

# Doctoral Dissertation (Censored)

## 博士論文 (要約)

### First-principles and machine learning study of anharmonic vibration and dielectric properties of materials

(物質の非調和振動と誘電特性の第一原理および機械学習による研究)

A Dissertation Submitted for the Degree of Doctor of Philosophy  
December 2023

令和5年12月 博士(理学) 申請

Department of Physics, Graduate School of Science, The University of Tokyo  
東京大学大学院理学系研究科物理学専攻

Tomohito Amano  
天野 智仁



# Abstract

This thesis aims to develop computational methods to predict the dielectric properties of materials. Dielectric properties describe the response of a material to an electric field and are essential in physics and practical applications. Infra-red spectroscopy has been widely used to study the structure and dynamics of crystals and molecules. In industry, dielectric materials play important roles in various fields, such as pigments, capacitors, optical coatings, and optical fiber. In recent years, low-dielectric materials for high-speed communications have also attracted attention. Prediction of dielectric properties by theoretical calculation is an important issue, for analyzing experimental spectra and developing new dielectric materials.

To accurately calculate the dielectric function, the classical static charge is often insufficient, and the Born effective charges or the mass center of the Wannier function (Wannier center) are required to describe the dipole moments of a system. There are two main methods for simulating dielectric properties. One is to calculate the dielectric properties of crystals using anharmonic phonons, and the other is to calculate the dielectric properties of liquids using molecular dynamics (MD) simulations. In this thesis, we addressed those two methods.

The anharmonic phonon method requires an accurate estimation of the phonon self-energies. Especially in the case of strongly anharmonic materials, the usual perturbation theory breaks down, and the self-energy must be treated self-consistently. Furthermore, the influence of the frequency dependence of the self-energy and the effect of the four-phonon scattering process on the dielectric properties have not been fully investigated. Therefore, in this thesis, we propose a method to calculate the dielectric properties of crystals with strong anharmonicity using the modified self-consistent phonon (SCPH) theory, including third-order anharmonicity as well as fourth-order anharmonicity. We applied our method to calculate the lattice dielectric function of strongly anharmonic rutile  $\text{TiO}_2$ . The resulting optical phonon frequencies and linewidths at the  $\Gamma$  point much better agree with experimental measurements than those from a perturbative approach. We show that the four-phonon scattering process contributes as much as the third-order anharmonic term to phonon linewidths of some phonon modes. Furthermore, incorporating the frequency dependence of phonon linewidth reveals that experimentally known but unidentified peaks of the dielectric function are due to the two-phonon process. This work emphasizes the importance of the self-consistent approach in predicting the optical properties of highly anharmonic materials.

In the MD method, the dipole moment is calculated by computing the Wannier centers at each step of MD, and the dielectric properties are estimated from the dipole autocorrelation function. The method is computationally time-consuming. In this thesis, we aimed to improve the computational efficiency by using machine learning (ML) techniques to calculate the dipole moments. So far, ML models of molecular dipole moments have focused primarily on the centroid of the Wannier functions of each molecule. However, this method is difficult to apply when the size of the molecules increases. Therefore, we develop a scheme that assigns Wannier centers to chemical bonds and makes predictions on a chemical bond basis. This method can be applied to larger molecules. Also, ML models are potentially applicable regardless of molecular species as we build them for each chemical bond. We apply this method to calculate the dielectric properties of methanol and ethanol. The ML model successfully predicted the dipole moments of molecules in the liquid phase with an accuracy of the root mean square error (RMSE) of 0.1 D. Furthermore, we show that the calculated dielectric constant and dielectric function reproduce experimental data well combined with classical MD and first-principles MD. We also show that the dipole moment and dielectric constant significantly increased in liquid due to the electronic polarization of the WCs of O lone pairs and OH bonds. We also apply our method to propylene glycol (PG), its dimer (PG2), and a much larger molecule, the 14-mer (PPG725). Our models predict the dipole moment of PPG725 with high accuracy. Also, when we train the ML model using only PG2 as training data, the model predicts the dielectric function of PPG725 in good agreement with experimental values.

We expect both methods we developed will be applied to other materials to elucidate the physical mechanisms contributing to dielectric properties and develop new dielectric materials.



# Contents

|   |           |
|---|-----------|
| <b>List of Abbreviations</b>  | <b>7</b>  |
| <b>List of Symbols</b>  | <b>9</b>  |
| <b>Chapter 1 Introduction</b>   | <b>11</b> |
| 1.1 Dielectric Function . . . . .   | 11        |
| 1.2 Three Mechanisms for Polarization . . . . .                               | 12        |
| 1.3 Lorentz and Debye Model . . . . .   | 14        |
| 1.3.1 The Lorentz model . . . . .   | 14        |
| 1.3.2 Debye model . . . . .   | 15        |
| 1.4 Theoretical Prediction of Dielectric Properties . . . . .                 | 16        |
| 1.4.1 Anharmonic phonon method . . . . .                                      | 17        |
| 1.4.2 Molecular dynamics simulation and machine learning . . . . .            | 18        |
| 1.5 Purpose and Outline of This Thesis . . . . .                              | 20        |
| <b>Chapter 2 Density Functional Theory</b>                                    | <b>23</b> |
| 2.1 Born-Oppenheimer Approximation . . . . .                                  | 23        |
| 2.2 Hellmann-Feynman Theorem . . . . .  | 24        |
| 2.3 Born-Oppenheimer Molecular Dynamics Simulation . . . . .                  | 25        |
| 2.4 Density Functional Theory . . . . .                                       | 26        |
| 2.4.1 Hohenberg-Kohn theorem . . . . .  | 26        |
| 2.4.2 Kohn-Sham scheme . . . . .  | 31        |
| 2.5 Density Functional Perturbation Theory . . . . .                          | 34        |
| <b>Chapter 3 Anharmonic Phonon Theory</b>                                     | <b>35</b> |
| 3.1 Lattice System . . . . .  | 35        |
| 3.2 Reciprocal Space . . . . .  | 36        |
| 3.3 Harmonic Approximation . . . . .  | 38        |
| 3.4 Normal Coordinates . . . . .  | 41        |
| 3.5 Expansion of Physical Quantities by Normal Coordinate . . . . .           | 43        |
| 3.6 Phonons . . . . .   | 47        |
| 3.7 Phonon Green's Function . . . . .   | 49        |
| 3.7.1 Green's function at finite temperature . . . . .                        | 49        |
| 3.7.2 Retarded Green's function . . . . .                                     | 51        |
| 3.7.3 Perturbation theory for the thermodynamic Green's function . . . . .    | 53        |
| 3.7.4 Harmonic phonon Green's function . . . . .                              | 54        |
| 3.7.5 Phonon self-energy . . . . .  | 55        |
| 3.8 Self-Consistent Phonon Theory . . . . .                                   | 57        |
| 3.9 Dielectric Function . . . . .   | 58        |
| 3.9.1 Cowley's formula . . . . .  | 58        |
| 3.9.2 Dielectric function from SCPH+B . . . . .                               | 60        |
| <b>Chapter 4 Modern Theory and Machine Learning of Polarization</b>           | <b>63</b> |
| <b>Chapter 5 Dielectric Properties of Strongly Anharmonic TiO<sub>2</sub></b> | <b>65</b> |
| 5.1 Introduction . . . . .  | 65        |
| 5.2 Four Parameter Semi-Quantum Model . . . . .                               | 67        |
| 5.3 Results and Discussion . . . . .  | 67        |
| 5.3.1 Computational details . . . . .   | 67        |
| 5.3.2 Phonon frequencies . . . . .  | 69        |
| 5.3.3 Results of the PBEsol functional . . . . .                              | 71        |

|                        |  |           |
|------------------------|--|-----------|
|                        | 5.3.4 Phonon linewidth . . . . .                                 | 73        |
|                        | 5.3.5 Phonon self energy . . . . .                               | 74        |
|                        | 5.3.6 Dielectric function . . . . .                              | 75        |
| 5.4                    | Conclusions . . . . .  | 79        |
| <b>Chapter 6</b>       | <b>Dielectric Properties of Liquid Alcohols and Its Polymers</b> | <b>81</b> |
| <b>Chapter 7</b>       | <b>Conclusion</b>  | <b>83</b> |
| 7.1                    | Summary of This Thesis . . . . .                                 | 83        |
| 7.2                    | Future Issues . . . . .  | 84        |
| <b>Appendix A</b>      | <b>Additional Simulation Results on Rutile TiO<sub>2</sub></b>   | <b>85</b> |
| <b>Acknowledgement</b> |  | <b>87</b> |

# List of Abbreviations

|               |   |
|---------------|---|
| <b>HK</b>     | Hohenberg-Kohn  |
| <b>KS</b>     | Kohn-Sham   |
| <b>DFPT</b>   | density functional perturbation theory                |
| <b>DFT</b>    | density functional theory                             |
| <b>ML</b>     | machine learning                                      |
| <b>PG</b>     | propylene glycol                                      |
| <b>PG2</b>    | di-propylene glycol                                   |
| <b>PPG725</b> | 14-mer of Propylene glycol                            |
| <b>SCPH</b>   | self-consistent phonon theory                         |
| <b>SCPH+B</b> | self-consistent phonon theory with the bubble diagram |
| <b>non-SC</b> | non self-consistent calculations                      |
| <b>WF</b>     | Wannier function                                      |
| <b>WC</b>     | Wannier center  |
| <b>LDA</b>    | local density approximation                           |
| <b>PBE</b>    | Perdew-Bruke-Ernzerhof                                |
| <b>BOMD</b>   | Born-Oppenheimer molecular dynamics                   |
| <b>BO</b>     | Born-Oppenheimer                                      |
| <b>AIMD</b>   | <i>ab initio</i> molecular dynamics                   |
| <b>LASSO</b>  | least absolute shrinkage and selection operator       |
| <b>IFC</b>    | interatomic force constant                            |
| <b>harm</b>   | harmonic approximation                                |
| <b>TDOS</b>   | two phonon density of state                           |
| <b>traj.</b>  | trajectory  |
| <b>lp</b>     | lone pair   |



# List of Symbols

|   |   |
|---|---|
| <b>D</b>  | electric flux density                       |
| <b>E</b>  | electric field                              |
| $\varepsilon$   | dielectric function                         |
| $\varepsilon_0$   | static dielectric constant                  |
| $\varepsilon_r$   | relative dielectric function                |
| <b>P</b>  | polarization                                |
| $\chi$  | susceptibility                              |
| $\varepsilon'$  | real part of dielectric function            |
| $\varepsilon''$   | minus imaginary part of dielectric function |
| $\varepsilon^{\text{inf}}$                                    | high-frequency dielectric constant          |
| $S_{\alpha\beta}^j$   | mode-oscillator strength                    |
| $v_0$   | the volume of a unitcell                    |
| $m_\kappa$  | the mass of the $\kappa$ -th atom           |
| $e_{\alpha\kappa}(\mathbf{q}j)$                               | phonon eigenvector                          |
| $u_{\kappa\alpha}$  | atomic displacement                         |
| $Z_{\kappa,\alpha\beta}^*$                                    | Born effective charge                       |
| $\Sigma(\omega)$  | phonon self-energy                          |
| $\Delta\omega(\omega)$  | minus real part of phonon self-energy       |
| $\Gamma(\omega)$  | imaginary part of phonon self-energy        |
| <b>M</b>  | dipole moment                               |
| $\Phi_{\mu_1 \dots \mu_n}(l_1 \kappa_1, \dots, l_n \kappa_n)$ | interatomic force constant                  |
| <b>q</b>  | phonon wavevector                           |
| $N$   | the number of atoms in a unitcell           |
| $N_{\text{cell}}$   | the number of unitcell in a supercell       |
| $D_{\mu_1 \mu_2}(l_1 \kappa_1, l_2 \kappa_2)$                 | dynamical matrix                            |
| $w_\mu(l, \kappa)$  | reduced atomic displacement                 |
| $\omega_{\mathbf{q}j}$  | phonon energy                               |
| $Q(\mathbf{q}j)$  | complex normal coordinate                   |
| $P(\mathbf{q}j)$  | complex normal momentum                     |
| $k_B$   | Boltzman constant                           |
| $A_{\mathbf{q}j}$   | phonon operator                             |
| $ \mathbf{R}n\rangle$   | Wannier function                            |
| $\mathbf{w}_n$  | Wannier center                              |
| $\hat{n}$   | complex refractive index                    |
| $n$   | refractive index                            |
| $\kappa$  | extinction coefficient                      |
| $\lambda$   | wavelength                                  |
| $\omega$  | angular frequency                           |
| $\alpha(\omega)$  | absorption coefficient                      |



# Chapter 1

## Introduction

Dielectric properties are crucial for the interaction between electric fields and materials. IR spectroscopy has been widely used to study the structure and dynamics of crystals and molecules, sometimes combined with Raman and THz spectroscopy. In industry, dielectric materials are used in various fields, such as pigments, capacitors, optical coatings, optical fiber, and high- $\kappa$  dielectric materials for DRAM [1]. In recent years, low-dielectric materials for high-speed communications have also attracted attention.

In this chapter, Sec. 1.1 to 1.3 outlines the basic concepts of dielectric properties and the history of their theoretical computation. We briefly introduce two methods used for theoretical calculations of dielectric properties in Sec. 1.4. Finally, we describe the purpose of this thesis in Sec. 1.5.

### 1.1 Dielectric Function

The central quantity of dielectric properties is the dielectric constant (or permittivity)  $\varepsilon$ , which is defined as the ratio between the electric flux density  $\mathbf{D}$  and the electric field  $\mathbf{E}$  as

$$\mathbf{D} = \varepsilon \mathbf{E}. \quad (1.1)$$

In general, the dielectric constant is anisotropic and is defined as a  $3 \times 3$  tensor. This measures the ease of polarization of a material when a static electric field is applied. The dielectric constant is often expressed in terms of the dimensionless relative permittivity  $\varepsilon_r$ , which is the ratio of the dielectric constant to the vacuum permittivity  $\varepsilon_0 = 8.854 \times 10^{-12}$  F/m as

$$\varepsilon = \varepsilon_0 \varepsilon_r. \quad (1.2)$$

In this thesis, unless otherwise stated, when we refer to dielectric functions, we mean relative dielectric functions. We list the relative permittivities of typical materials in Table 1.1. The relative dielectric constant changes its value considerably to reflect the dielectric properties of the material depending on how they tend to polarize.

We also introduce the related quantity called susceptibility  $\chi$ , which is the dimensionless constant connecting an electric field  $\mathbf{E}$  and the induced dielectric polarization density  $\mathbf{P}$  as

$$\mathbf{P} = \varepsilon_0 \chi \mathbf{E}. \quad (1.3)$$

Using the relationship between  $\mathbf{D}$  and  $\mathbf{P}$

$$\mathbf{D} = \varepsilon_0 \mathbf{E} + \mathbf{P}, \quad (1.4)$$

the following relationship between  $\varepsilon_r$  and  $\chi$  holds,

$$(1 + \chi) = \varepsilon_r. \quad (1.5)$$

By definition,  $\chi$  is zero in the case of vacuum.

Table 1.1: The static dielectric constant of typical materials at room temperature.

| Material              | Water | Methanol | benzene |
|-----------------------|-------|----------|---------|
| Relative Permittivity | 78.4  | 32.7     | 2.3     |

When a time-dependent electric field  $\mathbf{E}(t) = \mathbf{E}_0 e^{-i\omega t}$  is applied to a dielectric system, Equation (1.1) is extended to depend on the frequency and the dielectric function  $\varepsilon(\omega)$  and the susceptibility  $\chi(\omega)$  are introduced as follows.

$$\mathbf{D}(\omega) = \varepsilon(\omega)\mathbf{E}(\omega), \quad \mathbf{P}(\omega) = \varepsilon_0\chi(\omega)\mathbf{E}(\omega). \quad (1.6)$$

The response to an electric field must always be *causal*, occurring after applying an electric field, and can be expressed as a phase difference. Thus, the dielectric function is complex. We conventionally denote its real part as  $\varepsilon'$  and its imaginary part as  $\varepsilon''$  as<sup>\*1</sup>,

$$\varepsilon(\omega) = \varepsilon'(\omega) - i\varepsilon''(\omega). \quad (1.7)$$

Due to causality, the real and imaginary parts of the dielectric function are connected by the Kramers-Kronig relation, and when one is determined, the other is also determined. The real part of the dielectric function represents the ease of polarization of the material, and the imaginary part stands for the absorption of the electric field in the material. Their ratio is called the loss tangent as,

$$\tan \delta = \frac{\varepsilon''}{\varepsilon'}. \quad (1.8)$$

The lower the loss tangent, the more of the original signal reaches the destination. Materials with a lower loss tangent are, therefore, important for industrial applications. We often denote  $\varepsilon_0$  as the static dielectric constant to distinguish it from the dielectric function. The static dielectric constant is described by the low-frequency limit of the dielectric function as,

$$\varepsilon^0 = \lim_{\omega \rightarrow 0} \varepsilon(\omega), \quad (1.9)$$

while the high-frequency limit is called the optical dielectric constant  $\varepsilon^\infty$  as,

$$\varepsilon^\infty = \lim_{\omega \rightarrow \infty} \varepsilon(\omega). \quad (1.10)$$

## 1.2 Three Mechanisms for Polarization

Three main physical mechanisms actually contribute to the dielectric function, namely, the electronic, atomic, and orientational polarization, which are depicted in Fig. 1.1. In other words, They are the mechanism that generates dipole moments under an external electric field. The electron polarization is caused by the dipole moment produced by the relative displacement of the electronic cloud to the nucleus. It is called the electronic dipole moment  $\mathbf{p}$ , and the ratio to the external electric field  $\mathbf{E}$  is called the polarizability  $\alpha$  as,

$$\mathbf{p} = \alpha\mathbf{E}. \quad (1.11)$$

In atomic polarization, on which we focus in this thesis, the positively and negatively charged atoms move oppositely under the external field. The generated dipole moment is basically described as

$$\mathbf{p} = Z\Delta\mathbf{r}, \quad (1.12)$$

where  $Z$  is the atomic charge and  $\Delta\mathbf{r}$  is the nuclear displacement. We note that even in atomic polarization, electronic clouds move along nuclei and that we must include quantum mechanics effects to qualitatively describe this phenomenon. Sometimes atomic charges are replaced by effective charges (or dynamical charges) [2] to this end. In molecular systems, broad peaks appear in the THz range due to intermolecular interactions, and sharp peaks appear in the IR region due to intramolecular vibrations. In crystals, we have several peaks in the IR region due to IR active phonons.

Finally, unlike electronic and atomic polarization, orientational polarization only occurs when permanent dipole moments exist in the system, and their distribution is biased by an electric field. This phenomenon is widely observed in polar molecular liquids like water and alcohol, contributing to their large static dielectric constant.

The frequency range for which they are responsible is drastically different, reflecting the masses of molecules, atoms, and electrons. Electronic polarization is significant in the UV range, atomic polarization in the IR range, and dipolar polarization in the MHz range, as shown in Fig. 1.2.

---

<sup>\*1</sup> The sign convention for the imaginary part of permittivity is determined by the choice of sign for time-dependence,  $e^{-i\omega t}$ . The signs utilized here are the same as those frequently found in physics.

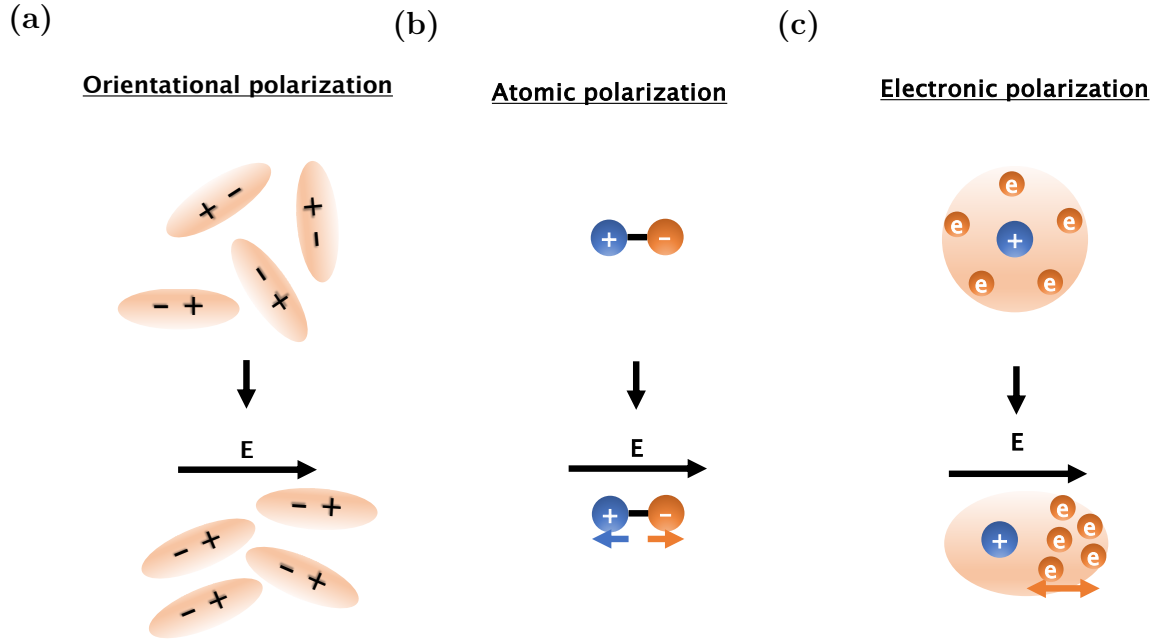


Fig. 1.1: The schematic image of three physical mechanisms of (a) the orientational (b) atomic (c) electronic polarization.  $\mathbf{E}$  denotes the external electric field, and these diagrams show how the system changes before and after the electric field is applied.

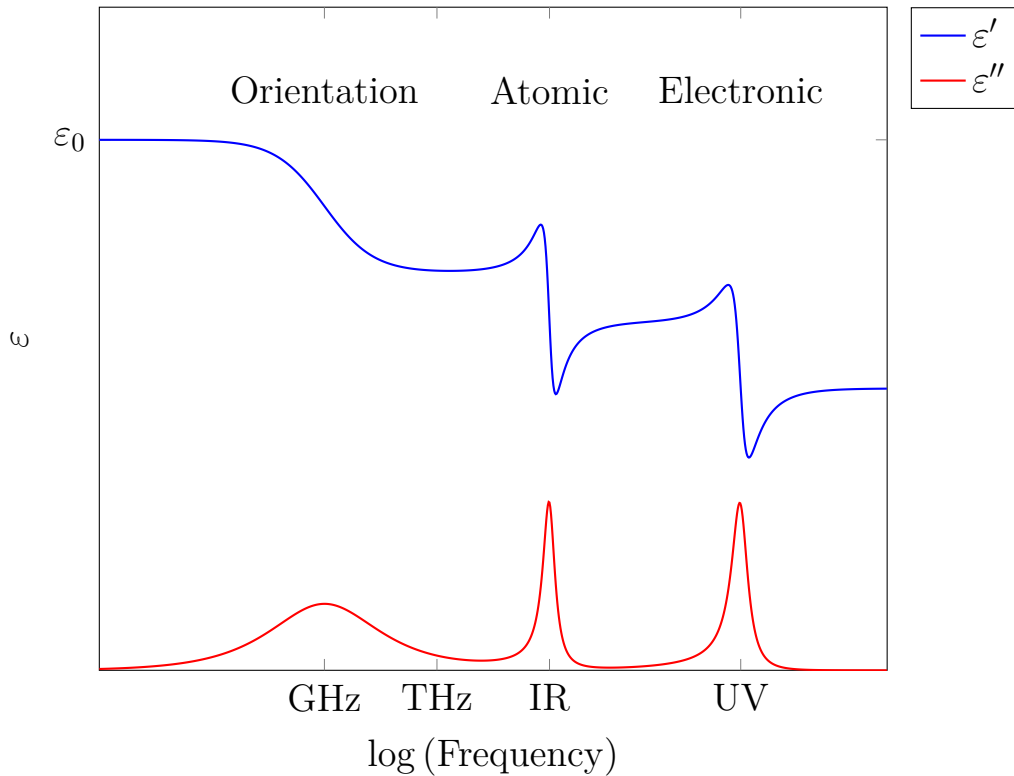


Fig. 1.2: The schematic figure of the real and imaginary part of the dielectric function.

At low frequencies, molecules are polarized by an applied electric field, which induces molecular rotations. At intermediate frequencies, the energy of an electric field is too high to cause rotations, yet too low to affect electrons directly, and is absorbed in the form of molecular or atomic vibrations. In polar liquids, this is where the imaginary part of the dielectric function starts to drop sharply. At high frequencies, molecules can not respond, and the energy is purely absorbed by atoms to excite electrons. Therefore, the optical dielectric constant  $\epsilon^\infty$  purely reflects electronic polarization.

This separation of frequency domains is vital in computational simulations. In this thesis, we will devote

ourselves to atomic polarization, in which case the electronic polarization is treated as a constant and can be written as follows,

$$\varepsilon(\omega) = \varepsilon^\infty + \varepsilon_{\text{atoms}}(\varepsilon). \quad (1.13)$$

### 1.3 Lorentz and Debye Model

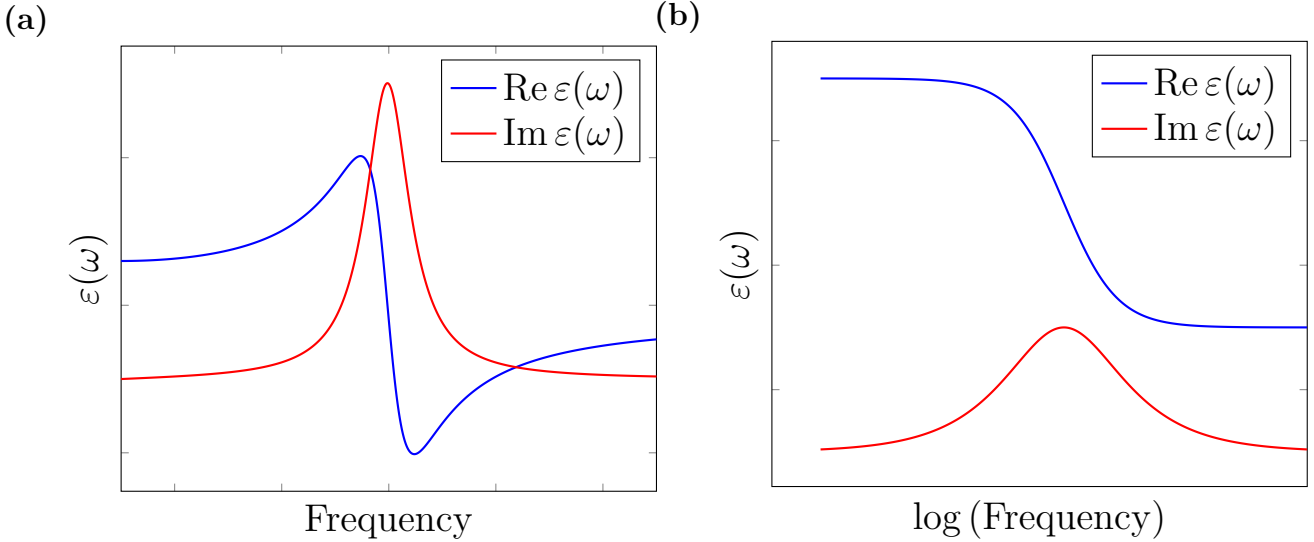


Fig. 1.3: The typical dielectric function of (a) the Lorentz model and (b) the Debye model. The blue lines represent the real part of the dielectric function, while the red lines correspond to the imaginary part. The peak positions of the imaginary part of the dielectric function are given by the resonance frequency  $\omega_0$  and the inverse of the relaxation time  $1/\tau$  for the Lorentz and Debye models, respectively.

The Debye and Lorentz models are the basic models for describing the dielectric function. The former describes orientational polarization, while the latter describes atomic polarization. They are still widely used for analyzing experimental spectrum. Typical function forms are shown in Fig. 1.3.

#### 1.3.1 The Lorentz model

Suppose that the system consists of independent harmonic oscillators. Let its density be  $N$ , its eigenfrequency  $\omega_0$ , and the relative displacement of the center of mass of  $\pm q$  charges be  $x$ . Denoting the damping constant by  $\Gamma$ , Newton's equation of motion of the oscillator with friction can be written as follows.

$$M \frac{d^2 x}{dt^2} = -M\omega_0^2 x + qE - M\Gamma \frac{dx}{dt}. \quad (1.14)$$

If  $x$  and  $E$  are proportional to  $e^{-i\omega t}$ ,  $x$  is solved for

$$x = \frac{qE}{M(\omega_0^2 - \omega^2 - i\Gamma\omega)}. \quad (1.15)$$

Since the polarization is given by  $P = Nqx$ , we have the relation between the polarization and the electric field as

$$P = \frac{Nq^2 E}{M(\omega_0^2 - \omega^2 - i\Gamma\omega)}. \quad (1.16)$$

The susceptibility and the dielectric function are calculated from Eq. (1.3) and (1.5), respectively:

$$\chi(\omega) = \frac{q^2}{\varepsilon_0 M(\omega_0^2 - \omega^2 - i\Gamma\omega)}, \quad (1.17)$$

$$\varepsilon(\omega) = \varepsilon_0 + \frac{q^2}{M(\omega_0^2 - \omega^2 - i\Gamma\omega)}. \quad (1.18)$$

In actual materials, the dielectric function is expressed as a superposition of several oscillators and has the form

$$\varepsilon(\omega) = \varepsilon^\infty + \sum_j \frac{\Delta\varepsilon_j \omega_{\mathbf{0}j}^2}{\omega^2 - \omega_{\mathbf{0}j}^2 + i\gamma_{\mathbf{0}j}\omega}, \quad (1.19)$$

where  $\omega_{\mathbf{q}j}$ ,  $\Delta\varepsilon_j$ , and  $\gamma_{\mathbf{q}j}$  are the resonant frequency, the oscillator strength, and the damping (FWHM) of the phonon with wave vector  $\mathbf{q}$  and mode  $j$ .  $\varepsilon^\infty$  is the electronic dielectric constant. We note that the constant term in Equation (1.19) is replaced with  $\varepsilon^\infty$  to include the electronic polarization effect. If there is only one oscillator, Eq. (1.19) can be rewritten using  $\varepsilon(0) = \varepsilon_0$  as,

$$\varepsilon(\omega) = \varepsilon^\infty + \frac{(\varepsilon^0 - \varepsilon^\infty)\omega_0^2}{\omega^2 - \omega_0^2 + i\gamma_0\omega}. \quad (1.20)$$

The real and imaginary parts of the dielectric function are given by

$$\varepsilon'(\omega) = \text{Re } \varepsilon(\omega) = \varepsilon^\infty + \frac{(\varepsilon^0 - \varepsilon^\infty)\omega_0^2 (\omega^2 - \omega_0^2)}{(\omega^2 - \omega_0^2)^2 + \omega^2\gamma_0^2} \quad (1.21)$$

$$\varepsilon''(\omega) = -\text{Im } \varepsilon(\omega) = \frac{(\varepsilon^0 - \varepsilon^\infty)\omega_0^2\gamma_0\omega}{(\omega^2 - \omega_0^2)^2 + \omega^2\gamma_0^2}, \quad (1.22)$$

which are illustrated in Fig. 1.3a

### 1.3.2 Debye model

The Debye model is based on the assumption that the polarization shows exponential decay without the external field as

$$\frac{d\mathbf{P}}{dt} = -\frac{\mathbf{P}}{\tau}, \quad (1.23)$$

where  $\tau$  is the relaxation time. Under the external electric field  $E(t)$ , the polarization obeys the following equation,

$$\frac{d\mathbf{P}}{dt} = \frac{1}{\tau} [\chi_0 \mathbf{E} - \mathbf{P}]. \quad (1.24)$$

If  $\mathbf{P}$  and  $\mathbf{E}$  are proportional to  $e^{-i\omega t}$ ,  $\mathbf{P}$  is solved for

$$\mathbf{P} = \frac{\chi_0}{1 - i\omega\tau} \mathbf{E}. \quad (1.25)$$

From Eq. (1.3) and Eq. (1.5), the dielectric function is

$$\varepsilon(\omega) = \varepsilon^\infty + \frac{\varepsilon^0 - \varepsilon^\infty}{1 - i\omega\tau}. \quad (1.26)$$

The real and imaginary parts are explicitly written as follows,

$$\varepsilon'(\omega) = \varepsilon^\infty + (\varepsilon^0 - \varepsilon^\infty) \frac{1}{1 + \omega^2\tau^2} \quad (1.27)$$

$$\varepsilon''(\omega) = (\varepsilon^0 - \varepsilon^\infty) \frac{\omega\tau}{1 + \omega^2\tau^2}. \quad (1.28)$$

By removing  $\omega$  from the above expression, we get the relation between the real and imaginary part

$$\left( \varepsilon'(\omega) - \frac{1}{2}(\varepsilon^\infty + \varepsilon^0) \right)^2 + (\varepsilon''(\omega))^2 = \frac{1}{4}(\varepsilon^0 - \varepsilon^\infty)^2 \quad (1.29)$$

which is called the Cole-Cole relation [3]. There exist several relaxation times in real materials, and the equation is extended to the form

$$\varepsilon(\omega) = \varepsilon^\infty + \sum_i \frac{\chi_i}{1 - i\omega\tau_i}. \quad (1.30)$$

In actual polar materials, there are several modes with multiple relaxation times, and these are often superimposed to represent the experimental spectrum. Furthermore, as the extension of this model, the phenomenological expression called the Havriliak-Negami relation [4] is known as

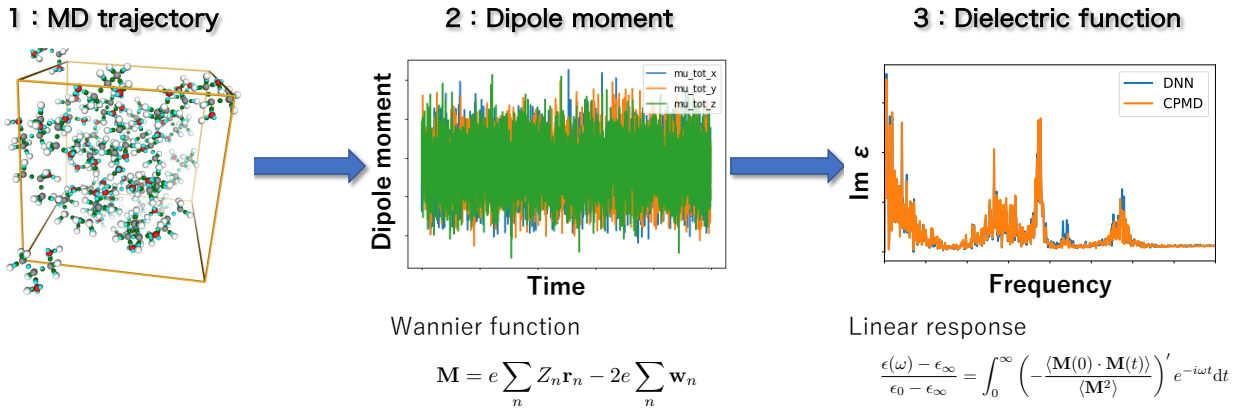
$$\varepsilon(\omega) = \varepsilon^\infty + \frac{\chi_0}{(1 - (i\omega\tau)^\beta)^\alpha}, \quad (1.31)$$

where  $\alpha$  and  $\beta$  are empirical parameters.

## 1.4 Theoretical Prediction of Dielectric Properties

Theoretical calculations of dielectric properties are of great importance for the interpretation of experimental spectra and the development of new dielectrics. Even though the Debye and Lorenz models have been very successful, they are based on classical theory and cannot incorporate quantum effects. DFT simulations are important for a more accurate evaluation of dielectric properties. Recent developments in theory and machine learning have made DFT-based calculations possible. Theoretical calculations are mainly done by the linear response theory [5] to electric fields. Therefore, the method to calculate system dipole moments is essential. There are two main methods, as shown in Fig. 1.4. One is based on the anharmonic phonon theory, which extends the Lorenz model to quantum mechanics. This method allows theoretical prediction of dielectric properties using DFT-based phonon calculations. The other way is based on molecular dynamics simulations, which can be accelerated using machine-learning techniques. This method applies not only to crystals but also to liquids and amorphous materials.

(a)



(b)

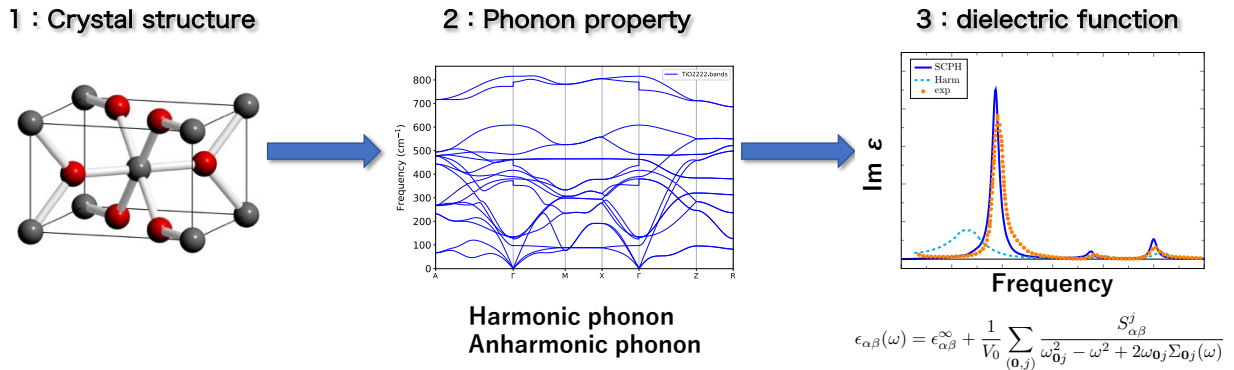


Fig. 1.4: Workflow to calculate the dielectric function. (a) In the anharmonic phonon method, the anharmonic phonon property is calculated from the DFT calculation of the crystal, from which the dielectric function is calculated according to the linear response theory. (b) In the molecular dynamics method, the trajectory is first obtained using molecular dynamics simulations and the dipole moment is calculated at each step. The dielectric function is calculated according to the linear response theory.

### 1.4.1 Anharmonic phonon method

The Lorentz model has three parameters: phonon frequency, oscillator strength, and damping factor. The damping factor directly relates to the lifetime of the phonons  $\tau$  as  $\tau = 1/\gamma$ , and phonons have infinite lifetimes under the harmonic approximation where phonons do not interact. Therefore, it is impossible to determine the dielectric function under the harmonic approximation. The phonon lifetime is treated as a parameter and determined by fitting the experimental spectrum. In this way, for example, the temperature dependence of phonon lifetimes can be investigated [6].

Cowley [7] reformulated the Lorentz model in terms of quantum mechanics and derived the following expression of the dielectric function using the anharmonic lattice dynamics theory [8] and the linear response theory,

$$\varepsilon_{\alpha\beta}(\omega) = \varepsilon_{\alpha\beta}^{\infty} + \frac{1}{v_0} \sum_j \frac{S_{\alpha\beta}^j}{(\omega_{0j})^2 - \omega^2 - 2\omega_{0j}\Sigma_{0j}(\omega)}, \quad (1.32)$$

where  $v_0$  is the volume of the unitcell,  $\alpha$  and  $\beta$  are Cartesian indices, and  $\Sigma(\omega)$  is phonon self-energy. Summations are taken only for TO phonons at the  $\Gamma$  point.  $S_{\alpha\beta}^j$  is called mode-oscillator strength defined as follows [9],

$$S_{\alpha\beta}^j = \left( \sum_{\kappa\alpha'} Z_{\kappa,\alpha\alpha'}^* \frac{e_{\kappa\alpha'}(\mathbf{0}j)}{\sqrt{m_{\kappa}}} \right) \left( \sum_{\kappa\beta'} Z_{\kappa,\beta\beta'}^* \frac{e_{\kappa\beta'}(\mathbf{0}j)}{\sqrt{m_{\kappa}}} \right), \quad (1.33)$$

where  $\kappa$  is the index of the atoms,  $m_{\kappa}$  is the mass of the  $\kappa$ -th atom, and  $e_{\alpha\kappa}(\mathbf{0}j)$  is a phonon eigenvector.  $Z^*$  is the Born effective charge, originally introduced by Born and Goppert-Mayer [8], which is the derivative of the polarization  $\mathbf{P}$  with respect to atomic coordinates at the zero electric field  $\mathbf{E} = \mathbf{0}$ ,

$$Z_{\kappa,\alpha\beta}^* = v_0 \left. \frac{\partial P_{\alpha}}{\partial u_{\kappa,\beta}} \right|_{\mathbf{E}=\mathbf{0}}. \quad (1.34)$$

As the polarization itself can be written in terms of the derivative of the energy with respect to the electric field as

$$\frac{\partial U}{\partial E_{\alpha}} = v_0 P_{\alpha}, \quad (1.35)$$

$Z^*$  is ultimately the second-order derivative of the energy, which can be calculated from first principles using the density functional perturbation theory (DFPT) [9–12]:

$$Z_{\kappa,\alpha\beta}^* = \frac{\partial U}{\partial E_{\alpha} u_{\kappa,\beta}}. \quad (1.36)$$

As the atomic force is the derivative of the energy with respect to atomic coordinates,  $Z^*$  is also related to the atomic force as

$$Z_{\kappa,\alpha\beta}^* = \frac{\partial F_{\kappa,\beta}}{\partial E_{\alpha}}. \quad (1.37)$$

$Z^*$  differs from the usual static charges or ionic charges [2]. The Born effective charges are also used to calculate the long-range Coulomb forces of the  $\Gamma$  point phonons in insulators, allowing the magnitude of the LO-TO splitting to be calculated. In recent years, it has also been used to calculate charge transportation [13, 14] and molecular dynamics simulations under electric fields [15].

Compared to the Lorentz model, Eq. (1.32) differs in that the damping factor is described by the phonon self-energy, which is a frequency-dependent and complex property. The real and imaginary parts of the self-energy are called frequency shift and linewidth, respectively, as

$$\Sigma(\omega) = -\Delta\omega(\omega) + i\Gamma(\omega). \quad (1.38)$$

Phonon lifetime  $\tau_{qj}$  is related to linewidth as  $\tau_{qj} = 1/2\Gamma(\omega_{qj})$ , and a damping parameter in the Lorentz model or the FPSQ model holds  $\gamma_{0j} = 2\Gamma(\omega_{0j})$ . To evaluate this expression, we must calculate the phonon self-energy, which is zero within the harmonic approximation. Therefore, it is necessary to perform calculations that incorporate the anharmonic effects of phonons. When the crystal structure is relatively simple, it is known that multi-parameter calculations of anharmonic phonons are in relatively good agreement with experiments [16–18].

Recently, first-principles methods to calculate phonon anharmonicity [19–24] have been developed, in which harmonic and anharmonic interatomic force constants (IFCs) are estimated from the set of atomic coordinates and forces calculated from *ab initio* density functional theory (DFT) or DFPT. Diagonalizing a dynamical matrix calculated from harmonic IFCs yields ordinary harmonic phonon frequencies and eigenvectors, whereas anharmonic IFCs determine self-energies that cause the frequency shifts and linewidths. This framework has made it possible to calculate phonon lifetimes, transport or thermal properties like thermal conductivity, and temperature dependence of phonon frequencies. Compared to molecular dynamics simulations, this method involves zero-point vibration and does not need long simulations.

The original studies are based on the perturbation theory, which has successfully explained lattice thermal conductivity in a wide variety of materials only with the third-order anharmonic terms [25]. However, the perturbative approach is valid only when the anharmonic self-energies are sufficiently small compared to the harmonic frequencies. Therefore, this method cannot be used for highly anharmonic materials, including the high-temperature phases of ferroelectric materials [26], and we need a nonperturbative scheme to overcome this limitation. The *ab initio* molecular dynamics (AIMD) based method and the self-consistent phonon (SCPH) based approach are used for this purpose. The temperature-dependent effective potential (TDEP) method [23, 27] is an example of the former method, which constructs an effective harmonic model at a target temperature from atomic configurations generated by AIMD. The self-consistent phonon (SCPH) theory [28, 29] includes the frequency shift associated with fourth-order anharmonicity in a self-consistent manner. This theory, originally developed by Hooton [30] and followed by the formulations using the many-body theory [31–33], composes an effective harmonic Hamiltonian (SCPH Hamiltonian) that includes anharmonicity, and can be valid when imaginary phonons appear in the harmonic phonons [28, 29]. Furthermore, the calculation of phonon lifetimes on the SCPH Hamiltonian improves the thermal conductivity compared to the usual perturbation calculations. There are several methods for constructing the SCPH Hamiltonian, including stochastic sampling approaches from the different atomic configurations, such as self-consistent *ab initio* lattice dynamics (SCAILD) [34] and stochastic self-consistent harmonic approximation (SSCHA) [24, 35], and the Green’s function method where anharmonic frequencies are estimated from the Dyson equation, implemented in the ALAMODE package [28, 29].

Several attempts have been made to calculate more accurate phonon properties. The SCPH+B theory includes the frequency shift associated with third-order anharmonicity within a quasiparticle approximation [36] to suppress the overestimation of phonon frequencies in the SCPH theory. The influence of the higher-order 4-phonon scattering diagram has also been investigated, and it has been shown to provide more accurate predictions of thermal conductivity and phonon linewidths for strongly anharmonic materials [37–42].

While the accurate SCPH theory has been successful in many thermal conductivity calculations, there have been few such attempts for lattice dielectric properties [43, 44], which only discussed static dielectric constants. This is partly due to the fact that the dielectric function requires higher accuracy than the thermal conductivity, as the frequency and self-energy for particular  $\Gamma$  point phonons have a significant influence on the results. The linewidths in specific phonon modes have been investigated for various materials [45–50]. Lattice dielectric properties of weakly anharmonic materials [51–55] have been studied using perturbation theory. According to the Lorentz model studies, the anharmonic term of four phonon scattering is not negligible for estimating optical properties [54, 55]. Fugallo et al. [53] used the Cowley formula [7] to incorporate the frequency dependence of a damping parameter and successfully obtained the dielectric spectra of MgO in good agreement with experiment.

### 1.4.2 Molecular dynamics simulation and machine learning

The second method uses molecular dynamics simulations, invented in 1964 by Rahman [56]. The dielectric function of a system can be calculated from the dipole auto-correlation function along MD trajectories based on the linear response theory [57–60]. Therefore, to accurately calculate the dielectric properties, not only the trajectories but also the dipole moments of the system need to be accurately calculated [61]. In classical MD calculations, which rely on parameterized functions to compute the forces acting on atoms, the dipole  $\mathbf{M}$  is calculated by assigning an empirical fixed charge  $q_i$  to the atom  $\mathbf{r}_i$  as

$$\mathbf{M} = \sum_i q_i \mathbf{r}_i. \quad (1.39)$$

Famous methods to assign these static charges include Mulliken [62], Hirshfeld [63], Bader [64], and RESP [65] charges. These methods may not work, especially when polarization or induced dipole moment is not negligible, where electron contribution needs to be described in a more sophisticated manner. For example, in hydrogen bonded systems, atomic charges are primarily affected by the local environment [66, 67]. In addition, the effect of induced dipoles is substantial for nonpolar materials such as benzene, especially the

libration peak appearing in the THz band [61], which cannot be reproduced by Eq. (1.39).

*Ab initio* molecular dynamics (AIMD) [68] was developed to overcome the problems in classical MD, in which the motion of the nuclei is described classically according to Newton's equations of motion and atomic forces are calculated using the quantum mechanics of the electrons and nuclei. AIMD is a versatile tool and has been used to study a wide variety of interesting and important problems. Examples include the structure and dynamics of liquid molecules [69–76], charge transport in solutions [13, 14], and others.

Adding to this, for the dipole moment part, the modern theory of polarization [77–81] can treat the dipole moment in a quantum mechanics manner through the Berry phase approach [82] or the maximally localized Wannier functions (MLWF) scheme [83, 84]. The total dipole moment consists of the ionic and the electronic parts. The ionic dipoles can be calculated from ionic charges and positions as usual. In the former method, the electronic contribution is expressed as an integral of the Berry phase, and the total dipole moment is

$$\mathbf{M} = e \sum_{i=1}^N Z_i \mathbf{r}_i + e \text{Im} \sum_n \int_{\text{BZ}} \frac{d\mathbf{k}}{(2\pi)^3} \langle u_{n\mathbf{k}} | \nabla_{\mathbf{k}} | u_{n\mathbf{k}} \rangle, \quad (1.40)$$

where  $Z_i$  is the ionic charge of atom  $i$ , and  $\mathbf{r}_i$  denotes the nuclear position.  $N$  is the number of atoms. The Bloch wavefunction at the band  $n$  and the wave vector  $\mathbf{k}$  is written as  $\psi_{n\mathbf{k}}(\mathbf{r}) = e^{i\mathbf{k} \cdot \mathbf{r}} u_{n\mathbf{k}}(\mathbf{r})$  using the periodic function  $u_{n\mathbf{k}}(\mathbf{r})$ .

In the MLWF method, the electronic contribution is evaluated from the  $-2e$  point charges at the center of MLWFs  $\mathbf{w}$ , called Wannier centers (WCs) as

$$\mathbf{M} = e \sum_{i=1}^N Z_i \mathbf{r}_i - 2e \sum_{k=1}^{N_w} \mathbf{w}_k, \quad (1.41)$$

where  $N_w$  is the number of WCs. It is particularly suitable for molecular systems because it treats individual electronic contribution explicitly. Combining AIMD and the modern theory of polarization, several studies have succeeded in calculating dielectric properties with results in good agreement with experiments for molecular systems [69, 70, 75, 85] and inorganic crystals [86, 87]. Although the AIMD method has been successful for many systems due to its accuracy, the high computational cost of it still imposes significant constraints on the size of the system and the time available for computation. In particular, long-time simulations of several nanoseconds are required for the calculation of dielectric constants [88], and it is difficult to use AIMD directly for this calculation.

In recent years, machine learning methods have been utilized to express *ab initio* potential energy surfaces as a function of nuclear coordinates  $\{\mathbf{r}\}$  as [89–93],

$$E = f(\{\mathbf{r}\}). \quad (1.42)$$

These methods are faster while maintaining the same level of accuracy as AIMD calculations and are used for larger systems and longer-time simulations. Most methods decomposed the total potential energy into a sum of atomic energy contributions,

$$E = \sum_i E_i \quad (1.43)$$

with  $i$  being the index of the atoms. Thanks to this decomposition, each atomic energy can be determined from the position of the  $i$ th atom and its near neighbors

$$E_i = E_i(\mathbf{r}_i, \{\mathbf{r}_j | j \in N_{r_c}(i)\}), \quad (1.44)$$

where  $N_{r_c}(i)$  denotes the index set of the neighbors of atom  $i$  within some cutoff radius  $r_c$ . This local environment approach greatly reduces the computational cost, while it is difficult to treat long-range Coulomb interaction in this scheme.

There are several ways to represent the local environment. It's important to ensure physical symmetry like the translational, rotational, and permutational invariances, which greatly improve the model accuracy and reduce the number of training data. Behler and Parrinello [89, 90] introduced atom-centered symmetry functions (ACSFs) consisting of two and three body terms

$$G_i^2 = \sum_{j \neq i} e^{-\eta(r_{ij} - r_s)^2} f_c(r_{ij}) \quad (1.45)$$

$$G_i^3 = 2^{1-\zeta} \sum_{(j,k) \neq i} (1 + \lambda \cos \theta_{ijk}) \zeta e^{-\eta(r_{ij}^2 + r_{jk}^2 + r_{ki}^2)} f_c(r_{ij}) f_c(r_{jk}) f_c(r_{ki}). \quad (1.46)$$

The summations are taken over all atoms within a cutoff radius  $r_c$ .  $r_{ij}$  is the distance between atoms  $i$  and  $j$ ,  $\theta_{ijk}$  is the angle created by three atoms  $i$ ,  $j$  and  $k$ . A cutoff function  $f_c(r)$  decays smoothly to zero as  $r$  approaches  $r_c$ .  $\eta$ ,  $r_s$ ,  $\zeta$ , and  $\lambda = \pm 1$  are hyperparameters. As the atom order is irrelevant for the values of  $G_i^2$  and  $G_i^3$  and only internal coordinates are used to calculate them, all physical invariants are satisfied.

Another approach often used is to describe the atomic environment using graph neural networks [94–96]. In this method, systems are considered as an undirected graph, with atoms represented as nodes and interactions between atoms as edges. By exchanging information (message passing [97]) between nodes along edges, complex chemical interactions can be modeled.

To calculate dielectric properties using this technique, however, we also need machine learning models to predict the dipole moment from atomic positions. Gastegger et al. [98] developed a model that learns the environment-dependent atomic partial charges  $\tilde{q}(\{\mathbf{r}\})$ , which varies depending on the positions of neighborhood atoms in contrast to the classical empirical charges, and thus describes the polarization effect of electrons well. Their model successfully reproduced the experimental IR spectrum of gas-phase methanol, n-alkanes, and protonated alanine tripeptide. In this method, the total dipole moment is described as a sum of environment-dependent atomic partial charges

$$\tilde{\boldsymbol{\mu}} = \sum_i \tilde{q}(\{\mathbf{r}_i\}) \mathbf{r}_i. \quad (1.47)$$

The loss function  $L$  is then constructed as the difference of predicted molecular dipole moments from that of training data  $\boldsymbol{\mu}^{\text{ref}}$

$$L = \frac{1}{N} \sum_{i=1}^N |\tilde{\boldsymbol{\mu}}_i - \boldsymbol{\mu}_i^{\text{ref}}|^2, \quad (1.48)$$

where the environment-dependent atomic charges are inferred indirectly because atomic partial charges are not quantum mechanical observable, unlike energies and forces.

An alternative approach is to manipulate the MLWFs directly. Several authors constructed the ML models to predict the centroid of the WCs of water molecules and successfully reproduced dielectric properties [88, 99–101]. In water, the centroid of the WCs is defined by the average position of the four Wannier centers associated with oxygen  $i$

$$\mathbf{w}_i^{\text{C}} = \frac{1}{4} \sum_{l_i=1}^4 \mathbf{w}_{l_i}. \quad (1.49)$$

They developed a machine learning model to infer  $\mathbf{w}_i^{\text{C}}$ , and the total dipole moment is then calculated from Eq. (1.41) as

$$\mathbf{D} = e \sum_{i=1}^N Z_i \mathbf{r}_i - 2e \sum_{k=1}^{N_w} \mathbf{w}_k^{\text{C}}, \quad (1.50)$$

This idea was also used to build the machine learning potential with long-range coulomb interaction [102]. Even though the scheme works for small molecules like water, it is not easy to apply when the molecules become larger and more complex. We note that the dipole moment and the potential energy behave differently under symmetry operations. The potential energy is a scalar quantity that remains constant despite changes in translation, rotation, and permutation. By contrast, the dipole moment is a vector and must change in the same way as the coordinate vector under the rotation.

## 1.5 Purpose and Outline of This Thesis

In this study, we aim to establish the methods to calculate dielectric properties from first principles using both the anharmonic phonon method and the molecular dynamics method.

First, for crystalline systems, we aimed to develop a computational method to calculate dielectric functions applicable to highly anharmonic materials. As mentioned in the previous section, the calculation of dielectric properties using the anharmonic phonon method has yet to be done very often. One reason is that the calculation of dielectric properties requires the analysis of specific IR active phonon modes, which must be very accurate. Therefore, few calculations were performed on highly anharmonic materials where perturbations would break down. To make our estimations as precise as possible, we used a modified self-consistent phonon method including third-order anharmonicity as well as fourth-order anharmonicity, taking into account fourth-order self-energies and including the frequency-dependence of the self-energies.

Second, for molecular systems, we aimed to develop a scheme to construct a machine-learning model of dipole moments. Although the Wannier centroid method used in previous studies is possible for simple molecules like  $\text{H}_2\text{O}$ , it does not apply to more complex materials. Instead, we have developed a versatile machine learning model of dipole moments applicable to molecular liquids. We assigned MLWFs to chemical bonds between atoms and used deep neural networks to predict the position of the MLWFs for each bond.

This thesis is organized as follows. Chapter 2 provides a brief introduction to the density functional theory for first-principles calculations.

In chapter 3, we introduce the anharmonic phonon theory. First, we review the lattice system based on the Taylor expansion, followed by the Green’s function theory for phonons. On the basis of the above, we show how to calculate dielectric functions based on the Green’s function method. We introduce the self-consistent phonon (SCPH) theory, which is effective for strongly anharmonic materials, and propose a method for calculating dielectric functions using the SCPH theory.

In chapter 4, we introduce the modern theory of polarization necessary for machine learning of dipole moments. After seeing that the polarization can be described by the center of mass of the Wannier function, the Wannier centers, we propose a chemical bond based scheme for the Wannier centers.

In chapter 5, the method to calculate the dielectric function using the SCPH method, introduced in chapter 3, is applied to rutile  $\text{TiO}_2$ , which is known for its strong anharmonicity. Rutile  $\text{TiO}_2$  has a very large dielectric constant, and its dielectric properties have been studied for a long time. However, its strong anharmonicity makes accurate calculations difficult, and the existence of peaks of unknown origin is experimentally known. We address these issues by applying the methodology we have developed.

In chapter 6, a machine learning dipole moment, which is introduced in chapter 4, is applied to calculate the dielectric properties of liquid alcohol. Methanol and ethanol are both basic alcohols, but their hydrogen bonding makes an accurate description of their dielectric properties difficult. We applied our developed method to verify whether the dielectric properties can be accurately calculated and also investigated the effect of intermolecular interactions on the dielectric properties. Next, we applied our scheme to propylene glycol (PG) and its polymers to investigate its versatility. In particular, the 14-mer of PG, called PPG725, contains 123 atoms per molecule. Furthermore, we investigated the transferability between the models.

Finally, we conclude this work in chapter 7.



## Chapter 2

# Density Functional Theory

This chapter introduces the basics of density functional theory (DFT). First, the Born-Oppenheimer (BO) approximation, a basic approximation for describing electron lattice systems, and related topics are introduced in Sec. 2.1 to 2.3. Then, DFT for electronic structure calculations is explained in Sec. 2.4. Finally, we briefly introduce DFPT in Sec. 2.5.

### 2.1 Born-Oppenheimer Approximation

We first discuss the electron lattice systems and how to separate out the motion of the nucleus and the electrons. Let us consider a system of  $N$  nuclei and  $N_e$  electrons, ignoring nuclear spin. The Hamiltonian of the system is given by

$$\hat{H} = \hat{T}_n + \hat{T}_e + \hat{V}_{ee} + \hat{V}_{nn} + \hat{V}_{en}. \quad (2.1)$$

$\hat{T}_n$  and  $\hat{T}_e$  are the nuclear and electron kinetic energy operators, while  $\hat{V}_{ee}$ ,  $\hat{V}_{nn}$ , and  $\hat{V}_{en}$  represent electron-electron, nuclear-nuclear, and electron-nuclear interaction potential operators, respectively. Their forms are given by

$$\hat{T}_n = \sum_{I=1}^N \frac{\hat{P}_I^2}{2M_I} \quad (2.2)$$

$$\hat{T}_e = \sum_{i=1}^{N_e} \frac{\hat{p}_i^2}{2m} \quad (2.3)$$

$$\hat{V}_{ee} = \sum_{(i>j)} \frac{e^2}{|r_i - r_j|} \quad (2.4)$$

$$\hat{V}_{nn} = \sum_{(I>J)} \frac{Z_I Z_J e^2}{|R_I - R_J|} \quad (2.5)$$

$$\hat{V}_{en} = - \sum_{(i,I)} \frac{Z_I e^2}{|R_I - r_i|}, \quad (2.6)$$

where  $\mathbf{R} = \{\mathbf{R}_1, \mathbf{R}_2, \dots, \mathbf{R}_N\}$ ,  $\hat{\mathbf{P}} = \{\hat{\mathbf{P}}_1, \dots, \hat{\mathbf{P}}_N\}$  and  $M = \{M_1, \dots, M_N\}$  are atomic coordinates, momenta, and masses.  $\mathbf{r} = \{\mathbf{r}_1, \dots, \mathbf{r}_{N_e}\}$ ,  $\mathbf{p} = \{\mathbf{p}_1, \dots, \mathbf{p}_{N_e}\}$ , and  $\sigma = \{\sigma_1, \dots, \sigma_{N_e}\}$  are electronic coordinates, momenta, and spin variables taking  $\pm 1/2$ .  $Z_I$  is the  $I$ th nucleus charge, and  $m$  is the electron mass. We express  $x \equiv (\mathbf{r}, s)$  as the collection of electron position and spin variables. The eigenfunctions  $\Psi(x, \mathbf{R})$  and eigenvalues  $\hat{H}$  of the Hamiltonian Eq. (2.1) satisfy the Schrödinger equation

$$\hat{H}\Psi(x, \mathbf{R}) = E\Psi(x, \mathbf{R}), \quad (2.7)$$

which is impossible to be solved exactly. The Born-Oppenheimer approximation [103] is based on the fact that the timescales of the electronic and nuclear motion are significantly different since the electrons are much lighter<sup>\*1</sup> than the nuclei. This can be expressed as a separable ansatz of the wavefunction as [104]

$$\Psi(x, \mathbf{R}) = \psi(x, \mathbf{R})\chi(\mathbf{R}), \quad (2.8)$$

---

<sup>\*1</sup> The mass of a single electron is  $m_e = 9.198 \times 10^{-31}$  Kg, which is only about 1/1860th of the proton mass.

where we decompose the total wavefunction into a nuclear wavefunction  $\chi(\mathbf{R})$  and an electronic wavefunction  $\psi(x, \mathbf{R})$ . While  $\chi(\mathbf{R})$  is independent of the electron positions,  $\psi(x, \mathbf{R})$  depends on the nuclear coordinates parametrically. We assume that the nuclear wavefunction  $\chi(\mathbf{R})$  is more localized around the atomic positions than the electronic wavefunction  $\psi(x, \mathbf{R})$

$$\nabla_I \chi(\mathbf{R}) \gg \nabla_I \psi(x, \mathbf{R}), \quad (2.9)$$

where  $\nabla_I = \partial/\partial \mathbf{R}_I$ . Substituting Eq. (2.8) into Eq. (2.7) and recognizing that  $\hat{T}_e \psi(x, \mathbf{R}) \chi(\mathbf{R}) = \chi(\mathbf{R}) \hat{T}_e \psi(x, \mathbf{R})$ , one obtains the following equation<sup>\*2</sup>:

$$E \psi(x, \mathbf{R}) \chi(\mathbf{R}) = \left[ \hat{T}_n + \hat{T}_e + \hat{V}_{ee} + \hat{V}_{nn} + \hat{V}_{en} \right] \psi(\mathbf{x}, \mathbf{R}) \chi(\mathbf{R}) \quad (2.11)$$

$$= \chi(\mathbf{R}) \left[ \hat{T}_e + \hat{V}_{ee} + \hat{V}_{en} \right] \psi(\mathbf{x}, \mathbf{R}) + \hat{T}_n \psi(\mathbf{x}, \mathbf{R}) \chi(\mathbf{R}) + \psi(\mathbf{x}, \mathbf{R}) \hat{V}_{nn} \chi(\mathbf{R}). \quad (2.12)$$

Using Eq. (2.9) we acquire

$$\hat{T}_n \psi(x, \mathbf{R}) \chi(\mathbf{R}) = \chi(\mathbf{R}) \hat{T}_n \psi(x, \mathbf{R}) + \psi(x, \mathbf{R}) \hat{T}_n \chi(\mathbf{R}) \simeq \psi(x, \mathbf{R}) \hat{T}_n \chi(\mathbf{R}). \quad (2.13)$$

Substituting Eq. (2.13) into Eq. (2.12) leads to

$$E \psi(x, \mathbf{R}) \chi(\mathbf{R}) = \chi(\mathbf{R}) \left[ \hat{T}_e + \hat{V}_{ee} + \hat{V}_{en} \right] \psi(x, \mathbf{R}) + \psi(x, \mathbf{R}) \left[ \hat{T}_n + \hat{V}_{nn} \right] \chi(\mathbf{R}). \quad (2.14)$$

Dividing both sides by  $\psi(x, \mathbf{R}) \chi(\mathbf{R})$  give us

$$E - \frac{\left[ \hat{T}_n + \hat{V}_{nn} \right] \chi(\mathbf{R})}{\chi(\mathbf{R})} = \frac{\left[ \hat{T}_e + \hat{V}_{ee} + \hat{V}_{en} \right] \psi(x, \mathbf{R})}{\psi(x, \mathbf{R})} \quad (2.15)$$

Since the left-hand side depends only on  $\mathbf{R}$ , the right-hand side is also a  $\mathbf{R}$ -only function. Let us denote this function as  $\varepsilon(\mathbf{R})$  and we get separate equations for  $\psi(x, \mathbf{R})$  and  $\chi(\mathbf{R})$  as

$$\left[ \hat{T}_e + \hat{V}_{ee} + \hat{V}_{en} \right] \psi(x, \mathbf{R}) = \varepsilon(\mathbf{R}) \psi(x, \mathbf{R}) \quad (2.16)$$

$$\left[ \hat{T}_n + \hat{V}_{nn} + \varepsilon(\mathbf{R}) \right] \chi(\mathbf{R}) = E \chi(\mathbf{R}). \quad (2.17)$$

Equation (2.16) is nothing but an Schrödinger equation for an electronic Hamiltonian at fixed nuclei positions  $\mathbf{R}$ ,

$$\hat{H}_e(\mathbf{R}) = \hat{T}_e + \hat{V}_{ee}(\mathbf{r}) + \hat{V}_{en}(\mathbf{r}, \mathbf{R}), \quad (2.18)$$

with eigenfunctions  $\psi(x, \mathbf{R})$  and eigenvalues  $\varepsilon(\mathbf{R})$ . For each solution  $\varepsilon(\mathbf{R})$ , we have a nuclei Schrödinger equation Eq. (2.17).

## 2.2 Hellmann-Feynman Theorem

Apart from the previous section, we consider a more general Hamiltonian, which depends on some parameter  $\lambda$ . It is expressed as  $\hat{H}(\lambda)$  with eigenstates  $|\Psi(\lambda)\rangle$

$$\hat{H}(\lambda) |\Psi(\lambda)\rangle = E(\lambda) |\Psi(\lambda)\rangle. \quad (2.19)$$

The normalization condition is satisfied for all  $\lambda$

$$\langle \Psi(\lambda) | \Psi(\lambda) \rangle = 1. \quad (2.20)$$

---

<sup>\*2</sup> We also utilize the obvious relationship

$$V_{en} \psi(\mathbf{x}, \mathbf{R}) \chi(\mathbf{R}) = \chi(\mathbf{R}) V_{en} \psi(\mathbf{x}, \mathbf{R}) \quad (2.10)$$

etc.

The derivative of the eigenvalue  $E$  by  $\lambda$  can be obtained as follows

$$\frac{dE}{d\lambda} = \frac{d}{d\lambda} \langle \Psi | \hat{H} | \Psi \rangle \quad (2.21)$$

$$= \left\langle \frac{d\Psi}{d\lambda} \middle| \hat{H} \middle| \Psi \right\rangle + \left\langle \Psi \middle| \frac{d\hat{H}}{d\lambda} \middle| \Psi \right\rangle + \left\langle \Psi \middle| \hat{H} \middle| \frac{d\Psi}{d\lambda} \right\rangle \quad (2.22)$$

$$(2.23)$$

Using Eq. (2.19) for the first and third term yields

$$\frac{dE}{d\lambda} = E \left\langle \frac{d\Psi}{d\lambda} \middle| \Psi \right\rangle + \left\langle \Psi \middle| \frac{d\hat{H}}{d\lambda} \middle| \Psi \right\rangle + E \left\langle \Psi \middle| \frac{d\Psi}{d\lambda} \right\rangle \quad (2.24)$$

$$= E \frac{d}{d\lambda} \langle \Psi | \Psi \rangle + \left\langle \Psi \middle| \frac{d\hat{H}}{d\lambda} \middle| \Psi \right\rangle. \quad (2.25)$$

Using Eq. (2.20) to the first term, we arrive at

$$\frac{dE}{d\lambda} = \left\langle \Psi \middle| \frac{d\hat{H}}{d\lambda} \middle| \Psi \right\rangle. \quad (2.26)$$

The above equation is the well-known Hellmann-Feynman theorem [105]. One application of the theorem is the calculation of atomic forces, and the force calculated by this method is specifically called the Hellmann-Feynman force. Returning to the Hamiltonian Eq. (2.1), we can take the nuclear coordinate  $\mathbf{R}_I$  as the parameter  $\lambda$ . The force acting on atom  $I$  is then

$$\mathbf{F}_I = -\frac{dE}{d\mathbf{R}_I} = -\left\langle \Psi \middle| \frac{d\hat{H}}{d\mathbf{R}_I} \middle| \Psi \right\rangle \quad (2.27)$$

Since only  $\hat{V}_{en}$  and  $\hat{V}_{nn}$  depend on  $\mathbf{R}_I$  among the Hamiltonian Eq. (2.1), we have

$$\mathbf{F}_I = -\left\langle \Psi \middle| \frac{dV_{nn}}{d\mathbf{R}_I} \middle| \Psi \right\rangle - \left\langle \Psi \middle| \frac{dV_{en}}{d\mathbf{R}_I} \middle| \Psi \right\rangle \quad (2.28)$$

$$= -\left\langle \Psi \middle| \sum_{J \neq I} \frac{Z_I Z_J e^2 (\mathbf{R}_I - \mathbf{R}_J)}{|\mathbf{R}_I - \mathbf{R}_J|^3} \middle| \Psi \right\rangle + \left\langle \Psi \middle| \sum_i \frac{Z_I e^2 (\mathbf{R}_I - \mathbf{r}_i)}{|\mathbf{R}_I - \mathbf{r}_i|^3} \middle| \Psi \right\rangle \quad (2.29)$$

$$= -\sum_{J \neq I} Z_I Z_J e^2 \frac{\mathbf{R}_I - \mathbf{R}_J}{|\mathbf{R}_I - \mathbf{R}_J|^3} + Z_I e^2 \int d\mathbf{r} n(\mathbf{r}) \frac{\mathbf{R}_I - \mathbf{r}}{|\mathbf{R}_I - \mathbf{r}|^3}, \quad (2.30)$$

where  $\rho(\mathbf{r})$  is the electron density. Thus, the force acting on an atom  $I$  from all electrons and other atoms is equal to that calculated from classical electromagnetism, where nuclei and electrons are treated as point charges. It is called the electrostatic theorem [105]. Evaluation of Eq. (2.30) is more efficient than calculating  $dE/d\mathbf{R}$  directly because it only requires  $n(\mathbf{r})$  at one fixed nuclei coordinates  $\mathbf{R}$ .

## 2.3 Born-Oppenheimer Molecular Dynamics Simulation

Using the BO approximation, one can consider molecular dynamics methods based on quantum mechanics. When both nuclei and electrons evolve in time according to quantum mechanics, it is necessary to solve the time-dependent Schrödinger equation. However, as we saw earlier, the time scales of nuclei and electrons are very different, and the BO approximation separates them. It allows the nuclei to evolve in time by the classical Newton's equation, and the forces acting on the nucleus are determined by solving a time-independent Schrödinger equation for electrons. The BO approximation ensures that the electrons are instantaneously in the ground state every time the nuclei move. The Born-Oppenheimer molecular dynamics (BOMD) method is then defined by

$$M_I \ddot{\mathbf{R}}_I(t) = -\nabla_I \min_{\Psi_0} \langle \Psi_0 | \hat{H}_e | \Psi_0 \rangle \quad (2.31)$$

$$\hat{H}_e |\Psi_0\rangle = E_0 |\Psi_0\rangle, \quad (2.32)$$

where  $|\Psi_0\rangle$  is the electronic ground state and  $E_0$  is the corresponding electronic energy. The definition of BOMD is conceptual, and various methods can be used for electronic ground state calculations. However, the computational cost of obtaining the electronic ground state is usually very high due to the diagonalization of the Hamiltonian, limiting the system size and time scale to which BOMD can apply. DFT, which we will discuss in the next section, is one of the possible electronic structure calculations.

## 2.4 Density Functional Theory

DFT describes energy as a functional of density. The Hohenberg-Kohn (HK) theorem in 1964 [106] serves as the theoretical cornerstone, which proves the existence of one-to-one mapping between ground state electronic densities  $n_0(\mathbf{r})$  and external potentials  $v_{\text{ext}}(\mathbf{r})$ . As a direct consequence, the variational principle for the ground state energy holds, and minimizing a specific functional  $E[n]$  across all electronic densities  $n(\mathbf{r})$  yields the exact ground state energy  $E_0$ . Although the electron density must be linked to the Hamiltonian  $\hat{H}_e$  associated with a certain external potential  $v_{\text{ext}}$  ( $v$ -representability) in the original derivation by HK, the condition can be loosed using the constrained search approach [107–109]. The HK theorem tells us nothing about the form of the functional  $E[n]$ . Thus, in order to make practical use of DFT, Kohn-Sham (KS) proposed the concept of a noninteracting reference system with an external potential  $v_{\text{KS}}$ , known as the KS system, such that the true interacting system and the KS system share the same the ground state energy and density [110]. The noninteracting KS system is described using single-particle orbitals  $\psi_i(r)$  called the KS orbitals. Instead of solving the original interacting system, we solve the self-consistent equations for the KS orbitals, called the KS equation, to obtain the density of the original interacting system. This section first introduces the HK theorem and then describes the KS scheme. The detailed theory of DFT is discussed in reviews [111, 112] and books [113–116]

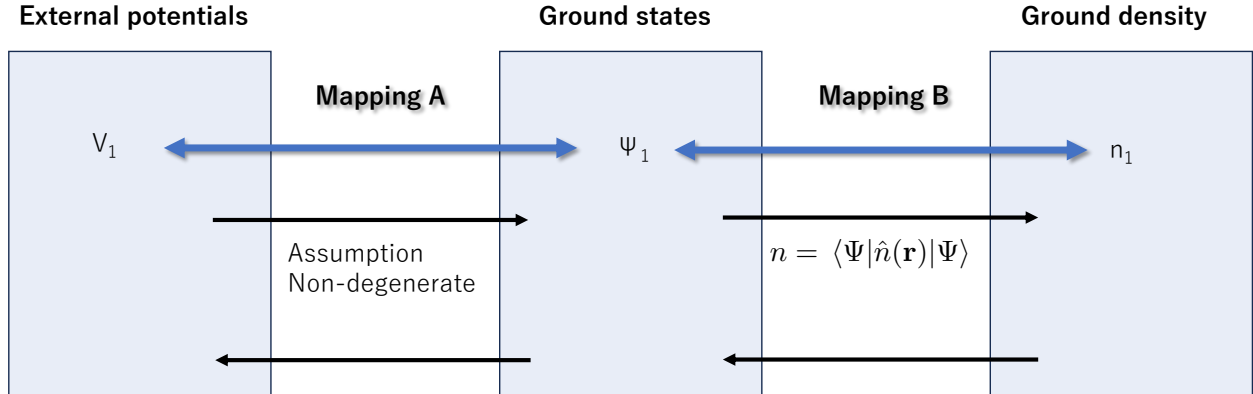


Fig. 2.1: Correspondence between external potentials  $v_i$ , associated ground states  $\Psi$ , and ground state densities  $n_0$  in the case of non-degenerate ground states.

### 2.4.1 Hohenberg-Kohn theorem

#### I. Density as basic variable

We discuss the system composed of  $N$  interacting spin-1/2 particles with a given external potential  $v_{\text{ext}}(\mathbf{r})$  and a particle-particle interaction  $v_{\text{int}}(\mathbf{r})$ . Although we consider electron systems interacting under the Coulomb forces of the nuclei in practical calculations, we are not concerned with the type of particle or interaction in the current discussion. The only assumption is that  $v_{\text{int}}$  is symmetric,  $v_{\text{int}}(\mathbf{r}, \mathbf{r}') = v_{\text{int}}(\mathbf{r}', \mathbf{r})$  and independent of spin. The Hamiltonian has three terms

$$\hat{H}_e = \hat{T}_e + \hat{V}_{\text{ext}} + \hat{V}_{\text{int}}, \quad (2.33)$$

where the kinetic energy  $\hat{T}_e$ , the external potential  $\hat{V}_{\text{ext}}$ , and the particle-particle interaction  $\hat{V}_{\text{int}}$  can be written as follows

$$\hat{T}_e = -\sum_{i=1}^N \frac{(-i\hbar\nabla_i)^2}{2m} = \frac{-\hbar^2}{2m} \sum_{\sigma} \int d\mathbf{r} \psi^{\dagger}(\mathbf{r}\sigma) \nabla^2 \psi(\mathbf{r}\sigma) \quad (2.34)$$

$$\hat{V}_{\text{ext}} = \sum_{i=1}^N v_{\text{ext}}(\mathbf{r}_i) = \int d\mathbf{r} v_{\text{ext}}(\mathbf{r}) \hat{n}(\mathbf{r}) \quad (2.35)$$

$$\hat{V}_{\text{int}} = \frac{1}{2} \sum_{j \neq i}^N v_{\text{int}}(\mathbf{r}_i, \mathbf{r}_j) = \frac{1}{2} \sum_{\sigma, \sigma'} \int d\mathbf{r} d\mathbf{r}' \psi^{\dagger}(\mathbf{r}\sigma) \psi^{\dagger}(\mathbf{r}'\sigma') v_{\text{int}}(\mathbf{r}, \mathbf{r}') \psi(\mathbf{r}'\sigma') \psi(\mathbf{r}\sigma). \quad (2.36)$$

The density operator  $\hat{n}(\mathbf{r})$  is defined as

$$\hat{n}(\mathbf{r}) = \sum_i^N \delta(\mathbf{r} - \mathbf{r}_i) = \sum_{\sigma} \hat{\psi}^{\dagger}(\mathbf{r}\sigma) \hat{\psi}(\mathbf{r}\sigma), \quad (2.37)$$

where particle  $i$  resides in the position  $\mathbf{r}_i$  and has spin index  $\sigma_i$  taking  $\pm 1/2$ .  $\hat{\psi}^{\dagger}(\mathbf{r}, \sigma)$  and  $\hat{\psi}(\mathbf{r}, \sigma)$  are the creation and annihilation operators.

The many-body Schrödinger equation is

$$\hat{H}_e |\Psi_0\rangle = E_0 |\Psi_0\rangle. \quad (2.38)$$

where  $E_0$  is the ground state density and  $|\Psi_0\rangle$  is the corresponding ground state. For simplicity of discussion, we assume that the ground state  $|\Psi_0\rangle$  is not degenerate. This assumption was also used in the original HK paper [106]. The wave function is written as

$$\Psi_0(\mathbf{r}_1, \sigma_1, \dots, \mathbf{r}_N, \sigma_N) = \langle \mathbf{r}_1, \sigma_1, \dots, \mathbf{r}_N, \sigma_N | \Psi_0 \rangle, \quad (2.39)$$

and the electronic density in the ground state  $|\Psi_0\rangle$  is

$$n_0(\mathbf{r}) = \langle \Psi_0 | \hat{n}(\mathbf{r}) | \Psi_0 \rangle = \sum_{\sigma, \sigma_2, \dots, \sigma_N} \int d\mathbf{r}_2 \dots d\mathbf{r}_N |\psi_0(\mathbf{r}, \sigma, \mathbf{r}_2, \sigma_2, \dots, \mathbf{r}_N, \sigma_N)|^2 \quad (2.40)$$

On top of these definitions, we introduce the first theorem by HK.

**Theorem 1** (Hohenberg and Kohn [106]). *Assume the two-body interaction is given and the ground state is not degenerate. There is the one-to-one correspondence between the ground-state density  $n_0$  and the external potential  $v_{\text{ext}}$  <sup>\*3</sup>.*

We note here about external potentials and states. An external potential plus an arbitrary constant gives the same state, and these external potentials are considered identical. Similarly, the state is treated as the same even if a phase factor is added as  $|\Psi'\rangle = e^{i\theta} |\Psi\rangle$ .

*Proof.* The proof is in two parts. First, we prove the one-to-one correspondence between the external potential and the ground state (A), then between the ground state and the density (B). Once these two mappings are proved, the correspondence between the external potential and the density is proven. Figure 2.1 illustrates these correspondence. More specifically, one must show the uniqueness of the following four mappings:

- A-1 there exists only one  $|\Psi_0\rangle$  for given  $v_{\text{ext}}$ .
- A-2 there exists only one  $v_{\text{ext}}$  for given  $|\Psi_0\rangle$ .
- B-1 there exists only one  $n$  for given  $|\Psi_0\rangle$ .
- B-2 there exists only one  $|\Psi_0\rangle$  for given  $n$ .

We start with the part (A). From our assumption of non-degenerate ground states, there exists only one  $|\Psi_0\rangle$  for given  $v_{\text{ext}}$  (A-1). Accordingly, it is enough to show that no two potentials  $v_{\text{ext}}$  and  $v'_{\text{ext}}$ , which differ by more than a constant, have the same ground state  $|\Psi\rangle$  (A-2). The proof is based on a *reductio ad absurdum*. Let us assume that two different potentials  $v_{\text{ext}}$  and  $v'_{\text{ext}} \neq v_{\text{ext}} + \text{const.}$  have the same ground state  $|\Psi_0\rangle$ , which thus satisfies two Schrödinger equations,

$$\hat{H}_e |\Psi_0\rangle = [\hat{T} + \hat{V}_{\text{int}} + \hat{V}_{\text{ext}}] |\Psi_0\rangle = E_0 |\Psi_0\rangle, \quad (2.41)$$

$$\hat{H}'_e |\Psi_0\rangle = [\hat{T} + \hat{V}_{\text{int}} + \hat{V}'_{\text{ext}}] |\Psi_0\rangle = E'_0 |\Psi_0\rangle. \quad (2.42)$$

<sup>\*3</sup> It is implicitly assumed that the density  $n$  is a solution of the Schrödinger equation.

Subtraction of Eq. (2.41) and Eq. (2.42) yields

$$[\hat{V}_{\text{ext}} - \hat{V}'_{\text{ext}}] |\Psi_0\rangle = [E_0 - E'_0] |\Psi_0\rangle. \quad (2.43)$$

Upon applying  $\langle\Psi_0|$  from the right-hand-side one obtains

$$\sum_i^N (v_{\text{ext}}(\mathbf{r}_i) - v'_{\text{ext}}(\mathbf{r}_i)) = E_0 - E'_0 \quad (2.44)$$

for all points  $\mathbf{r}_i$  for which the wavefunction  $\Psi_0(\mathbf{r}_1, \dots, \mathbf{r}_N)$  does not vanish. The right-hand side is constant, but the left-hand side is not constant from the assumption; this is a contradiction. Hence, the proof by contradiction shows the uniqueness of the map A, which states the one-to-one relation between  $v_{\text{ext}}$  and  $n$ .

We next contemplate the second part of the proof. From the relationship between a density and a state Eq. (2.40), the map (B-1) is obvious, so we focus on the map (B-2). The proof runs as follows and is again based on *reductio ad absurdum*. Assume that two different states  $|\Psi_0\rangle$  and  $|\Psi'_0\rangle$  yield the same density  $n_0(\mathbf{r})$  as

$$n_0(\mathbf{r}) = \langle\Psi_0|\hat{n}(\mathbf{r})|\Psi_0\rangle = \langle\Psi'_0|\hat{n}(\mathbf{r})|\Psi'_0\rangle. \quad (2.45)$$

From the mapping (A), they connect to two external potentials  $v_{\text{ext}}$  and  $v'_{\text{ext}}$ , which differ by more than a constant. Two Hamiltonians are  $\hat{H} = \hat{T} + \hat{V}_{\text{int}} + \hat{V}_{\text{ext}}$  and  $\hat{H}' = \hat{T} + \hat{V}_{\text{int}} + \hat{V}'_{\text{ext}}$  with corresponding ground state energies,  $E_0$  and  $E'_0 (\neq E_0)$ ,

$$E_0 = \langle\Psi|\hat{H}|\Psi\rangle \quad (2.46)$$

$$E'_0 = \langle\Psi'|\hat{H}'|\Psi'\rangle. \quad (2.47)$$

The Ritz variational principle leads to an inequality

$$E_0 = \langle\Psi_0|\hat{H}|\Psi_0\rangle < \langle\Psi'_0|\hat{H}|\Psi'_0\rangle \quad (2.48)$$

$$= \langle\Psi'_0|(\hat{H}' + \hat{V}_{\text{ext}} - \hat{V}'_{\text{ext}})|\Psi'_0\rangle = E'_0 + \langle\Psi'_0|(\hat{V}_{\text{ext}} - \hat{V}'_{\text{ext}})|\Psi'_0\rangle. \quad (2.49)$$

Utilizing Eq. (2.35) and (2.45) yields

$$E_0 < E'_0 + \int (v_{\text{ext}}(\mathbf{r}) - v'_{\text{ext}}(\mathbf{r})) n(\mathbf{r}) d\mathbf{r}. \quad (2.50)$$

Similarly, one also reaches

$$E'_0 < E_0 + \int (v'_{\text{ext}}(\mathbf{r}) - v_{\text{ext}}(\mathbf{r})) n(\mathbf{r}) d\mathbf{r}. \quad (2.51)$$

Addition of Eq. (2.50) and (2.51) leads to the inconsistency

$$E_0 + E'_0 < E'_0 + E_0. \quad (2.52)$$

Therefore, we conclude that the map B is unique, which states a one-to-one correspondence between  $|\Psi_0\rangle$  and  $n_0$ . The above proofs of maps A and B substantiate the one-to-one correspondence between the external potential and the density, which is HK's claim.  $\square$

As can be seen from the above proof, if one of the external potential  $v_{\text{ext}}$ , the non-degenerate ground state  $|\Psi_0\rangle$ , and the associated ground state density  $n_0$  is determined, the other two are automatically identified. In the DFT framework, we choose the ground state density as the basic variable, and the ground state is a functional of  $n$  as  $|\Psi[n]\rangle$ . Substituting any ground state density  $n_0$  outputs the corresponding ground state  $|\Psi_0\rangle$  as

$$|\Psi_0\rangle = |\Psi[n_0]\rangle. \quad (2.53)$$

As  $v_{\text{ext}}$  is not necessary to build the functional  $|\Psi[n]\rangle$ , the same  $|\Psi[n]\rangle$  can be used for all systems as long as the particle interaction  $v_{\text{int}}$  is the same. From Eq. (2.53), any ground state observable is also a density functional. In particular, the ground state energy is a functional of the ground state density  $n$ :

$$E[n] = \langle\Psi[n]|\hat{H}|\Psi[n]\rangle. \quad (2.54)$$

Therefore, the three components of the ground-state energy in Eq. (2.33) are also functionals of the ground state density

$$E_0[n] = T_e[n] + E_{\text{int}}[n] + E_{\text{ext}}[n] \quad (2.55)$$

$$E_{\text{ext}}[n] = \int d\mathbf{r} n(\mathbf{r}) v_{\text{ext}}(\mathbf{r}), \quad (2.56)$$

where  $T_e$  and  $E_{\text{int}}$  are  $v_{\text{ext}}$ -independent and thus have the same functional form for every system. To make this explicit, one defines the universal HK functional  $F_{\text{HK}}$  as

$$F_{\text{HK}}[n] = T_e[n] + E_{\text{int}}[n] = \langle \Psi[n] | (\hat{T} + \hat{V}_{\text{int}}) | \Psi[n] \rangle. \quad (2.57)$$

The ground state energy is then expressed as

$$E_0[n] = F_{\text{HK}}[n] + E_{\text{ext}}[n]. \quad (2.58)$$

The definite form of  $F_{\text{HK}}[n]$  lies completely in the dark. For later discussion, it is convenient to separate out the classical part from  $F_{\text{HK}}$ . This is called the Hartree energy

$$E_{\text{H}}[n] = \frac{1}{2} \iint d\mathbf{r} d\mathbf{r}' n(\mathbf{r}) v_{\text{int}}(\mathbf{r}, \mathbf{r}') n(\mathbf{r}') \quad (2.59)$$

including their self-interaction energy. Especially in the case of Coulomb interactions between electrons, we have

$$E_{\text{H}}[n] = \frac{1}{2} \iint d\mathbf{r} d\mathbf{r}' \frac{n(\mathbf{r}) n(\mathbf{r}')}{|\mathbf{r} - \mathbf{r}'|}. \quad (2.60)$$

## II. Variational principle

We have verified that the ground state density is, in principle, a constitutive variable for the ground state density and ground state observables. However, two dominant problems still need to be tackled for the practical calculation of DFT. One is how to obtain the ground-state density, and the other is to determine the specific form of  $E[n]$ , which will be discussed in the consecutive subsection. HK, in the original paper [106], showed that the variational principle holds and that the functional  $E[n]$  delivers the lowest energy, which is the ground state energy  $E_0$ , if and only if the input density is the true ground state density  $n_0$ . While the Ritz variational principle established a variational principle for the wave function  $\Psi$ , HK argued that a similar variational principle holds for the density  $n$ .

**Theorem 2** (Hohenberg and Kohn [106]). *Suppose that the density  $n$  can be obtained by solution of the Schrödinger equation of a system with  $N$  particles<sup>\*4</sup>. The ground state energy functional  $E[n]$  takes a minimum value only if the input density is a true ground state density  $n_0$ . The ground-state energy  $E_0$  holds*

$$E_0 = E[n_0] \leq E[n] \iff E[n_0] = \min_n E[n]. \quad (2.61)$$

*Proof.* The proof is fairly straightforward and combines the uniqueness between  $n_0$  and  $|\Psi_0\rangle$  with the Ritz variational principle. Suppose that the density  $n$  can be obtained by solution of the Schrödinger equation of a  $N$  particles system associated with some  $v_{\text{ext}}$ . According to the Ritz variational principle, the following inequality holds for the ground state  $|\Psi_0\rangle$  and any other state  $|\tilde{\Psi}\rangle$  for a system of  $N$  particles

$$E_0 = \langle \Psi_0 | \hat{H} | \Psi_0 \rangle < \langle \tilde{\Psi} | \hat{H} | \tilde{\Psi} \rangle. \quad (2.62)$$

From the one-to-one relationship between density and state, the densities corresponding to  $|\Psi_0\rangle$  and  $|\tilde{\Psi}\rangle$  are written as  $n_0$  and  $\tilde{n}$ . Obviously,  $n_0$  is the density of the ground state,

$$E_0 = E[n_0] = \langle \Psi_0 | \hat{H} | \Psi_0 \rangle \quad (2.63)$$

$$E[\tilde{n}] = \langle \tilde{\Psi} | \hat{H} | \tilde{\Psi} \rangle. \quad (2.64)$$

---

<sup>\*4</sup> Here we assume that the density  $n$  is describable by some  $v_{\text{ext}}$  (so-called  $v$ -representable).

Thus, we arrive at

$$E_0 = E[n_0] = \langle \Psi_0 | \hat{H} | \Psi_0 \rangle \underset{\text{Eq. (2.62)}}{<} \langle \tilde{\Psi} | \hat{H} | \tilde{\Psi} \rangle = E[\tilde{n}], \quad (2.65)$$

which is the desired result.  $\square$

Here, we deliberate on the mathematical aspects of the HK theorem. In the proof of the HK theorem, the density  $n$  is assumed to be a solution of the Schrödinger equation characterized by a certain  $v_{\text{ext}}$ . Such a density is called  $v$ -representable. As a simple example, for a function  $n$  to be a density,  $n$  must be positive definite  $n(\mathbf{r}) \geq 0$ , and the number of particles must be equal to  $N$

$$\int d\mathbf{r} n(\mathbf{r}) = N. \quad (2.66)$$

It has yet to be discovered which conditions densities must obey in order to be  $v$ -representable. The proofs of HK given so far hold only for  $v$ -representable densities. The energy density functional  $E[n]$  is defined over a  $v$ -representable density, and the trial densities allowed for the variational principle are only  $v$ -representable. Many known densities are not  $v$ -representable, which is a problem in practical calculations. However, as we will show in the following section, this condition can be replaced by the weaker requirement that the density should arise from an antisymmetric wave function without the explicit connection to an external potential. Such densities are called  $N$ -representable, which is a necessary condition for  $v$ -representable. Since almost all practical calculations are associated with some wavefunction methods, the densities that emerge in these applications are  $N$ -representable.

### Constrained-search approach

Levy [107, 108] and Lieb [109] extended HK's original argument to  $N$ -representable densities. Returning to the Ritz variational principle, the ground state energy reads

$$E_0 = \min_{\Psi \rightarrow N} \langle \Psi | \hat{H} | \Psi \rangle, \quad (2.67)$$

where  $\Psi \rightarrow N$  means that the antisymmetric wave function  $\Psi$  is searched among those with  $N$  electrons. Instead of changing the wave function directly, we perform the search Eq. (2.67) in two different steps. In the first step, we only consider trial antisymmetric wave functions that give a certain density  $n$ . In the next step, the search is performed by varying the density  $n$  under the constant number of particles  $N$ . Such a two-step search is called the Levy constrained-search formulation and can be expressed as

$$E_0 = \min_{n \rightarrow N} \left( \min_{\Psi \rightarrow n} \langle \Psi | \hat{H} | \Psi \rangle \right), \quad (2.68)$$

where the inner and outer optimizations correspond to the first and second steps, respectively.

Since  $E_{\text{ext}}[n]$  is determined by the density from Eq. (2.56), it is the same for all wavefunctions producing a particular density and can be separated from the kinetic and electron-electron repulsion contributions

$$E_0 = \min_{n \rightarrow N} \left( \min_{\Psi \rightarrow n} \langle \Psi | (\hat{T} + \hat{V}) | \Psi \rangle + \int d\mathbf{r} v_{\text{ext}} n(\mathbf{r}) \right). \quad (2.69)$$

We introduce the universal functional

$$F[n] = \min_{\Psi \rightarrow n} \langle \Psi | (\hat{T} + \hat{V}) | \Psi \rangle, \quad (2.70)$$

which results in

$$E_0 = \min_{n \rightarrow N} \left( F[n] + \int d\mathbf{r} v_{\text{ext}} n(\mathbf{r}) \right). \quad (2.71)$$

The difference between  $F[n]$  and  $F_{\text{HK}}[n]$  is the domain of density  $n$ . In  $F_{\text{HK}}$ , only  $v$ -representable densities are allowed, while  $F$  is defined for all densities coming from an antisymmetric wave function. The latter does not assume the existence of an external potential  $v_{\text{ext}}$ .

### 2.4.2 Kohn-Sham scheme

The next point we will discuss is how to obtain the form of the functional  $F$  in Eq. (2.70). The exact form is so complicated that some approximation must be used. The primary issue is the kinetic energy  $T$ . There have been attempts to express  $T$  as an explicit functional of the density  $n$ , such as the Thomas-Fermi approximation, but they have not been quantitatively successful. Kohn and Sham suggested a way to approach the universal functional in 1965 [110]. Their idea is to give up directly evaluating  $T$  and instead introduce the concept of a noninteracting reference system built from a set of single-particle orbitals of which the kinetic energy can be exactly calculated. Although the remaining part is unidentified, it is so diminutive that we can rely on some approximation to compute it with satisfying accuracy.

#### Noninteracting system

Before introducing the KS equations, we consider a system of noninteracting  $N$  electrons with an external potential  $v_{\text{KS}}(\mathbf{r})$ , which we will later refer to as the KS system,

$$\hat{H}_s = \hat{T} + \hat{V}_s \quad (2.72)$$

$$\hat{V}_s = \int d\mathbf{r} \hat{n}(\mathbf{r}) v_{\text{KS}}(\mathbf{r}), \quad (2.73)$$

where  $\hat{T}$  is the kinetic energy. The ground state energy  $E_{s0}$  and  $N$ -particle ground state  $|\Psi_0\rangle$ , which is assumed to be non-degenerate, satisfy the Schrödinger equation

$$\hat{H}_s |\Psi\rangle = E_{s0} |\Psi\rangle. \quad (2.74)$$

Since the system is not interacting, its ground state wavefunction  $\Psi_0(\mathbf{r}_1\sigma_1, \dots, \mathbf{r}_N\sigma_N)$  is rigorously represented by the Slater determinant,

$$\Psi_0(\mathbf{r}_1\sigma_1, \dots, \mathbf{r}_N\sigma_N) = \langle \mathbf{r}_1\sigma_1, \dots, \mathbf{r}_N\sigma_N | \Psi_0 \rangle \quad (2.75)$$

$$= \frac{1}{\sqrt{N!}} \det |\psi_1(\mathbf{r}_1\sigma_1), \psi_2(\mathbf{r}_2\sigma_2), \dots, \psi_N(\mathbf{r}_N\sigma_N)|, \quad (2.76)$$

where  $\psi_i$ , ( $i = 1, 2, \dots, N$ ) is the solutions of the single-particle Schrödinger equation,

$$\hat{h}_s \psi_i(\mathbf{r}\sigma) = \varepsilon_i \psi_i(\mathbf{r}\sigma) \quad (2.77)$$

$$\hat{h}_s = -\frac{\hbar^2 \nabla^2}{2m} + v_{\text{KS}}(\mathbf{r}). \quad (2.78)$$

We have the standard orthonormal condition for  $\psi_i$

$$\int d\mathbf{r} \psi_i(\mathbf{r}) \psi_j(\mathbf{r}) = \delta_{ij}. \quad (2.79)$$

The eigenvalues  $\varepsilon_i$  are energetically lowest and assumed to be ordered as

$$\varepsilon_1 \leq \varepsilon_2 \leq \dots \leq \varepsilon_N. \quad (2.80)$$

Thanks to the Slater determinant, the ground state density corresponding to Eq. (2.76) can be expressed as

$$n_{s0}(\mathbf{r}) = \sum_{\sigma} \sum_{i=1}^N |\psi_i(\mathbf{r}\sigma)|^2 \quad (2.81)$$

A significant benefit of introducing noninteracting systems is that the total kinetic energy  $T_s$  can be written straightforwardly using single-particle orbitals,

$$T_s = \langle \Psi_0 | \hat{T} | \Psi_0 \rangle = \sum_{\sigma} \sum_{i=1}^N \int d\mathbf{r} \psi_i^*(\mathbf{r}\sigma) \frac{(-i\hbar \nabla)^2}{2m} \psi_i(\mathbf{r}\sigma). \quad (2.82)$$

The ground state energy is thus

$$E_{s0} = \langle \Psi_0 | \hat{H}_s | \Psi_0 \rangle = \langle \Psi_0 | \hat{T} | \Psi_0 \rangle + \langle \Psi_0 | \hat{V}_s | \Psi_0 \rangle \quad (2.83)$$

$$= \sum_{\sigma} \sum_{i=1}^N \int d\mathbf{r} \psi_i^*(\mathbf{r}\sigma) \frac{(-i\hbar \nabla)^2}{2m} \psi_i(\mathbf{r}\sigma) + \int d\mathbf{r} v_{\text{KS}}(\mathbf{r}) n(\mathbf{r}). \quad (2.84)$$

Since the HK theorem is valid independent of the particle interaction  $v_{\text{int}}(\mathbf{r}, \mathbf{r}')$ , it holds for noninteracting systems. Similar to the discussion of Eq. (2.55), one can define the HK ground state energy functional of noninteracting systems,

$$E_s[n] = \langle \Psi[n] | \hat{T} + \hat{V}_s | \Psi[n] \rangle = \langle \Psi[n] | \hat{T} | \Psi[n] \rangle + \int d\mathbf{r} v_{\text{KS}}(\mathbf{r}) n(\mathbf{r}) \equiv T_s[n] + \int d\mathbf{r} v_{\text{KS}}(\mathbf{r}) n(\mathbf{r}), \quad (2.85)$$

where  $T_s[n]$  is the kinetic energy functional of noninteracting systems related to a Hamiltonian in Eq. (2.72). We note that single-particle wave functions  $\psi_i$  are also functionals of the ground-state density  $n$  using the same argument as the HK theorem.

### Kohn-Sham equation

We again discuss the interacting system Eq. (2.33). Assume that for an electron density  $n_0(\mathbf{r})$  associated with any external potential  $v_{\text{ext}}$ , there is an external potential  $v_{\text{KS}}$  of a noninteracting system that reproduces the same density  $n_0(\mathbf{r})$ . One calls this auxiliary noninteracting system of Eq. (2.72) as the KS system. Whether such a KS system actually exists for arbitrary  $n_0$ , so-called noninteracting  $v$ -representability, is discussed by several authors [117–119]. Using Eq. (2.81), we can represent the ground state density of the interacting system in terms of the single-particle orbitals  $\psi_i$  of the KS system,

$$n_0(\mathbf{r}) = n_{0s}(\mathbf{r}) = \sum_{\sigma} \sum_{i=1}^N |\psi_i(\mathbf{r}\sigma)|^2. \quad (2.86)$$

Of course, the noninteracting kinetic energy in Eq. (2.82) is not equal to the true kinetic energy of the interacting system in Eq. (2.55), even if the systems share the same density. KS introduced the following disintegration of the total energy functional

$$E[n] = T[n] + E_{ee}[n] + E_{\text{ext}}[n] \quad (2.87)$$

$$= T_s[n] + E_H[n] + E_{\text{ext}}[n] + E_{\text{XC}}[n], \quad (2.88)$$

where  $E_{\text{XC}}$ , the so-called exchange-correlation energy is defined as

$$E_{\text{XC}} = (T - T_s) + (E_{ee} - E_H). \quad (2.89)$$

$E_{\text{XC}}$ , which contains everything that is unknown, is composed of two parts: The difference of the kinetic energy of the true interacting system and the noninteracting KS system, and the difference between the true electron interaction and the classical Coulomb energy. The actual calculations make appropriate approximations to  $E_{\text{XC}}$ , but the important thing is that  $T_s$ ,  $E_H$ , and  $E_{\text{ext}}$  can be evaluated accurately and that they usually dominate over  $E_{\text{XC}}$ . The HK theorem for interacting systems ensures that  $E[n]$  is a density functional, and  $T_s$  is a density functional as a result of the HK theorem for noninteracting systems. In contrast,  $E_H$  and  $E_{\text{ext}}$  are explicit density functionals. Therefore,  $n$  should be simultaneously interacting and noninteracting  $v$ -representable for the decomposition Eq. (2.88).

Our next task is determining single-particle orbitals  $\psi_i$ , and thus  $n_0$ . For this purpose, we consider the variational principle for the energy functional  $E[n]$

$$\left. \frac{\delta E[n]}{\delta n} \right|_{n=n_0} = 0. \quad (2.90)$$

Since the  $\psi_i$  are functionals of the density, we can consider a variation  $\delta\psi_i$  of  $\psi_i$  corresponding to  $n_0 + \delta n$ . From Eq. (2.81), they are related as

$$\delta n(\mathbf{r}) = \sum_i \sum_{\sigma} \{ \delta\psi_i^*(\mathbf{r}, \sigma) \psi_i(\mathbf{r}, \sigma) + \psi_i^*(\mathbf{r}, \sigma) \delta\psi_i(\mathbf{r}, \sigma) \} \quad (2.91)$$

The normalization condition for the single-particle wavefunction Eq. (2.79) yields

$$0 = \int d\mathbf{r} |\psi_i(\mathbf{r}\sigma) + \delta\psi_i(\mathbf{r}\sigma)|^2 - \int d\mathbf{r} |\psi_i(\mathbf{r}\sigma)|^2 \quad (2.92)$$

$$= \int d\mathbf{r} \{ \delta\psi_i^*(\mathbf{r}\sigma) \psi_i(\mathbf{r}\sigma) + \delta\psi_i(\mathbf{r}\sigma) \psi_i^*(\mathbf{r}\sigma) \} \quad (2.93)$$

Now, we examine the individual components of  $\delta E[n]/\delta n$ . The functional derivative of the Hartree (Eq. (2.59)) and the external potential energy (Eq. (2.59)) are easily calculated as

$$\frac{\delta E_H[n]}{\delta n}(\mathbf{r}) = \int d\mathbf{r}' v_{\text{int}}(\mathbf{r}, \mathbf{r}') n(\mathbf{r}') \quad (2.94)$$

$$\frac{\delta E_{\text{ext}}[n]}{\delta n}(\mathbf{r}) = v_{\text{ext}}(\mathbf{r}) \quad (2.95)$$

We utilize Eq. (2.82) for  $T_s$ . To first order in the deviation  $\psi_i$  and thus  $\delta n$  one obtains

$$\delta T_s[n] = \sum_{\sigma} \sum_{i=1}^N \int d\mathbf{r} \left\{ \delta \psi_i^*(\mathbf{r}\sigma) \frac{(-i\hbar\nabla)^2}{2m} \psi_i(\mathbf{r}\sigma) + \psi_i^*(\mathbf{r}\sigma) \frac{(-i\hbar\nabla)^2}{2m} \delta \psi_i(\mathbf{r}\sigma) \right\} \quad (2.96)$$

Applying the partial integration twice to the second term with the assumption that all surface contributions vanish, we get

$$\delta T_s[n] = \sum_{\sigma} \sum_{i=1}^N \int d\mathbf{r} \left\{ \delta \psi_i^*(\mathbf{r}\sigma) \frac{(-i\hbar\nabla)^2}{2m} \psi_i(\mathbf{r}\sigma) + \delta \psi_i(\mathbf{r}\sigma) \frac{(-i\hbar\nabla)^2}{2m} \psi_i^*(\mathbf{r}\sigma) \right\} \quad (2.97)$$

We utilize the one-body Schrödinger equations Eq. (2.77) to eliminate the derivatives

$$\delta T_s[n] = \sum_{\sigma} \sum_{i=1}^N \int d\mathbf{r} [\varepsilon_i - v_s(\mathbf{r})] \{ \delta \psi_i^*(\mathbf{r}\sigma) \psi_i(\mathbf{r}\sigma) + \delta \psi_i(\mathbf{r}\sigma) \psi_i^*(\mathbf{r}\sigma) \}. \quad (2.98)$$

The first term is zero from the normalization condition Eq. (2.93) and the second term can be written in terms of  $\delta n$  using Eq. (2.91)

$$\delta T_s[n] = - \sum_{\sigma} \int d\mathbf{r} v_s(\mathbf{r}) \sum_{i=1}^N \{ \delta \psi_i^*(\mathbf{r}\sigma) \psi_i(\mathbf{r}\sigma) + \delta \psi_i(\mathbf{r}\sigma) \psi_i^*(\mathbf{r}\sigma) \} \quad (2.99)$$

$$= - \int d\mathbf{r} v_s(\mathbf{r}) \delta n(\mathbf{r}) \quad (2.100)$$

Therefore, we finally acquire

$$\frac{\delta T_s[n]}{n(\mathbf{r})} = -v_s(\mathbf{r}). \quad (2.101)$$

Collecting the results Eq. (2.94), (2.95) and (2.101), one ends up

$$-v_{\text{KS}}(\mathbf{r}) + \int d\mathbf{r}' v_{\text{int}}(\mathbf{r}, \mathbf{r}') n(\mathbf{r}') + v_{\text{ext}}(\mathbf{r}) + \frac{\delta E_{\text{XC}}[n]}{\delta n} \Big|_{n=n_0} = 0 \quad (2.102)$$

Thus,  $v_{\text{KS}}$  is written by the quantity of the interacting system as follows

$$v_{\text{KS}}(\mathbf{r}) = \int d\mathbf{r}' v_{\text{int}}(\mathbf{r}, \mathbf{r}') n(\mathbf{r}') + v_{\text{ext}}(\mathbf{r}) + \frac{\delta E_{\text{XC}}[n]}{\delta n} \Big|_{n=n_0} \quad (2.103)$$

$$= v_{\text{ext}}(\mathbf{r}) + v_H[n_0](\mathbf{r}) + v_{\text{XC}}[n_0](\mathbf{r}), \quad (2.104)$$

where  $v_H$  and  $v_{\text{XC}}$  are called the Hartree and xc potential, defined as

$$v_H[n](\mathbf{r}) = \int d\mathbf{r}' v_{\text{int}}(\mathbf{r}, \mathbf{r}') n(\mathbf{r}') \quad (2.105)$$

$$v_{\text{XC}}[n](\mathbf{r}) = \frac{\delta E_{\text{XC}}[n]}{\delta n(\mathbf{r})}. \quad (2.106)$$

The KS equations resulting from insertion of Eq. (2.104) into Eq. (2.77) is

$$\left\{ -\frac{\nabla^2}{2m} + v_{\text{ext}} + v_H[n](\mathbf{r}) + v_{\text{XC}}[n](\mathbf{r}) \right\} \psi_i(\mathbf{r}\sigma) = \varepsilon_i \psi_i(\mathbf{r}\sigma). \quad (2.107)$$

We note that the KS equations Eq. (2.107) are nonlinear because  $v_H$  and  $v_{\text{XC}}$  depend on the density, which is determined by the wavefunctions. We have to solve them self-consistently, similar to the Hartree-Fock equations.

## 2.5 Density Functional Perturbation Theory

We consider how to describe external perturbations within DFT. This theory is called DFPT [11, 120]. Similar to the discussion of the Hellman-Feynman theorem, suppose that the Hamiltonian can be described by the parameter  $\lambda$  as  $\hat{H}(\lambda)$ . Let us consider the change in electron density  $n$  due to the perturbation of  $\lambda$ ,  $\delta n(\mathbf{r})$ . The density functional  $v_{\text{KS}}$  also changes by  $\delta v_{\text{KS}}$ , which is written as

$$\delta v_{\text{KS}}(\mathbf{r}) = \delta v_{\text{ext}}(\mathbf{r}) + \delta v_H[n](\mathbf{r}) + \delta v_{\text{XC}}[n](\mathbf{r}) \quad (2.108)$$

$$= \delta v_{\text{ext}}(\mathbf{r}) + \int d\mathbf{r}' v_{\text{int}}(\mathbf{r}, \mathbf{r}') \delta n(\mathbf{r}') + \frac{\delta v_{\text{XC}}}{\delta n} \delta n(\mathbf{r}). \quad (2.109)$$

We note that  $\delta v_{\text{ext}}(\mathbf{r})$  here represents the change purely due to parameters  $\lambda$  and does not depend on the density  $n$  explicitly. According to the discussion in the previous section, the KS orbitals  $\psi_i$  also change to  $\psi_i + \delta\psi_i$  by the perturbation. The usual perturbation theory for the KS equation Eq. (2.107) can be used to determine  $\delta\psi_i$  [121]. The KS equations for unperturbed and perturbed systems are

$$\hat{h}_s \psi_i(\mathbf{r}\sigma) = \left\{ -\frac{\nabla^2}{2m} + v_{\text{KS}} \right\} \psi_i(\mathbf{r}\sigma) = \varepsilon_i \psi_i(\mathbf{r}\sigma) \quad (2.110)$$

$$\left\{ -\frac{\nabla^2}{2m} + v_{\text{KS}} + \delta v_{\text{KS}} \right\} (\psi_i(\mathbf{r}\sigma) + \delta\psi_i(\mathbf{r}\sigma)) = (\varepsilon_i + \delta\varepsilon_i) (\psi_i(\mathbf{r}\sigma) + \delta\psi_i(\mathbf{r}\sigma)). \quad (2.111)$$

Subtracting Eq. (2.110) and (2.111) and only retaining up to the first order yields the Sternheimer-type equation [122]

$$(\hat{h}_s - \varepsilon_i) \delta\psi_i = -(\delta v_{\text{KS}} - \delta\varepsilon_i) \psi_i. \quad (2.112)$$

From the normalization condition, we have the same equation as Eq. (2.93)

$$0 = \int d\mathbf{r} \{ \delta\psi_i^*(\mathbf{r}\sigma) \psi_i(\mathbf{r}\sigma) + \delta\psi_i(\mathbf{r}\sigma) \psi_i^*(\mathbf{r}\sigma) \}. \quad (2.113)$$

As usually used in perturbation theory, we can impose the stronger constraint

$$0 = \int d\mathbf{r} \delta\psi_i^*(\mathbf{r}\sigma) \psi_i(\mathbf{r}\sigma), \quad (2.114)$$

which means that the perturbed wave function is orthogonal to the original wave function. Keeping this in mind and multiplying  $\psi_i^*$  from the left in Eq. (2.112), we get the first order energy correction

$$\delta\varepsilon_i = \int d\mathbf{r} \psi_i^*(\mathbf{r}\sigma) \delta v_{\text{KS}} \psi_i(\mathbf{r}\sigma) = \langle \psi_i | \delta v_{\text{KS}} | \psi_i \rangle. \quad (2.115)$$

Equation (2.112) differs from ordinary perturbation theory in that  $\delta v_{\text{KS}}$ , which depends on  $\delta n$ , must be solved self-consistently like the KS equations in the unperturbed case.

## Chapter 3

# Anharmonic Phonon Theory

In this chapter, we discuss the theory of anharmonic phonons. In Sec. 3.1 to 3.5, we discuss lattice models based on the famous textbook by Born and Huang [8]. Next, we will discuss phonons by Green's function method in Sec. 3.6 and beyond. In particular, the self-consistent phonon (SCPH) method is discussed in Sec. 3.8 and the dielectric function is discussed in Sec. 3.9.1 and 3.9.2. We follow the notation used in the ALAMODE package [25, 29, 123]

### 3.1 Lattice System

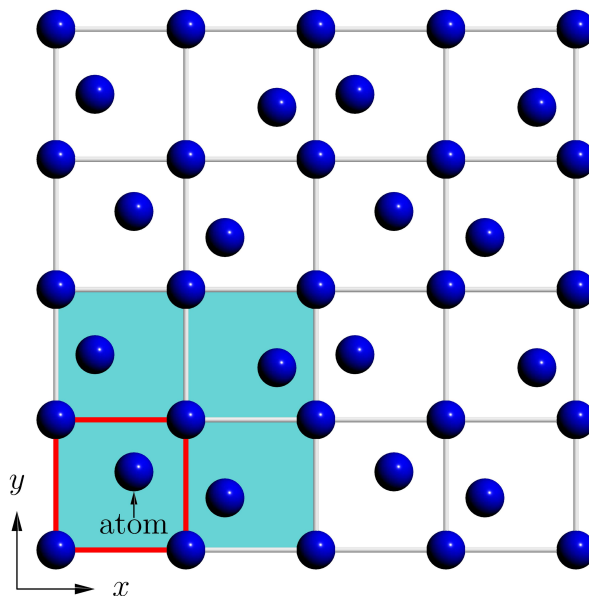


Fig. 3.1: The illustration of the lattice system considered in this section. The blue circles represent atoms, and each square represents a unit cell. Therefore, we have two atoms in the unit cell (the red square). The blue part constitutes a  $2 \times 2$  supercell, which is connected by periodic boundary conditions.

The lattice system considered in this chapter is illustrated in Fig. 3.1, which is composed of supercells with periodic boundary conditions. Physical quantities can be normalized by the volume of the supercell. We deliberate a unit lattice described by the basic lattice vectors  $\mathbf{a}_1$ ,  $\mathbf{a}_2$ , and  $\mathbf{a}_3$ . Let  $\kappa = 1, 2, \dots, N$  be the index of the nuclei, where  $N$  is the number of atoms in the unitcell. The system can be written in terms of  $N_{\text{cell}} = L_1 \times L_2 \times L_3$  iterations of the fundamental lattice, with  $L_i$  being the number of iterations in each  $i$  direction. We call the chunk of unit cells the supercell with the basic vectors  $L_1\mathbf{a}_1$ ,  $L_2\mathbf{a}_2$  and  $L_3\mathbf{a}_1$ . Let  $l = 1, 2, \dots, N_{\text{cell}}$  be the index of  $l$  on this unit lattice. The coordinates of the origin of the lattice  $l$  are denoted by  $\mathbf{x}(l)$  and are called the real lattice vector. This can be expressed in terms of three integers  $l_1$ ,  $l_2$ , and  $l_3$  as

$$\mathbf{x}(l) = l_1\mathbf{a}_1 + l_2\mathbf{a}_2 + l_3\mathbf{a}_3. \quad (3.1)$$

Atoms in a supercell are fully specified by lattice and nuclear indices  $(l, \kappa)$ . The mass of an atom  $\kappa$  belonging to a lattice  $l$  is denoted by  $m_\kappa$  and its coordinates by  $x_\mu(l\kappa)$ , where  $\mu = 1, 2, 3$  are Cartesian indices. The

atomic displacement from the equilibrium position  $x_\mu^0(l\kappa)$  is written as  $u_\mu(l\kappa)$

$$u_\mu(l\kappa) = x_\mu(l\kappa) - x_\mu^0(l\kappa). \quad (3.2)$$

We impose the periodic boundary condition by requiring that the pattern of atomic motion should be the same in all supercells (see Fig. 3.1). Namely, we require that  $u(l, \kappa) = u(l', \kappa)$  if  $l$  and  $l'$  are the same cells in their respective supercells

$$l'_1 = l_1 + cL_1 \quad (3.3)$$

$$l'_2 = l_2 + cL_2 \quad (3.4)$$

$$l'_3 = l_3 + cL_3. \quad (3.5)$$

Then, the energies in all supercells are clearly identical, and only the energy in one supercell needs to be considered. If the atomic displacements from the equilibrium positions  $\mathbf{R}_0$  are small compared with interatomic distances, the total energy of a supercell  $U$  can be written in terms of the Taylor expansion for small displacements  $u_\mu(l\kappa)$  as

$$U = U_0 + U_2 + U_3 + \dots \quad (3.6)$$

$$U_n = \frac{1}{n!} \sum_{(l, \kappa, \mu)}^N \Phi_{\mu_1 \dots \mu_n}(l_1 \kappa_1, \dots, l_n \kappa_n) \times u_{\mu_1}(l_1 \kappa_1) \dots u_{\mu_n}(l_n \kappa_n), \quad (3.7)$$

where the summation over  $l$  is taken over the  $N_{\text{cell}}$  unit cells in the supercell.  $\Phi_n$  is the  $n$ th derivative of the total energy, called the  $n$ th order interatomic force constant (IFC),

$$\Phi_{\mu_1 \dots \mu_n}(l_1 \kappa_1, \dots, l_n \kappa_n) = \left( \frac{\partial U}{\partial u_{\mu_1}(l_1 \kappa_1) \dots \partial u_{\mu_n}(l_n \kappa_n)} \right)_0. \quad (3.8)$$

The index 0 signifies the equilibrium configuration  $x^0$ .  $U_0$  is the total energy at equilibrium state  $x^0$ , and  $U_1 = 0$  since the energy is minimum at the equilibrium state. We point out the two important properties of IFCs. From the periodic boundary condition, the values of IFCs do not change when the same number  $l$  is added to all cell indices as

$$\Phi_{\mu_1 \dots \mu_n}(l_1 \kappa_1, \dots, l_n \kappa_n) = \Phi_{\mu_1 \dots \mu_n}(l_1 + l \kappa_1, \dots, l_n + l \kappa_n). \quad (3.9)$$

If we take  $l = -l_1$ , the first cell variable becomes zero,

$$\Phi_{\mu_1 \dots \mu_n}(l_1 \kappa_1, \dots, l_n \kappa_n) = \Phi_{\mu_1 \dots \mu_n}(0 \kappa_1, l_2 - l_1 \kappa_2, \dots, l_n - l_1 \kappa_n). \quad (3.10)$$

Thus, the first-order IFCs are independent of the cell index, and the second-order IFCs depend only on the difference of the cell indices  $l_2 - l_1$ . In general,  $n$ th-order IFCs depend only on  $n - 1$  cell indices. To make this clear, if necessary, we write them as follows:

$$\Phi_{\mu_1}(l_1 \kappa_1) = \Phi_{\mu_1}(\kappa_1) \quad (3.11)$$

$$\Phi_{\mu_1 \mu_2}(l_1 \kappa_1, l_2 \kappa_2) = \Phi_{\mu_1 \mu_2}(l_2 - l_1, \kappa_1, \kappa_2). \quad (3.12)$$

Second, IFCs have permutation symmetry, as we can change the order of the derivative,

$$\Phi_{\mu_1 \dots \mu_n}(\dots, l_i \kappa_i, \dots, l_j \kappa_j, \dots) = \Phi_{\mu_1 \dots \mu_n}(\dots, l_j \kappa_j, \dots, l_i \kappa_i, \dots). \quad (3.13)$$

## 3.2 Reciprocal Space

For all real lattice vectors  $\mathbf{R}$  defined by Eq. (3.1),  $\mathbf{K}$  satisfying

$$e^{i\mathbf{K} \cdot \mathbf{R}} = 1 \quad (3.14)$$

is called a reciprocal lattice vector. There exist reciprocal lattice basis vectors  $\mathbf{b}_1, \mathbf{b}_2, \mathbf{b}_3$  corresponding to lattice basis vectors  $\mathbf{a}_1, \mathbf{a}_2, \mathbf{a}_3$  such that<sup>\*1</sup>

$$\mathbf{a}_i \cdot \mathbf{b}_j = 2\pi\delta_{ij}. \quad (3.18)$$

The any point satisfying Eq. (3.14) can be expressed in terms of  $\mathbf{b}$  as

$$\mathbf{K}(h) = h_1\mathbf{b}_1 + h_2\mathbf{b}_2 + h_3\mathbf{b}_3 \quad (3.19)$$

with  $h(h_1, h_2, h_3)$  being integers.

For any point  $\mathbf{q}(h) = (h_1, h_2, h_3)$  on the reciprocal lattice space and any lattice point  $\mathbf{x}(l) = (l_1, l_2, l_3)$  on real space, we can construct a function of  $\mathbf{x}(l)$  (or  $\mathbf{q}(h)$ ) as follow:

$$\frac{1}{\sqrt{N_{\text{cell}}}} \exp \left( i\mathbf{q} \left( \frac{h_1}{L_1}, \frac{h_2}{L_2}, \frac{h_3}{L_3} \right) \cdot \mathbf{x}(l) \right) = \frac{1}{\sqrt{N_{\text{cell}}}} \exp \left\{ 2\pi i \left( \frac{h_1 l_1}{L_1} + \frac{h_2 l_2}{L_2} + \frac{h_3 l_3}{L_3} \right) \right\}. \quad (3.20)$$

This expression is invariant if we add integral multiples of  $L_i$  to either  $l_i$  or  $h_i$ . Therefore, if we consider Eq. (3.20) as a function of  $\mathbf{x}(l)$ , it satisfies the periodic condition with respect to  $L_1, L_2$ , and  $L_3$ . On the other hand, considering  $\mathbf{q}(h)$ , all the values of Eq. (3.20) can be obtained if we only consider the following range of  $\mathbf{q}(h)$  (suppose  $L_i$  even):

$$-\frac{L_1}{2} \leq h_1 < \frac{L_1}{2} \quad (3.21)$$

$$-\frac{L_2}{2} \leq h_2 < \frac{L_2}{2} \quad (3.22)$$

$$-\frac{L_3}{2} \leq h_3 < \frac{L_3}{2}. \quad (3.23)$$

If we introduce new variables  $\xi_i = h_i/L_i$ , we can restrict them to the range

$$-\frac{1}{2} \leq \frac{h_1}{L_1}, \frac{h_2}{L_2}, \frac{h_3}{L_3} < \frac{1}{2}. \quad (3.24)$$

The region of the reciprocal space satisfying Eq. (3.24) is called the first Brillouin zone. There are exactly  $N_{\text{cell}}$  sets of  $\xi = (\xi_1, \xi_2, \xi_3)$ . We extend the argument of Eq. (3.19) to  $N_{\text{cell}}$  distinct  $\xi$  satisfying Eq. (3.24) and call them wavenumbers

$$\mathbf{q}(\xi) = \xi_1\mathbf{b}_1 + \xi_2\mathbf{b}_2 + \xi_3\mathbf{b}_3. \quad (3.25)$$

Upon above definitions, let us consider the following function  $\Delta(\mathbf{q})$  in the reciprocal space:

$$\Delta(\mathbf{q}) = \frac{1}{N_{\text{cell}}} \sum_l^{N_{\text{cell}}} \exp(i\mathbf{q} \cdot \mathbf{x}(l)), \quad (3.26)$$

where the summation is over all the  $N_{\text{cell}}$  cells, and  $\mathbf{q}$  is any point in the reciprocal space. The summation over  $l_1, l_2$ , and  $l_3$  can be done using the sum formula of geometric sequences

$$\Delta(\mathbf{q}) = \left( \frac{1 - e^{2\pi i L_1 \xi_1}}{1 - e^{2\pi i \xi_1}} \right) \left( \frac{1 - e^{2\pi i L_2 \xi_2}}{1 - e^{2\pi i \xi_2}} \right) \left( \frac{1 - e^{2\pi i L_3 \xi_3}}{1 - e^{2\pi i \xi_3}} \right). \quad (3.27)$$

The numerator of this function is always zero as  $e^{2\pi i L_i \xi_i} = e^{2\pi i h_i} = 1 (h_i \in \text{integer})$ . On the other hand, the denominator is zero if and only if  $\xi$  is an integer, i.e.,  $\mathbf{q}$  is on the reciprocal grid point ( $h_i$  is a multiple of  $L_i$ ). In this case, every term in the sum of Eq. (3.26) is equal to unity. Hence,  $\Delta(\mathbf{q})$  is given by

$$\Delta(\mathbf{q}) = \begin{cases} 1 & \mathbf{q} = \text{reciprocal lattice points} \\ 0 & \text{otherwise.} \end{cases} \quad (3.28)$$

---

<sup>\*1</sup> Typically,  $\mathbf{b}_i$  are taken as

$$\mathbf{b}_1 = 2\pi \frac{\mathbf{a}_2 \times \mathbf{a}_3}{\mathbf{a}_1 \cdot (\mathbf{a}_2 \times \mathbf{a}_3)} \quad (3.15)$$

$$\mathbf{b}_2 = 2\pi \frac{\mathbf{a}_3 \times \mathbf{a}_1}{\mathbf{a}_1 \cdot (\mathbf{a}_3 \times \mathbf{a}_1)} \quad (3.16)$$

$$\mathbf{b}_3 = 2\pi \frac{\mathbf{a}_1 \times \mathbf{a}_2}{\mathbf{a}_1 \cdot (\mathbf{a}_1 \times \mathbf{a}_2)}. \quad (3.17)$$

As you will see below, this function appears in many equations. The function Eq. (3.26) satisfies a kind of orthogonality relations. For two wavenumbers  $\mathbf{q}_1 = \mathbf{q}(\xi_1)$  and  $\mathbf{q}_2 = \mathbf{q}(\xi_2)$ , we have

$$\sum_l^{N_{\text{cell}}} \left( \frac{1}{\sqrt{N_{\text{cell}}}} \exp(2\pi i \mathbf{q}_2 \cdot \mathbf{x}(l)) \right)^* \left( \frac{1}{\sqrt{N_{\text{cell}}}} \exp(2\pi i \mathbf{q}_1 \cdot \mathbf{x}(l)) \right) = \Delta(-\mathbf{q}_2 + \mathbf{q}_1) \quad (3.29)$$

Under the restriction Eq. (3.24),

$$-\mathbf{q}(\xi_2) + \mathbf{q}(\xi_1) = \mathbf{q}(\xi_1 - \xi_2) \quad (3.30)$$

is a reciprocal lattice vector only for the case  $\mathbf{q}_1 = \mathbf{q}_2$ . Thus it follows from Eq. (3.28) that

$$\sum_l^{N_{\text{cell}}} \left( \frac{1}{\sqrt{N_{\text{cell}}}} \exp(2\pi i \mathbf{q}_2 \cdot \mathbf{x}(l)) \right)^* \left( \frac{1}{\sqrt{N_{\text{cell}}}} \exp(2\pi i \mathbf{q}_1 \cdot \mathbf{x}(l)) \right) = \delta_{\mathbf{q}_1 \mathbf{q}_2} \quad (3.31)$$

if  $\mathbf{q}_1$  and  $\mathbf{q}_2$  are two permitted wave-numbers. This expresses the orthonormal relations between the functions of the type Eq. (3.20).

Similarly, for two cell index  $l$  and  $l'$ , we have orthonormal relations

$$\sum_{\mathbf{q}}^{N_{\text{cell}}} \left( \frac{1}{\sqrt{N_{\text{cell}}}} \exp(2\pi i \mathbf{q} \cdot \mathbf{x}(l)) \right)^* \left( \frac{1}{\sqrt{N_{\text{cell}}}} \exp(2\pi i \mathbf{q} \cdot \mathbf{x}(l')) \right) = \delta_{ll'}. \quad (3.32)$$

where the letter  $N_{\text{cell}}$  signifies that  $\mathbf{q}$  is summed over the  $N_{\text{cell}}$  permitted wave-numbers.

### 3.3 Harmonic Approximation

Restricting the energy expansion Eq. (3.7) to the second order is called the harmonic approximation. In this case, the Hamiltonian can be diagonalized, and independent harmonic oscillators become its energy eigenstates. We start our discussion with the second-order potential energy

$$U_{\text{harm}} = U_2 = \frac{1}{2} \sum_{l_1, \kappa_1, \mu_1} \sum_{l_2, \kappa_2, \mu_2} \Phi_{\mu_1, \mu_2}(l_1 \kappa_1, l_2 \kappa_2) u_{\mu_1}(l_1 \kappa_1) u_{\mu_2}(l_2 \kappa_2). \quad (3.33)$$

The classical equation of motion in arbitrary displaced positions  $u_{\mu}(l\kappa)$  under the potential  $U_{\text{harm}}$  is

$$\begin{aligned} m_{\kappa} \ddot{u}_{\mu}(l\kappa) &= - \frac{\partial U_{\text{harm}}}{\partial u_{\mu}(l\kappa)} \\ &= - \sum_{l_2, \kappa_2, \mu_2} \Phi_{\mu, \mu_2}(l\kappa, l_2 \kappa_2) u_{\mu_2}(l_2 \kappa_2) \end{aligned} \quad (3.34)$$

We introduce the dynamical matrix in which IFCs are normalized by atomic masses

$$D_{\mu_1, \mu_2}(l_1 \kappa_1, l_2 \kappa_2) = \frac{1}{\sqrt{m_{\kappa_1} m_{\kappa_2}}} \Phi_{\mu_1, \mu_2}(l_1 \kappa_1, l_2 \kappa_2), \quad (3.35)$$

and the reduced displacements

$$w_{\mu}(l, \kappa) = \sqrt{m_{\kappa}} u_{\mu}(l, \kappa). \quad (3.36)$$

If the pair  $(l, \kappa)$  is considered a single index, the dynamical matrix can be regarded as a  $3N \times 3N$  dimensional matrix. The potential energy, kinetic energy, and Hamiltonian are written as

$$U_{\text{harm}} = \frac{1}{2} \sum_{l_1, \kappa_1, \mu_1} \sum_{l_2, \kappa_2, \mu_2} D_{\mu_1, \mu_2}(l_1 \kappa_1, l_2 \kappa_2) w_{\mu_1}(l_1 \kappa_1) w_{\mu_2}(l_2 \kappa_2) \quad (3.37)$$

$$T = \frac{1}{2} \sum_{l, \kappa, \mu} m_{\kappa} \dot{u}_{\mu}^2(l\kappa) = \frac{1}{2} \sum_{\kappa, \mu} w_{\mu}^2(l\kappa) = \frac{1}{2} \sum_{\kappa, \mu} w_{\mu}^*(l\kappa) w_{\mu}(l\kappa) \quad (3.38)$$

$$H = T + U_{\text{harm}} = \frac{1}{2} \sum_{l, \kappa, \mu} w_{\mu}^2(l\kappa) + \frac{1}{2} \sum_{l, \kappa, \mu} D_{\mu_1, \mu_2}(l_1 \kappa_1, l_2 \kappa_2) w_{\mu_1}(l_1 \kappa_1) w_{\mu_2}(l_2 \kappa_2). \quad (3.39)$$

In the second line, we used  $w_\mu(l\kappa) = w_\mu^*(l\kappa)$  as  $w_\mu(l\kappa)$  is real. Similarly, the Newton's equation of motion Eq. (3.34) is given by

$$\ddot{w}_\mu(l\kappa) = \sum_{l_2, \kappa_2, \mu_2} D_{\mu, \mu_2}(l\kappa, l_2\kappa_2) w_{\mu_2}(l_2\kappa_2). \quad (3.40)$$

Since the Hamiltonian is a quadratic form of a  $3N \times 3N$  dimensional matrix, diagonalizing the Hamiltonian yields  $3N$  reference oscillations. For this purpose, we express the reduced displacements  $w_\mu(l\kappa)$  in terms of a set of complex variables  $w_\mu(\mathbf{q}, \kappa)$  as follows:

$$w_\mu(l, \kappa) = \frac{1}{\sqrt{N_{\text{cell}}}} \sum_{\mathbf{q}}^{N_{\text{cell}}} w_\mu(\mathbf{q}, \kappa) e^{2\pi i \mathbf{q} \cdot \mathbf{x}(l)}. \quad (3.41)$$

We again notice that the  $\mathbf{q}$  is a wave number, and  $N_{\text{cell}}$  means the summation is taken over all  $N_{\text{cell}}$  wave number satisfying Eq. (3.24). Since reduced displacements are real, the complex conjugate of the above Eq. (3.41) yields

$$w_\mu^*(\mathbf{q}, \kappa) = w_\mu(-\mathbf{q}, \kappa). \quad (3.42)$$

The inverse transformation of Eq. (3.41) can be obtained as follows: First, we multiply both sides of Eq. (3.41) by  $e^{-2\pi i \mathbf{q}' \cdot \mathbf{x}(l)} / \sqrt{N_{\text{cell}}}$  and sum over  $l$

$$\frac{1}{\sqrt{N_{\text{cell}}}} \sum_l w_\mu(l, \kappa) e^{-2\pi i \mathbf{q}' \cdot \mathbf{x}(l)} = \sum_l \left( \frac{1}{\sqrt{N_{\text{cell}}}} \sum_{\mathbf{q}}^{N_{\text{cell}}} w_\mu(\mathbf{q}, \kappa) e^{2\pi i \mathbf{q} \cdot \mathbf{x}(l)} \right) \frac{1}{\sqrt{N_{\text{cell}}}} e^{-2\pi i \mathbf{q}' \cdot \mathbf{x}(l)}. \quad (3.43)$$

Equation (3.31) tells us that the summation over  $l$  in the right-hand side is  $\delta_{\mathbf{q}\mathbf{q}'}$ , and we get

$$w_\mu(\mathbf{q}, \kappa) = \frac{1}{\sqrt{N_{\text{cell}}}} \sum_l w_\mu(l, \kappa) e^{-2\pi i \mathbf{q} \cdot \mathbf{x}(l)}. \quad (3.44)$$

Eq. (3.41) and (3.44) are Fourier transforms between real space and reciprocal lattice space. Similarly, we introduce a transformation for the dynamic matrix. We recall that the second-order IFCs, thus the dynamical matrix, only depend on one cell index  $l_2 - l_1$  as in Eq. (3.12),

$$D_{\mu_1, \mu_2}(l_1\kappa_1, l_2\kappa_2) = D_{\mu_1, \mu_2}(0\kappa_1, l_2 - l_1\kappa_1). \quad (3.45)$$

We then introduce the dynamical matrix in the reciprocal lattice space as

$$D_{\mu_1, \mu_2}(\mathbf{q}, \kappa_1, \kappa_2) = \sum_l^{N_{\text{cell}}} D_{\mu_1, \mu_2}(0\kappa_1, l\kappa_2) e^{-2\pi i \mathbf{q} \cdot \mathbf{x}(l)}. \quad (3.46)$$

We shall show that  $D_{\mu_1, \mu_2}(\mathbf{q}, \kappa_1, \kappa_2)$  is Hermitian. Taking the complex conjugate of Eq. (3.46) and using the fact that IFCs are real yields

$$D_{\mu_1, \mu_2}^*(\mathbf{q}, \kappa_1, \kappa_2) = \sum_l D_{\mu_1, \mu_2}(0\kappa_1, l\kappa_2) e^{+2\pi i \mathbf{q} \cdot \mathbf{x}(l)}. \quad (3.47)$$

Using the permutation symmetry on IFCs Eq. (3.13), thus on the dynamical matrix, i.e.,  $D_{\mu_1, \mu_2}(0\kappa_1, l\kappa_2) = D_{\mu_2, \mu_1}(l\kappa_2, 0\kappa_1)$ , we acquire

$$\begin{aligned} D_{\mu_1, \mu_2}^*(\mathbf{q}, \kappa_1, \kappa_2) &= \sum_l D_{\mu_2, \mu_1}(l\kappa_2, 0\kappa_1) e^{+2\pi i \mathbf{q} \cdot \mathbf{x}(l)} \\ &= \sum_l D_{\mu_2, \mu_1}(0\kappa_2, -l\kappa_1) e^{+2\pi i \mathbf{q} \cdot \mathbf{x}(l)} \\ &= \sum_l D_{\mu_2, \mu_1}(0\kappa_2, l\kappa_1) e^{-2\pi i \mathbf{q} \cdot \mathbf{x}(l)} \\ &= D_{\mu_2, \mu_1}(\mathbf{q}, \kappa_2, \kappa_1). \end{aligned} \quad (3.48)$$

We replace the summation index from  $l$  to  $-l$  in the third line. Equation (3.48) shows that the dynamical matrix is Hermitian.

We express the harmonic potential energy Eq. (3.37) in terms of the complex variables. Substituting Eq. (3.41) into Eq. (3.37) yields

$$\begin{aligned}
U_{\text{harm}} &= \frac{1}{2} \sum_{l_1, \kappa_1, \mu_1} \sum_{l_2, \kappa_2, \mu_2} D_{\mu_1, \mu_2}(l_1 \kappa_1, l_2 \kappa_2) w_{\mu_1}(l_1 \kappa_1) w_{\mu_2}(l_2 \kappa_2) \\
&= \frac{1}{2N_{\text{cell}}} \sum_{l_1, \kappa_1, \mu_1} \sum_{l_2, \kappa_2, \mu_2} \sum_{\mathbf{q}_1, \mathbf{q}_2}^{N_{\text{cell}}} D_{\mu_1, \mu_2}(l_1 \kappa_1, l_2 \kappa_2) w_{\mu_1}(\mathbf{q}_1 \kappa_1) w_{\mu_2}(\mathbf{q}_2 \kappa_2) e^{2\pi i(\mathbf{q}_1 \cdot \mathbf{x}(l_1) + \mathbf{q}_2 \cdot \mathbf{x}(l_2))} \\
&= \frac{1}{2N_{\text{cell}}} \sum_{l_1, \kappa_1, \mu_1} \sum_{l_2, \kappa_2, \mu_2} \sum_{\mathbf{q}_1, \mathbf{q}_2}^{N_{\text{cell}}} D_{\mu_1, \mu_2}(l_1 \kappa_1, l_2 \kappa_2) w_{\mu_1}(\mathbf{q}_1 \kappa_1) w_{\mu_2}(\mathbf{q}_2 \kappa_2) e^{2\pi i(\mathbf{q}_1 + \mathbf{q}_2) \cdot \mathbf{x}(l_2)} e^{-2\pi i(\mathbf{x}(l_2) - \mathbf{x}(l_1)) \cdot \mathbf{q}_1} \\
&= \frac{1}{2N_{\text{cell}}} \sum_{\kappa_1, \mu_1} \sum_{l_2, \kappa_2, \mu_2} \sum_{\mathbf{q}_1, \mathbf{q}_2}^{N_{\text{cell}}} w_{\mu_1}(\mathbf{q}_1 \kappa_1) w_{\mu_2}(\mathbf{q}_2 \kappa_2) e^{2\pi i(\mathbf{q}_1 + \mathbf{q}_2) \cdot \mathbf{x}(l_2)} \left\{ \sum_{l_1} D_{\mu_1, \mu_2}(0 \kappa_1, l_2 - l_1 \kappa_2) e^{-2\pi i(\mathbf{x}(l_2) - \mathbf{x}(l_1)) \cdot \mathbf{q}_1} \right\}.
\end{aligned} \tag{3.49}$$

We used the relation  $\mathbf{q}_1 \cdot \mathbf{x}(l_1) + \mathbf{q}_2 \cdot \mathbf{x}(l_2) = (\mathbf{x}(l_2) - \mathbf{x}(l_1)) \cdot \mathbf{q}_1 + (\mathbf{q}_1 + \mathbf{q}_2) \cdot \mathbf{x}(l_2)$  in the third line. The expression in the curly brackets is independent of the value of  $l_2$ . By replacing the summation index  $l_1$  by  $\bar{l} = l_2 - l_1$  (using  $\mathbf{x}(\bar{l}) = \mathbf{x}(l_2) - \mathbf{x}(l_1)$ ), we can clearly see that it is identical to the reciprocal dynamical matrix Eq. (3.46)

$$U_{\text{harm}} = \frac{1}{2N_{\text{cell}}} \sum_{\kappa_1, \mu_1} \sum_{l_2, \kappa_2, \mu_2} \sum_{\mathbf{q}_1, \mathbf{q}_2}^{N_{\text{cell}}} w_{\mu_1}(\mathbf{q}_1 \kappa_1) w_{\mu_2}(\mathbf{q}_2 \kappa_2) e^{2\pi i(\mathbf{q}_1 + \mathbf{q}_2) \cdot \mathbf{x}(l_2)} \sum_{\bar{l}} D_{\mu_1, \mu_2}(0 \kappa_1, \bar{l} \kappa_2) e^{-2\pi i(\mathbf{x}(\bar{l})) \cdot \mathbf{q}_1} \tag{3.50}$$

$$= \frac{1}{2N_{\text{cell}}} \sum_{\kappa_1, \mu_1} \sum_{\kappa_2, \mu_2} \sum_{\mathbf{q}_1, \mathbf{q}_2} w_{\mu_1}(\mathbf{q}_1 \kappa_1) w_{\mu_2}(\mathbf{q}_2 \kappa_2) \left[ \sum_{l_2} e^{2\pi i(\mathbf{q}_1 + \mathbf{q}_2) \cdot \mathbf{x}(l_2)} \right] D_{\mu_1, \mu_2}(\mathbf{q}_1, \kappa_1, \kappa_2) \tag{3.51}$$

The summation over  $l$  is  $\delta_{\mathbf{q}_1, -\mathbf{q}_2}$  from Eq. (3.26), afterwards we can carry out the summation over  $\mathbf{q}_2$ :

$$U_{\text{harm}} = \frac{1}{2} \sum_{\kappa_1, \mu_1} \sum_{\kappa_2, \mu_2} \sum_{\mathbf{q}_1, \mathbf{q}_2}^{N_{\text{cell}}} w_{\mu_1}(\mathbf{q}_1 \kappa_1) w_{\mu_2}(\mathbf{q}_2 \kappa_2) \delta_{\mathbf{q}_1, -\mathbf{q}_2} D_{\mu_1, \mu_2}(\mathbf{q}_1, \kappa_1, \kappa_2) \tag{3.52}$$

$$= \frac{1}{2} \sum_{\kappa_1, \mu_1} \sum_{\kappa_2, \mu_2} \sum_{\mathbf{q}}^{N_{\text{cell}}} w_{\mu_1}(\mathbf{q}, \kappa_1) w_{\mu_2}(-\mathbf{q}, \kappa_2) D_{\mu_1, \mu_2}(\mathbf{q}, \kappa_1, \kappa_2). \tag{3.53}$$

Using Eq. (3.42), we obtain the potential energy in the form

$$U_{\text{harm}} = \frac{1}{2} \sum_{\kappa_1, \mu_1} \sum_{\kappa_2, \mu_2} \sum_{\mathbf{q}}^{N_{\text{cell}}} w_{\mu_1}(\mathbf{q}, \kappa_1) w_{\mu_2}^*(\mathbf{q}, \kappa_2) D_{\mu_1, \mu_2}(\mathbf{q}, \kappa_1, \kappa_2) \tag{3.54}$$

Compared to the original expression Eq. (3.37), which is the quadratic form of two lattice indices, Eq. (3.54) is the  $N_{\text{cell}}$  independent  $\mathbf{q}$  form characterized by a  $3N \times 3N$  matrix  $D_{\mu_1, \mu_2}(\mathbf{q}, \kappa_1, \kappa_2)$ .

Let us go back to Newton's equation of motion Eq. (3.40), which represents a system of simultaneous linear differential equations. We suppose that the solution is given by

$$w_{\mu}(\mathbf{q}, \kappa) e^{2\pi i \mathbf{q} \cdot \mathbf{x}(l)} e^{-i\omega t} \tag{3.55}$$

Upon substituting Eq. (3.55) in Eq. (3.40), we get

$$(-i\omega)^2 w_{\mu}(\mathbf{q}, \kappa) e^{2\pi i \mathbf{q} \cdot \mathbf{x}(l)} e^{-i\omega t} = - \sum_{l_2, \kappa_2, \mu_2} D_{\mu, \mu_2}(l \kappa, l_2 \kappa_2) w_{\mu_2}(\mathbf{q}, \kappa_2) e^{2\pi i \mathbf{q} \cdot \mathbf{x}(l_2)} e^{-i\omega t}. \tag{3.56}$$

Multiplying  $e^{-2\pi i \mathbf{q} \cdot \mathbf{x}(l)}$  both side and using Eq. (3.45) yields

$$\omega^2 w_{\mu}(\mathbf{q}, \kappa) e^{-i\omega t} = \sum_{l_2, \kappa_2, \mu_2} w_{\mu_2}(\mathbf{q}, \kappa_2) D_{\mu, \mu_2}(0 \kappa, l_2 - l \kappa_2) e^{2\pi i \mathbf{q} \cdot (\mathbf{x}(l_2) - \mathbf{x}(l))} e^{-i\omega t}. \tag{3.57}$$

Similar to Eq. (3.50), we can replace the summation index from  $l_2$  to  $l_2 - l$ . Using the relation Eq. (3.46), we can take the summation over  $l_2$ ,

$$\omega^2 w_\mu(\mathbf{q}, \kappa) e^{-i\omega t} = \sum_{\kappa_2, \mu_2} D_{\mu, \mu_2}(\mathbf{q}, \kappa, \kappa_2) w_{\mu_2}(\mathbf{q}, \kappa_2) e^{-i\omega t} \quad (3.58)$$

Dividing both side by  $e^{-i\omega t}$  yields

$$\omega^2 w_\mu(\mathbf{q}, \kappa) = \sum_{\kappa_2, \mu_2} D_{\mu, \mu_2}(\mathbf{q}, \kappa, \kappa_2) w_{\mu_2}(\mathbf{q}, \kappa_2) \quad (3.59)$$

This is nothing but the eigenvalue relation for  $N_{\text{cell}}$  dynamical matrix  $D_{\mu, \mu_2}(\mathbf{q}, \kappa, \kappa_2)$  ( $\mathbf{q} = 0, 1, \dots, N_{\text{cell}} - 1$ ), which is a  $3N \times 3N$  Hermitian matrix. For each  $\mathbf{q}$ , there exist  $3N$  sets of eigenvectors  $e_{\kappa\mu}(\mathbf{q}, j)$  and eigenvalues  $\omega_{\mathbf{q},j}^2$  for  $j = 1, 2, \dots, 3N$ ,

$$\sum_{\kappa_2, \mu_2} D_{\mu, \mu_2}(\mathbf{q}, \kappa, \kappa_2) e_{\kappa_2 \mu_2}(\mathbf{q}j) = \omega_{\mathbf{q},j}^2 e_{\kappa\mu}(\mathbf{q}j). \quad (3.60)$$

We impose the direct and inverse orthonormal relations on eigenvectors as

$$\sum_{\kappa\mu} e_{\kappa\mu}^*(\mathbf{q}j_1) e_{\kappa\mu}(\mathbf{q}j_2) = \delta_{j_1 j_2} \quad (3.61)$$

$$\sum_j e_{\kappa_1 \mu_1}^*(\mathbf{q}j) e_{\kappa_2 \mu_2}(\mathbf{q}j) = \delta_{\mu_1 \mu_2} \delta_{\kappa_1 \kappa_2}. \quad (3.62)$$

Eigenvalues can be obtained from the eigenvalue equations

$$|\omega_{\mathbf{q},j}^2 \delta_{\mu_1 \mu_2} \delta_{\kappa_1, \kappa_2} - D_{\mu_1, \mu_2}(\mathbf{q}, \kappa_1, \kappa_2)| = 0. \quad (3.63)$$

eigenvalues are all real because  $D_{\mu, \mu_2}(\mathbf{q}, \kappa, \kappa_2)$  is Hermitian. Therefore, vibration frequencies  $\omega_{\mathbf{q},j}$  must be either real or purely imaginary. It is known that  $\omega_{\mathbf{q},j}$  are all real if the lattice is stable. As  $\omega_{\mathbf{q},j}^2$  are real, taking the complex conjugate of Eq. (3.46) yields

$$D_{\mu_1, \mu_2}^*(\mathbf{q}, \kappa_1, \kappa_2) = D_{\mu_1, \mu_2}(-\mathbf{q}, \kappa_1, \kappa_2), \quad (3.64)$$

with which we have upon taking the complex conjugates of Eq. (3.60) and (3.63)

$$\sum_{\kappa_2, \mu_2} D_{\mu_1, \mu_2}(-\mathbf{q}, \kappa_1, \kappa_2) e_{\kappa_2 \mu_2}^*(\mathbf{q}j) = \omega_{\mathbf{q},j}^2 e_{\kappa_1 \mu_1}^*(\mathbf{q}j) \quad (3.65)$$

$$|\omega_{\mathbf{q},j}^2 \delta_{\mu_1 \mu_2} \delta_{\kappa_1, \kappa_2} - D_{\mu_1, \mu_2}(-\mathbf{q}, \kappa_1, \kappa_2)| = 0. \quad (3.66)$$

Compared with the eigenvalue relations for a mode  $(-\mathbf{q}, j)$ , we find that eigenvalues and eigenstates satisfy the following relations:

$$\omega_{\mathbf{q}j} = \omega_{-\mathbf{q}j} \quad (3.67)$$

$$e_{\kappa\mu}^*(\mathbf{q}j) = e_{\kappa\mu}(-\mathbf{q}j) \quad (3.68)$$

### 3.4 Normal Coordinates

The complex normal coordinates  $Q(\mathbf{q}, j)$  are introduced by the unitary transformation of  $w_\mu(\mathbf{q}, \kappa)$

$$w_\mu(\mathbf{q}, \kappa) = \sum_j e_{\kappa\mu}(\mathbf{q}j) Q(\mathbf{q}, j), \quad (3.69)$$

and the inverse transformation is

$$Q(\mathbf{q}j) = \sum_{\kappa\mu} e_{\kappa\mu}^*(\mathbf{q}j) w_\mu(\mathbf{q}, \kappa). \quad (3.70)$$

The complex conjugate of  $Q(\mathbf{q}, j)$  satisfies

$$Q^*(\mathbf{q}j) = Q(-\mathbf{q}, j), \quad (3.71)$$

which follows from Eq. (3.70) and Eq. (3.42)

$$Q^*(\mathbf{q}j) = \sum_{\kappa\mu} e_{\mu}(\kappa, \mathbf{q}j) w_{\mu}^*(\kappa, \mathbf{q}) = \sum_{\kappa\mu} e_{\kappa\mu}^*(-\mathbf{q}j) w_{\mu}(\kappa, -\mathbf{q}) = Q(-\mathbf{q}, j). \quad (3.72)$$

Substituting Eq. (3.69) into Eq. (3.41), we can express reduced-coordinates in terms of  $Q(\mathbf{q}j)$

$$w_{\mu}(l\kappa) = \frac{1}{\sqrt{N_{\text{cell}}}} \sum_{\mathbf{q}} \sum_j^{N_{\text{cell}}} Q(\mathbf{q}j) e_{\kappa\mu}(\mathbf{q}j) e^{2\pi i \mathbf{q} \cdot \mathbf{x}(l)}. \quad (3.73)$$

Therefore, we can interpret that the complex normal coordinates describe the amplitudes of lattice waves with the wave number  $\mathbf{q}$  represented in the complex form. The harmonic potential can be reduced using  $Q(\mathbf{q}, j)$  as follows:

$$\begin{aligned} U_{\text{harm}} &= \frac{1}{2} \sum_{\kappa_1\mu_1} \sum_{\kappa_2\mu_2} \sum_{\mathbf{q}}^{N_{\text{cell}}} w_{\mu_1}(\mathbf{q}, \kappa_1) w_{\mu_2}^*(\mathbf{q}, \kappa_2) D_{\mu_1\mu_2}(\mathbf{q}, \kappa_1\kappa_2) \\ &= \frac{1}{2} \sum_{\kappa_2\mu_2} \sum_{\mathbf{q}}^{N_{\text{cell}}} \sum_{j_1} \sum_{j_2} Q(\mathbf{q}, j_1) Q(\mathbf{q}, j_2) e_{\kappa_2\mu_2}^*(\mathbf{q}, j_2) \sum_{\kappa_1\mu_1} D_{\mu_1\mu_2}(\mathbf{q}, \kappa_1\kappa_2) e_{\kappa_1\mu_1}(\mathbf{q}, j_1) \\ &= \frac{1}{2} \sum_{\kappa_2\mu_2} \sum_{\mathbf{q}}^{N_{\text{cell}}} \sum_{j_1} \sum_{j_2} Q(\mathbf{q}, j_1) Q(\mathbf{q}, j_2) e_{\kappa_2\mu_2}^*(\mathbf{q}, j_2) \omega_{\mathbf{q}j_1}^2 e_{\kappa_2\mu_2}(\mathbf{q}, j_1), \end{aligned} \quad (3.74)$$

where we have made use of Eq. (3.60). Using Eq. (3.61), the summation over  $\kappa_2$  and  $\mu_2$  can be simplified to  $\delta_{j_1j_2}$ , then we can perform the summation over  $j_2$

$$\begin{aligned} U_{\text{harm}} &= \frac{1}{2} \sum_{\mathbf{q}}^{N_{\text{cell}}} \sum_{j_1} \sum_{j_2} Q(\mathbf{q}, j_1) Q(\mathbf{q}, j_2) \omega_{\mathbf{q}j_1}^2 \delta_{j_1j_2} \\ &= \frac{1}{2} \sum_{\mathbf{q}}^{N_{\text{cell}}} \sum_j \omega_{\mathbf{q}j}^2 Q^*(\mathbf{q}j) Q(\mathbf{q}j). \end{aligned} \quad (3.75)$$

Similarly, we substitute Eq. (3.73) into the kinetic energy term Eq. (3.38)

$$\begin{aligned} T &= \frac{1}{2} \sum_{l, \kappa, \mu} w_{\mu}^*(l\kappa) w_{\mu}(l\kappa) \\ &= \frac{1}{2} \sum_{\mathbf{q}_1}^{N_{\text{cell}}} \sum_{j_1} \sum_{\mathbf{q}_2}^{N_{\text{cell}}} \sum_{j_2} Q^*(\mathbf{q}_1j_1) Q(\mathbf{q}_2j_2) \sum_{\kappa, \mu} e_{\kappa\mu}^*(\mathbf{q}_1j_1) e_{\kappa\mu}(\mathbf{q}_2j_2) \sum_l \frac{1}{N_{\text{cell}}} e^{-2\pi i \mathbf{q}_1 \cdot \mathbf{x}(l)} e^{2\pi i \mathbf{q}_2 \cdot \mathbf{x}(l)} \end{aligned} \quad (3.76)$$

$$= \frac{1}{2} \sum_{\mathbf{q}}^{N_{\text{cell}}} \sum_j \dot{Q}^*(\mathbf{q}j) \dot{Q}(\mathbf{q}j), \quad (3.77)$$

where the summation over  $l$  has been curtailed to  $\delta_{\mathbf{q}_1, \mathbf{q}_2}$  from Eq. (3.26), then the summation over  $\kappa$  and  $\mu$  has turned to  $\delta_{j_1, j_2}$ . Finally, the Hamiltonian reads

$$H = T + U_{\text{harm}} = \frac{1}{2} \sum_{\mathbf{q}}^{N_{\text{cell}}} \sum_j \left[ \dot{Q}^*(\mathbf{q}j) \dot{Q}(\mathbf{q}j) + \omega_{\mathbf{q}j}^2 Q^*(\mathbf{q}j) Q(\mathbf{q}j) \right]. \quad (3.78)$$

For later discussion, we rewrite the Hamiltonian in terms of momentum. The complex normal coordinates are expressed in terms of the atomic displacements from Eq. (3.36), (3.44) and (3.70)

$$Q(\mathbf{q}j) = \sum_{\kappa\mu} e_{\kappa\mu}^*(\mathbf{q}j) \left[ \frac{1}{\sqrt{N_{\text{cell}}}} \sum_l \sqrt{m_{\kappa}} u_{\mu}(l, \kappa) e^{-2\pi i \mathbf{q} \cdot \mathbf{x}(l)} \right] \quad (3.79)$$

Noting that the momentum of the atom ( $l\kappa$ ) is defined as

$$p_{\mu}(l\kappa) = m_{\kappa} \dot{u}_{\mu}(l\kappa), \quad (3.80)$$

we introduce the complex normal momentum  $P(\mathbf{q}j)$  corresponding to the complex normal coordinate (see Eq. (3.71))

$$P(\mathbf{q}j) = \dot{Q}^*(\mathbf{q}j) = \dot{Q}(-\mathbf{q}j), \quad (3.81)$$

which is written in terms of atomic momentum using Eq. (3.79)

$$P(\mathbf{q}j) = \sum_{\kappa\mu} e_{\kappa\mu}(\mathbf{q}j) \left[ \frac{1}{\sqrt{N_{\text{cell}}}} \sum_l \frac{p_\mu(l, \kappa)}{\sqrt{m_\kappa}} e^{+2\pi i \mathbf{q} \cdot \mathbf{x}(l)} \right]. \quad (3.82)$$

The Hamiltonian is written as

$$H = \frac{1}{2} \sum_{\mathbf{q}} \sum_j^{N_{\text{cell}}} [P^*(\mathbf{q}j)P(\mathbf{q}j) + \omega_{\mathbf{q}j}^2 Q^*(\mathbf{q}j)Q(\mathbf{q}j)] \quad (3.83)$$

$$= \frac{1}{2} \sum_{\mathbf{q}} \sum_j^{N_{\text{cell}}} [P(-\mathbf{q}j)P(\mathbf{q}j) + \omega_{\mathbf{q}j}^2 Q(-\mathbf{q}j)Q(\mathbf{q}j)]. \quad (3.84)$$

### 3.5 Expansion of Physical Quantities by Normal Coordinate

In the previous section, we discussed the energy of the harmonic approximation by using the Taylor expansion from the equilibrium position of the potential energy. In this section, we consider general expansion rules for both the potential energy and the dipole moment. They are representative physical quantities in the sense that they are scalar and vector, respectively. We start with the Taylor expansion for a scalar  $U$  with the first-order term remaining for general discussion.

$$U = U_0 + U_1 + U_2 + U_3 + \cdots \quad (3.85)$$

$$U_n = \frac{1}{n!} \sum_{(l_1, \kappa_1, \mu_1)}^{N_{\text{cell}}} \cdots \sum_{(l_n, \kappa_n, \mu_n)}^{N_{\text{cell}}} \Phi_{\mu_1 \cdots \mu_n}(l_1 \kappa_1, \cdots, l_n \kappa_n) \times u_{\mu_1}(l_1 \kappa_1) \cdots u_{\mu_n}(l_n \kappa_n), \quad (3.86)$$

Exactly the same equation holds for the dipole moment  $\mathbf{M}$ , except for the expansion coefficients:

$$\mathbf{M} = \mathbf{M}_0 + \mathbf{M}_1 + \mathbf{M}_2 + \mathbf{M}_3 + \cdots, \quad (3.87)$$

where the  $\alpha$  component of  $\mathbf{M}_n$  is

$$M_{n,\alpha} = \frac{1}{n!} \sum_{l_1 \kappa_1 \mu_1}^{N_{\text{cell}}} \cdots \sum_{l_n \kappa_n \mu_n}^{N_{\text{cell}}} M_{\alpha, \mu_1 \cdots \mu_n}(l_1 \kappa_1, l_2 \kappa_2, \cdots, l_n \kappa_n) \times u_{\mu_1}(l_1 \kappa_1) u_{\mu_2}(l_2 \kappa_2) \cdots u_{\mu_n}(l_n \kappa_n). \quad (3.88)$$

Here,  $\alpha$  is the index of Cartesian coordinates. The summation with the index  $N_{\text{cell}}$  means that the summation is restricted to the  $N_{\text{cell}}$  cells in the supercell, the same as the previous section. The coefficient  $M_{\alpha, \mu_1 \cdots \mu_n}(l_1 \kappa_1, l_2 \kappa_2, \cdots, l_n \kappa_n)$  is the  $n$ th-order derivative of  $\mathbf{M}$  with respect to atomic coordinates as

$$M_{\alpha, \mu_1 \cdots \mu_n}(l_1 \kappa_1, \cdots, l_n \kappa_n) = \frac{\partial M_\alpha}{\partial u_{\mu_1}(l_1 \kappa_1) \cdots \partial u_{\mu_n}(l_n \kappa_n)}. \quad (3.89)$$

From the periodic boundary condition, the value of the quantity does not change when the same number is added to the indices of all cells. Thus, the first-order quantity is independent of  $l$ , the second-order quantity depends only on the difference of the cell indices  $l - l'$ , and the third-order quantity depends only on  $l - l'$  and  $l - l''$ . We can exhibit this fact explicitly by using the following alternative notation for the expansion coefficients:

$$M_{\alpha, \beta}(l\kappa) = M_{\alpha, \beta}(\kappa) \quad (3.90)$$

$$M_{\alpha, \beta\gamma}(l\kappa, l'\kappa') = M_{\alpha, \beta\gamma}(l - l', \kappa\kappa') \quad (3.91)$$

The first-order coefficients are called the Born effective charge tensor and are usually denoted by  $Z^*$

$$Z_{\kappa, \alpha\beta}^* = M_{\alpha, \beta}(\kappa), \quad (3.92)$$

which can be calculated by DFPT. Due to the translational symmetry of the system, the physical quantity is invariant even if all atomic displacements  $\mathbf{u}$  are equal to an arbitrary vector  $\boldsymbol{\varepsilon}$ . Up to the first order in  $\boldsymbol{\varepsilon}$ , we have

$$\sum_{\beta, \kappa} M_{\alpha, \beta}(\kappa) \varepsilon_{\beta} = 0. \quad (3.93)$$

Since this must hold for all values of  $\boldsymbol{\varepsilon}$ , we obtain

$$\sum_{\kappa} M_{\alpha, \beta}(\kappa) = 0, \quad (3.94)$$

which is called the acoustic sum rule [9].

To see how Eq. (3.88) can be rewritten in terms of complex normal coordinates, let us first examine the  $n = 1$  expansion for a scalar function  $U$ . The nuclear displacements are expressed in terms of the complex normal coordinates from Eq. (3.36) and (3.73)

$$u_{\mu}(l\kappa) = \frac{1}{\sqrt{m_{\kappa}}} w_{\mu}(l\kappa) = \frac{1}{\sqrt{N_{\text{cell}} m_{\kappa}}} \sum_{\mathbf{q}j} Q(\mathbf{q}j) e_{\kappa\mu}(\mathbf{q}j) e^{2\pi i \mathbf{q} \cdot \mathbf{x}(l)}. \quad (3.95)$$

Substituting Eq. (3.95) into Eq. (3.85) of  $n = 1$  yields

$$\sum_{l\kappa\mu} \Phi_{\mu}(l\kappa) u_{\mu}(l\kappa) = \sum_{l\kappa\mu} \Phi_{\mu}(l\kappa) \frac{1}{\sqrt{N_{\text{cell}} m_{\kappa}}} \sum_{\mathbf{q}j} Q(\mathbf{q}j) e_{\kappa\mu}(\mathbf{q}j) e^{2\pi i \mathbf{q} \cdot \mathbf{x}(l)} \quad (3.96)$$

$$= \sum_l \sum_{\mathbf{q}j} Q(\mathbf{q}j) \frac{1}{\sqrt{N_{\text{cell}}}} e^{2\pi i \mathbf{q} \cdot \mathbf{x}(l)} \left[ \sum_{\kappa\mu} \frac{1}{\sqrt{m_{\kappa}}} \Phi_{\mu}(l\kappa) e_{\kappa\mu}(\mathbf{q}j) \right] \quad (3.97)$$

$\Phi_{\mu}(l\kappa)$  does not depend on  $l$  and we can define the wave-vector representation of  $\Phi$  as

$$\Phi_{\mu}(\mathbf{q}j) = \sum_{\kappa\mu} \frac{1}{\sqrt{m_{\kappa}}} \Phi_{\mu}(\kappa) e_{\mu}(\kappa, \mathbf{q}j). \quad (3.98)$$

Applying this expression into Eq. (3.97) outputs

$$\sum_{l\kappa\mu} \Phi_{\mu}(l\kappa) u_{\mu}(l\kappa) = \sum_{\mathbf{q}j} \sum_l Q(\mathbf{q}j) \frac{1}{\sqrt{N_{\text{cell}}}} e^{2\pi i \mathbf{q} \cdot \mathbf{x}(l)} \Phi_{\mu}(\mathbf{q}j). \quad (3.99)$$

From the definition of  $\Delta$  function Eq. (3.26), the summation over  $l$  give us  $\Delta(\mathbf{q})$  as

$$U_1 = \sum_{\mathbf{q}j} Q(\mathbf{q}j) \sqrt{N_{\text{cell}}} \Delta(\mathbf{q}) \Phi_{\mu}(\mathbf{q}j). \quad (3.100)$$

Since the delta function gives unity only at  $\mathbf{q} = 0$  and 0 otherwise, we can also perform summation with respect to  $\mathbf{q}$ , which means that the current expansion only needs to be summed at the  $\Gamma$  point of  $\mathbf{q} = \mathbf{0}$

$$U_1 = \sum_j Q(\mathbf{0}j) \sqrt{N_{\text{cell}}} \Phi_{\mu}(\mathbf{0}j). \quad (3.101)$$

Although the expansion of energy  $U$  actually yields  $U_1 = 0$  from the equilibrium condition, the expansion of Eq. (3.101) is also valid for  $\mathbf{M}$  because it only uses the periodicity of the crystal. The above transformation implies that by considering the expansion for the complex normal coordinate, the  $\Delta$  function appears, which restricts the index to be summed. This is the so-called selection rule.

To see if the same rule holds for higher-order expansions, we examine  $n = 3$  expansions as an example:

$$U_3 = \frac{1}{3!} \sum_{l_1 \kappa_1 \mu_1} \sum_{l_2 \kappa_2 \mu_2} \sum_{l_3 \kappa_3 \mu_3} \Phi_{\mu_1 \mu_2 \mu_3}(l_1 \kappa_1, l_2 \kappa_2, l_3 \kappa_3) u_{\mu_1}(l_1 \kappa_1) u_{\mu_2}(l_2 \kappa_2) u_{\mu_3}(l_3 \kappa_3). \quad (3.102)$$

We again rewrite the expansion in terms of complex normal coordinates using Eq. (3.95)

$$U_3 = \frac{1}{3! N_{\text{cell}}^{3/2}} \sum_{(\mathbf{q}_1 j_1)} \sum_{(\mathbf{q}_2 j_2)} \sum_{(\mathbf{q}_3 j_3)} Q(\mathbf{q}_1 j_1) Q(\mathbf{q}_2 j_2) Q(\mathbf{q}_3 j_3) \quad (3.103)$$

$$\times \sum_{l_1 \kappa_1 \mu_1} \sum_{l_2 \kappa_2 \mu_2} \sum_{l_3 \kappa_3 \mu_3} \Phi_{\mu_1 \mu_2 \mu_3}(l_1 \kappa_1, l_2 \kappa_2, l_3 \kappa_3) \frac{1}{\sqrt{m_{\kappa_1} m_{\kappa_2} m_{\kappa_3}}} e_{\kappa_1 \mu_1}(\mathbf{q}_1 j_1) e_{\kappa_2 \mu_2}(\mathbf{q}_2 j_2) e_{\kappa_3 \mu_3}(\mathbf{q}_3 j_3) \quad (3.104)$$

$$\times \exp(2\pi i (\mathbf{q}_1 \cdot \mathbf{x}(l_1) + \mathbf{q}_2 \cdot \mathbf{x}(l_2) + \mathbf{q}_3 \cdot \mathbf{x}(l_3))). \quad (3.105)$$

We can subtract the same index  $l$  from all the cell indices of  $\Phi$  from the periodic boundary conditions. Noting the obvious relation

$$x(l_2) = x(l_2 - l_1) + x(l_1) \quad (3.106)$$

$$x(l_3) = x(l_3 - l_1) + x(l_1), \quad (3.107)$$

we introduce  $\bar{l}_3 = l_3 - l_1$  and  $\bar{l}_2 = l_2 - l_1$  as new summation indices.

$$\begin{aligned} U_3 = & \frac{1}{3!N_{\text{cell}}^{3/2}} \sum_{(\mathbf{q}_1 j_1)} \sum_{(\mathbf{q}_2 j_2)} \sum_{(\mathbf{q}_3 j_3)} Q(\mathbf{q}_1 j_1) Q(\mathbf{q}_2 j_2) Q(\mathbf{q}_3 j_3) \sum_l \exp(2\pi i(\mathbf{q}_1 + \mathbf{q}_2 + \mathbf{q}_3) \cdot \mathbf{x}(l)) \\ & \times \left[ \sum_{\kappa_1 \mu_1} \sum_{\bar{l}_2 \kappa_2 \mu_2} \sum_{\bar{l}_3 \kappa_3 \mu_3} \Phi_{\mu_1 \mu_2 \mu_3}(0\kappa_1, \bar{l}_2 \kappa_2, \bar{l}_3 \kappa_3) \frac{1}{\sqrt{m_{\kappa_1} m_{\kappa_2} m_{\kappa_3}}} e_{\kappa_1 \mu_1}(\mathbf{q}_1 j_1) e_{\kappa_2 \mu_2}(\mathbf{q}_2 j_2) e_{\kappa_3 \mu_3}(\mathbf{q}_3 j_3) \right. \\ & \left. \times \exp(2\pi i(\mathbf{q}_2 \cdot \mathbf{x}(\bar{l}_2) + \mathbf{q}_3 \cdot \mathbf{x}(\bar{l}_3))) \right] \end{aligned} \quad (3.108)$$

The expression in the curly brackets is independent of  $l_1$ , and we can define it as the wave number representation of  $\Phi$

$$\begin{aligned} \Phi(\mathbf{q}_1 j_1, \mathbf{q}_2 j_2, \mathbf{q}_3 j_3) = & \sum_{\kappa_1 \mu_1} \sum_{l_2 \kappa_2 \mu_2} \sum_{l_3 \kappa_3 \mu_3} \Phi_{\mu_1 \mu_2 \mu_3}(0\kappa_1, l_2 \kappa_2, l_3 \kappa_3) \frac{1}{\sqrt{m_{\kappa_1} m_{\kappa_2} m_{\kappa_3}}} e_{\kappa_1 \mu_1}(\mathbf{q}_1 j_1) e_{\kappa_2 \mu_2}(\mathbf{q}_2 j_2) e_{\kappa_3 \mu_3}(\mathbf{q}_3 j_3) \\ & \times \exp(2\pi i(\mathbf{q}_2 \cdot \mathbf{x}(l_2) + \mathbf{q}_3 \cdot \mathbf{x}(l_3))). \end{aligned} \quad (3.109)$$

We can express the result of the summation over  $l$  in terms of the  $\Delta$  function

$$U_3 = \frac{1}{3!N_{\text{cell}}^{1/2}} \sum_{(\mathbf{q}_1 j_1)} \sum_{(\mathbf{q}_2 j_2)} \sum_{(\mathbf{q}_3 j_3)} Q(\mathbf{q}_1 j_1) Q(\mathbf{q}_2 j_2) Q(\mathbf{q}_3 j_3) \Delta(\mathbf{q}_1 + \mathbf{q}_2 + \mathbf{q}_3) \Phi(\mathbf{q}_1 j_1, \mathbf{q}_2 j_2, \mathbf{q}_3 j_3), \quad (3.110)$$

noting that the denominator  $N_{\text{cell}}^{3/2}$  has become  $N_{\text{cell}}^{1/2}$ .

We now discuss the symmetry of the newly defined  $\Phi(\mathbf{q}_1 j_1, \mathbf{q}_2 j_2, \mathbf{q}_3 j_3)$  in Eq. (3.109). Let us first consider the permutation symmetry. We recall that the IFCs have the permutation symmetry. For example, if we exchange the second and third variables,

$$\Phi_{\mu_1 \mu_2 \mu_3}(0\kappa_1, l_2 \kappa_2, l_3 \kappa_3) = \Phi_{\mu_1 \mu_3 \mu_2}(0\kappa_1, l_3 \kappa_3, l_2 \kappa_2). \quad (3.111)$$

It is then obvious that  $\Phi(\mathbf{q}_1 j_1, \mathbf{q}_2 j_2, \mathbf{q}_3 j_3)$  is invariant under the second and third indices:

$$\Phi(\mathbf{q}_1 j_1, \mathbf{q}_2 j_2, \mathbf{q}_3 j_3) = \Phi(\mathbf{q}_1 j_1, \mathbf{q}_3 j_3, \mathbf{q}_2 j_2). \quad (3.112)$$

To show that  $\Phi(\mathbf{q}_1 j_1, \mathbf{q}_2 j_2, \mathbf{q}_3 j_3)$  is also symmetric between the first and second (or third) indices, we have only to consider the case

$$\mathbf{q}_1 + \mathbf{q}_2 + \mathbf{q}_3 = \mathbf{G} \quad \mathbf{G} \in \text{reciprocal lattice vector} \quad (3.113)$$

for which  $\Delta(\mathbf{q}_1 + \mathbf{q}_2 + \mathbf{q}_3) \neq 0$ . We exchange the first and second summation indices in Eq. (3.109)

$$\begin{aligned} \Phi(\mathbf{q}_1 j_1, \mathbf{q}_2 j_2, \mathbf{q}_3 j_3) = & \sum_{\kappa_1 \mu_1} \sum_{l_2 \kappa_2 \mu_2} \sum_{l_3 \kappa_3 \mu_3} \Phi_{\mu_2 \mu_1 \mu_3}(l_2 \kappa_2, 0\kappa_1, l_3 \kappa_3) \frac{1}{\sqrt{m_{\kappa_1} m_{\kappa_2} m_{\kappa_3}}} e_{\kappa_1 \mu_1}(\mathbf{q}_1 j_1) e_{\kappa_2 \mu_2}(\mathbf{q}_2 j_2) e_{\kappa_3 \mu_3}(\mathbf{q}_3 j_3) \\ & \times \exp(2\pi i(\mathbf{q}_2 \cdot \mathbf{x}(l_2) + \mathbf{q}_3 \cdot \mathbf{x}(l_3))) \end{aligned} \quad (3.114)$$

In addition, we re-label the atoms  $\kappa$  and the Cartesian indices  $\mu$  for the first and second variables keeping  $l$  unchanged,

$$\begin{aligned} \Phi(\mathbf{q}_1 j_1, \mathbf{q}_2 j_2, \mathbf{q}_3 j_3) = & \sum_{\kappa_1 \mu_1} \sum_{l_2 \kappa_2 \mu_2} \sum_{l_3 \kappa_3 \mu_3} \Phi_{\mu_1 \mu_2 \mu_3}(l_2 \kappa_1, 0\kappa_2, l_3 \kappa_3) \frac{1}{\sqrt{m_{\kappa_1} m_{\kappa_2} m_{\kappa_3}}} e_{\kappa_2 \mu_2}(\mathbf{q}_1 j_1) e_{\kappa_1 \mu_1}(\mathbf{q}_2, j_2) e_{\kappa_3 \mu_3}(\mathbf{q}_3 j_3) \\ & \times \exp(2\pi i(\mathbf{q}_2 \cdot \mathbf{x}(l_2) + \mathbf{q}_3 \cdot \mathbf{x}(l_3))) \end{aligned} \quad (3.115)$$

Rewriting the exponential function using the conditional Eq. (3.113), we find

$$\begin{aligned} \Phi(\mathbf{q}_1 j_1, \mathbf{q}_2 j_2, \mathbf{q}_3 j_3) &= \sum_{\kappa_1 \mu_1} \sum_{l_2 \kappa_2 \mu_2} \sum_{l_3 \kappa_3 \mu_3} \Phi_{\mu_1 \mu_2 \mu_3}(l_2 \kappa_1, 0 \kappa_2, l_3 \kappa_3) \frac{1}{\sqrt{m_{\kappa_1} m_{\kappa_2} m_{\kappa_3}}} e_{\kappa_2 \mu_2}(\mathbf{q}_1 j_1) e_{\kappa_1 \mu_1}(\mathbf{q}_2, j_2) e_{\kappa_3 \mu_3}(\mathbf{q}_3 j_3) \\ &\times \exp(2\pi i((\mathbf{G} - \mathbf{q}_1 - \mathbf{q}_3) \cdot \mathbf{x}(l_2) + \mathbf{q}_3 \cdot \mathbf{x}(l_3))) \end{aligned} \quad (3.116)$$

$$\begin{aligned} &= \sum_{\kappa_1 \mu_1} \sum_{l_2 \kappa_2 \mu_2} \sum_{l_3 \kappa_3 \mu_3} \Phi_{\mu_1 \mu_2 \mu_3}(l_2 \kappa_1, 0 \kappa_2, l_3 \kappa_3) \frac{1}{\sqrt{m_{\kappa_1} m_{\kappa_2} m_{\kappa_3}}} e_{\kappa_2 \mu_2}(\mathbf{q}_1 j_1) e_{\kappa_1 \mu_1}(\mathbf{q}_2, j_2) e_{\kappa_3 \mu_3}(\mathbf{q}_3 j_3) \\ &\times \exp(2\pi i((-\mathbf{q}_1 - \mathbf{q}_3) \cdot \mathbf{x}(l_2) + \mathbf{q}_3 \cdot \mathbf{x}(l_3))) \end{aligned} \quad (3.117)$$

where we have used  $e^{2\pi i \mathbf{G} \cdot \mathbf{x}} = 1$  for any lattice vector  $\mathbf{x}$  in the second line. Subtracting  $l_2$  from the cell indices in the  $\Phi$  and introducing  $-l_2$  and  $l_3 - l_2$  as summation indices and afterwards writing them simply as  $\tilde{l}_2$  and  $\tilde{l}_3$ , we have

$$\begin{aligned} \Phi(\mathbf{q}_1 j_1, \mathbf{q}_2 j_2, \mathbf{q}_3 j_3) &= \sum_{\kappa_1 \mu_1} \sum_{l_2 \kappa_2 \mu_2} \sum_{l_3 \kappa_3 \mu_3} \Phi_{\mu_1 \mu_2 \mu_3}(\kappa_1, -l_2 \kappa_2, l_3 - l_2 \kappa_3) \frac{1}{\sqrt{m_{\kappa_1} m_{\kappa_2} m_{\kappa_3}}} e_{\kappa_2 \mu_2}(\mathbf{q}_1 j_1) e_{\kappa_1 \mu_1}(\mathbf{q}_2, j_2) e_{\kappa_3 \mu_3}(\mathbf{q}_3 j_3) \\ &\times \exp(2\pi i(-\mathbf{q}_1 \cdot \mathbf{x}(l_2) + \mathbf{q}_3 \cdot (\mathbf{x}(l_3) - \mathbf{x}(l_2)))) \end{aligned} \quad (3.118)$$

$$\begin{aligned} &= \sum_{\kappa_1 \mu_1} \sum_{\tilde{l}_2 \kappa_2 \mu_2} \sum_{\tilde{l}_3 \kappa_3 \mu_3} \Phi_{\mu_1 \mu_2 \mu_3}(0 \kappa_1, \tilde{l}_2 \kappa_2, \tilde{l}_3 \kappa_3) \frac{1}{\sqrt{m_{\kappa_1} m_{\kappa_2} m_{\kappa_3}}} e_{\kappa_2 \mu_2}(\mathbf{q}_1 j_1) e_{\kappa_1 \mu_1}(\mathbf{q}_2, j_2) e_{\kappa_3 \mu_3}(\mathbf{q}_3 j_3) \\ &\times \exp(2\pi i(\mathbf{q}_1 \cdot \mathbf{x}(\tilde{l}_2) + \mathbf{q}_3 \cdot \mathbf{x}(\tilde{l}_3))) \end{aligned} \quad (3.119)$$

Comparing with Eq. (3.109) we see that the right-hand side is nothing but  $\Phi(\mathbf{q}_2 j_2, \mathbf{q}_1 j_1, \mathbf{q}_3 j_3)$ . It means we have shown the permutation symmetry of the first and second variables.

$$\Phi(\mathbf{q}_1 j_1, \mathbf{q}_2 j_2, \mathbf{q}_3 j_3) = \Phi(\mathbf{q}_2 j_2, \mathbf{q}_1 j_1, \mathbf{q}_3 j_3) \quad (3.120)$$

From Eq. (3.112) and (3.120) we conclude that  $\Phi(\mathbf{q}_1 j_1, \mathbf{q}_2 j_2, \mathbf{q}_3 j_3)$  have permutation symmetry of any two indices.

The second symmetry is about a complex conjugate of  $\Phi$ . From the relation of eigenvectors Eq. (3.68), we see straightforwardly by taking the complex conjugate of Eq. (3.109)

$$\Phi^*(\mathbf{q}_1 j_1, \mathbf{q}_2 j_2, \mathbf{q}_3 j_3) = \Phi(-\mathbf{q}_1 j_1, -\mathbf{q}_2 j_2, -\mathbf{q}_3 j_3). \quad (3.121)$$

The above discussion applies equally well to general  $n$ th-order expansions. The  $n$ th-order terms in the expansion are

$$U_n = \sum_{(\mathbf{q}_1 j_1)} \cdots \sum_{(\mathbf{q}_n j_n)} \frac{1}{n!} \frac{1}{N_{\text{cell}}^{n/2-1}} \Delta(\mathbf{q}_1 + \mathbf{q}_2 + \cdots + \mathbf{q}_n) \Phi(\mathbf{q}_1 j_1, \dots, \mathbf{q}_n j_n) Q(\mathbf{q}_1 j_1) \cdots Q(\mathbf{q}_n j_n), \quad (3.122)$$

where we define the wave number expression of  $\Phi$  as

$$\begin{aligned} \Phi(\mathbf{q}_1 j_1, \dots, \mathbf{q}_n j_n) &= \sum_{\kappa_1 \mu_1} \cdots \sum_{l_n \kappa_n \mu_n} \Phi_{\mu_1 \dots \mu_n}(0 \kappa_1, l_2 \kappa_2, \dots, l_n \kappa_n) \frac{1}{\sqrt{m_{\kappa_1} \cdots m_{\kappa_n}}} e_{\mu_1}(k_1 j_1, \kappa_1) \cdots e_{\mu_n}(k_n j_n, \kappa_n) \\ &\times \exp(2\pi i(\mathbf{q}_2 \cdot \mathbf{x}(l_2) + \cdots + \mathbf{q}_n \cdot \mathbf{x}(l_n))) \end{aligned} \quad (3.123)$$

The coefficients Eq. (3.122) are symmetric in the indices and satisfy

$$\Phi^*(\mathbf{q}_1 j_1, \dots, \mathbf{q}_n j_n) = \Phi(-\mathbf{q}_1 j_1, \dots, -\mathbf{q}_n j_n). \quad (3.124)$$

The fact that  $\Delta(\mathbf{q}_1 + \cdots + \mathbf{q}_n)$  is included in the expansion coefficients places a restriction on the wavenumbers to be taken as the sum. In particular, for the first-order, as we have seen above, the only wavenumber that satisfies  $\Delta(\mathbf{q}) \neq 0$  is  $\mathbf{q} = \mathbf{0}$ , and similarly for the second-order,  $\Delta(\mathbf{q}_1 + \mathbf{q}_2) \neq 0$  is satisfied only if  $\mathbf{q}_2 = -\mathbf{q}_1$ . In the third-order, many wavenumbers satisfy  $\mathbf{q}_1 + \mathbf{q}_2 + \mathbf{q}_3 = \mathbf{G}$  as known from Umklap scattering. However, this strong restriction on the first- and second-orders, which are dominant contributions in the expansion, is important to make numerical calculations very efficient. In addition, in some literature, the eigenvectors of the phonon are written as

$$U_{\kappa \mu}(\mathbf{q} j) = \frac{1}{\sqrt{m_{\kappa}}} e_{\kappa \mu}(\mathbf{q} j), \quad (3.125)$$

which is normalized as

$$\sum_{\kappa\alpha} [U_{\kappa\alpha}(\mathbf{q}j)]^* U_{\kappa\alpha}(\mathbf{q}j') = \delta_{jj'}/m_{\kappa}. \quad (3.126)$$

In this case, all  $m_{\kappa}$  appearing in the expansion coefficient Eq. (3.123) disappear, so the form becomes very simple.

Finally, we write down the expansions for the dipole moment  $\mathbf{M}$  up to the second-order for future reference. The expansion itself is the same as in the energy case, except for the coefficients:

$$\begin{aligned} \mathbf{M}(q_1, \dots, q_n) &= \sum_{\kappa_1\mu_1} \dots \sum_{l_n\kappa_n\mu_n} \mathbf{M}_{\mu_1\dots\mu_n}^{0\kappa_1,l_2\kappa_2,\dots,l_n\kappa_n} \\ &\times \frac{1}{\sqrt{m_{\kappa_1}\dots m_{\kappa_n}}} e_{\mu_1}(q_1, \kappa_1) \dots e_{\mu_n}(q_n, \kappa_n) \\ &\times \exp(i(\mathbf{q}_2 \cdot \mathbf{r}_{l_2} + \dots + \mathbf{q}_n \cdot \mathbf{r}_{l_n})). \end{aligned} \quad (3.127)$$

The expansion is given by

$$\delta M_{\alpha} = \sqrt{N_{\text{cell}}} \sum_j M_{\alpha}(\mathbf{0}j) Q(\mathbf{0}j) + \frac{1}{2} \sum_{\mathbf{q}} \sum_{jj'} M_{\alpha}(\mathbf{q}j, -\mathbf{q}j') Q(\mathbf{q}j) Q(-\mathbf{q}j') + \dots \quad (3.128)$$

The first-order coefficients

$$M_{\alpha}(\mathbf{q}j) = \sum_{\kappa\mu} M_{\alpha,\mu}(\kappa) \frac{1}{\sqrt{m_{\kappa}}} e_{\kappa\mu}(\mathbf{q}j) \quad (3.129)$$

are called the mode effective charge vector [9]. The second order coefficients are (see also Eq. (3.68) for the second line)

$$M_{\alpha}(\mathbf{q}j, -\mathbf{q}j') = \sum_{\kappa_1\mu_1} \sum_{l_2\kappa_2\mu_2} M_{\alpha,\mu_1\mu_2}(0\kappa, l_2\kappa_2) \frac{1}{\sqrt{m_{\kappa_1}m_{\kappa_2}}} e_{\kappa\mu_1}(\mathbf{q}j) e_{\kappa_2\mu_2}(-\mathbf{q}j') \quad (3.130)$$

$$= \sum_{\kappa_1\mu_1} \sum_{l_2\kappa_2\mu_2} M_{\alpha,\mu_1\mu_2}(0\kappa, l_2\kappa_2) \frac{1}{\sqrt{m_{\kappa_1}m_{\kappa_2}}} e_{\kappa\mu_1}(\mathbf{q}j) e_{\kappa_2\mu_2}^*(\mathbf{q}j'). \quad (3.131)$$

which satisfy the following relation from permutation symmetry and Eq. (3.124)

$$M_{\alpha}(\mathbf{q}j, -\mathbf{q}j') = M_{\alpha}(-\mathbf{q}j', \mathbf{q}j) = M_{\alpha}^*(-\mathbf{q}j, \mathbf{q}j'). \quad (3.132)$$

## 3.6 Phonons

In quantum mechanics, position and momentum are replaced with corresponding operators,

$$u_{\mu}(l\kappa) \rightarrow \hat{u}_{\mu}(l\kappa) \quad (3.133)$$

$$p_{\mu}(l\kappa) \rightarrow \hat{p}_{\mu}(l\kappa), \quad (3.134)$$

which satisfies the commutation relation

$$[\hat{u}_{\mu_1}(l_1\kappa_1), \hat{p}_{\mu_2}(l_2\kappa_2)] = i\hbar \delta_{\mu_1\mu_2} \delta_{l_1l_2} \delta_{\kappa_1\kappa_2}. \quad (3.135)$$

The square brackets represent the commutator of the operators, which for bosons is:

$$[A, B] = AB - BA. \quad (3.136)$$

Using Eq. (3.79) and (3.82), we get the commutation relation for the normal coordinates,

$$\left[ \hat{Q}(\mathbf{q}_1 j_1), \hat{P}(\mathbf{q}_2 j_2) \right] = \frac{1}{N_{\text{cell}}} \sum_{\kappa_1 \mu_1} e_{\kappa_1 \mu_1}^*(\mathbf{q}_1 j_1) \sum_{\kappa_2 \mu_2} e_{\kappa_2 \mu_2}(\mathbf{q}_2 j_2) \sum_{l_1 l_2} \left[ \sqrt{m_{\kappa_1}} \hat{u}_{\mu_1}(l_1, \kappa_1) e^{-2\pi i \mathbf{q}_1 \cdot \mathbf{x}(l_1)}, \frac{\hat{p}_{\mu_2}(l_2, \kappa_2)}{\sqrt{m_{\kappa_2}}} e^{2\pi i \mathbf{q}_2 \cdot \mathbf{x}(l_2)} \right] \quad (3.137)$$

$$= \frac{1}{N_{\text{cell}}} \sum_{\kappa_1 \mu_1} e_{\kappa_1 \mu_1}^*(\mathbf{q}_1 j_1) \sum_{\kappa_2 \mu_2} e_{\kappa_2 \mu_2}(\mathbf{q}_2 j_2) \sum_{l_1 l_2} \sqrt{\frac{m_{\kappa_1}}{m_{\kappa_2}}} e^{2\pi i (-\mathbf{q}_1 \cdot \mathbf{x}(l_1) + \mathbf{q}_2 \cdot \mathbf{x}(l_2))} [\hat{u}_{\mu_1}(l_1, \kappa_1), \hat{p}_{\mu_2}(l_2, \kappa_2)] \quad (3.138)$$

$$= \frac{i\hbar}{N_{\text{cell}}} \sum_{\kappa_1 \mu_1} e_{\kappa_1 \mu_1}^*(\mathbf{q}_1 j_1) e_{\kappa_1 \mu_1}(\mathbf{q}_2 j_2) \sum_{l_1} e^{2\pi i (-\mathbf{q}_1 + \mathbf{q}_2) \cdot \mathbf{x}(l_1)} \quad (3.139)$$

$$= i\hbar \sum_{\kappa_1 \mu_1} e_{\kappa_1 \mu_1}^*(\mathbf{q}_1 j_1) e_{\kappa_1 \mu_1}(\mathbf{q}_2 j_2) \Delta(-\mathbf{q}_1 + \mathbf{q}_2) \quad (3.140)$$

$$= i\hbar \sum_{\kappa_1 \mu_1} e_{\kappa_1 \mu_1}^*(\mathbf{q}_1 j_1) e_{\kappa_1 \mu_1}(\mathbf{q}_2 j_2) \delta_{\mathbf{q}_1, \mathbf{q}_2} \quad (3.141)$$

The summation over  $\kappa_1$  and  $\mu_1$  are reduced to  $\delta_{j_1, j_2}$  from Eq. (3.61)

$$\left[ \hat{Q}(\mathbf{q}_1 j_1), \hat{P}(\mathbf{q}_2 j_2) \right] = i\hbar \delta_{j_1, j_2} \delta_{\mathbf{q}_1, \mathbf{q}_2}. \quad (3.142)$$

Similarly, we have

$$\left[ \hat{Q}(\mathbf{q}_1 j_1), \hat{Q}(\mathbf{q}_2 j_2) \right] = 0 \quad (3.143)$$

$$\left[ \hat{P}(\mathbf{q}_1 j_1), \hat{P}(\mathbf{q}_2 j_2) \right] = 0. \quad (3.144)$$

We now define creation and annihilation operators  $\hat{b}_{\mathbf{q}j}^\dagger, \hat{b}_{\mathbf{q}j}$  for each mode  $(\mathbf{q}, j)$

$$\hat{b}_{\mathbf{q}j} = \sqrt{\frac{\omega_{\mathbf{q}j}}{2\hbar}} \left( \hat{Q}_{\mathbf{q}j} + i \frac{\hat{P}_{-\mathbf{q}j}}{\omega_{\mathbf{q}j}} \right) \quad (3.145)$$

$$\hat{b}_{\mathbf{q}j}^\dagger = \sqrt{\frac{\omega_{\mathbf{q}j}}{2\hbar}} \left( \hat{Q}_{-\mathbf{q}j} - i \frac{\hat{P}_{\mathbf{q}j}}{\omega_{\mathbf{q}j}} \right), \quad (3.146)$$

which satisfy the following commutation relations

$$\left[ b_{\mathbf{q}_1 j_1}, b_{\mathbf{q}_2 j_2}^\dagger \right] = \delta_{\mathbf{q}_1 \mathbf{q}_2} \delta_{j_1 j_2} \quad (3.147)$$

$$\left[ b_{\mathbf{q}_1 j_1}, b_{\mathbf{q}_2 j_2} \right] = 0 \quad (3.148)$$

$$\left[ b_{\mathbf{q}_1 j_1}^\dagger, b_{\mathbf{q}_2 j_2}^\dagger \right] = 0. \quad (3.149)$$

Eq. (3.147) can be derived using Eq. (3.142), (3.145) and (3.146)

$$\left[ b_{\mathbf{q}_1 j_1}, b_{\mathbf{q}_2 j_2}^\dagger \right] = \frac{\sqrt{\omega_{\mathbf{q}_1 j_1} \omega_{\mathbf{q}_2 j_2}}}{2\hbar} \left[ \hat{Q}_{\mathbf{q}_1 j_1} + i \frac{\hat{P}_{-\mathbf{q}_1 j_1}}{\omega_{\mathbf{q}_1 j_1}}, \hat{Q}_{\mathbf{q}_2 j_2} - i \frac{\hat{P}_{\mathbf{q}_2 j_2}}{\omega_{\mathbf{q}_2 j_2}} \right] \quad (3.150)$$

$$= \frac{\sqrt{\omega_{\mathbf{q}_1 j_1} \omega_{\mathbf{q}_2 j_2}}}{2\hbar} \left( \frac{-i}{\omega_{\mathbf{q}_2 j_2}} \left[ \hat{Q}_{\mathbf{q}_1 j_1}, \hat{P}_{\mathbf{q}_2 j_2} \right] + \frac{i}{\omega_{\mathbf{q}_1 j_1}} \left[ \hat{Q}_{\mathbf{q}_2 j_2}, \hat{P}_{\mathbf{q}_1 j_1} \right] \right) \quad (3.151)$$

$$= \delta_{\mathbf{q}_1 \mathbf{q}_2} \delta_{j_1 j_2}. \quad (3.152)$$

The normal coordinates can be represented in terms of creation and annihilation operators as the inverse relations of Eq. (3.145) and (3.146)

$$\hat{Q}_{\mathbf{q}j} = \sqrt{\frac{\hbar}{2\omega_{\mathbf{q}j}}} \left( b_{\mathbf{q}j} + b_{-\mathbf{q}j}^\dagger \right) \quad (3.153)$$

$$\hat{P}_{\mathbf{q}j} = -i\sqrt{\frac{\hbar\omega_{\mathbf{q}j}}{2}} \left( b_{-\mathbf{q}j} - b_{\mathbf{q}j}^\dagger \right). \quad (3.154)$$

The Hamiltonian can be similarly expressed as

$$H = \frac{1}{2} \sum_{\mathbf{q}} \sum_j^{N_{\text{cell}}} \left[ \hat{P}(-\mathbf{q}j) \hat{P}(\mathbf{q}j) + \omega^2(\mathbf{q}j) \hat{Q}(-\mathbf{q}j) \hat{Q}(\mathbf{q}j) \right] \quad (3.155)$$

$$= \frac{1}{2} \sum_{\mathbf{q}} \sum_j^{N_{\text{cell}}} \left[ -\frac{\hbar\omega_{\mathbf{q}j}}{2} (b_{\mathbf{q}j} - b_{-\mathbf{q}j}^\dagger) (b_{-\mathbf{q}j} - b_{\mathbf{q}j}^\dagger) + \omega^2(\mathbf{q}j) \frac{\hbar}{2\omega_{\mathbf{q}j}} (b_{-\mathbf{q}j} + b_{\mathbf{q}j}^\dagger) (b_{\mathbf{q}j} + b_{-\mathbf{q}j}^\dagger) \right] \quad (3.156)$$

$$= \frac{1}{2} \sum_{\mathbf{q}} \sum_j^{N_{\text{cell}}} \frac{\hbar\omega_{\mathbf{q}j}}{2} (b_{\mathbf{q}j} b_{\mathbf{q}j}^\dagger + b_{\mathbf{q}j}^\dagger b_{\mathbf{q}j} + b_{-\mathbf{q}j} b_{-\mathbf{q}j}^\dagger + b_{-\mathbf{q}j}^\dagger b_{-\mathbf{q}j}) \quad (3.157)$$

Using Eq. (3.147), we obtain

$$H = \frac{1}{2} \sum_{\mathbf{q}} \sum_j^{N_{\text{cell}}} \hbar\omega_{\mathbf{q}j} (b_{\mathbf{q}j}^\dagger b_{\mathbf{q}j} + b_{-\mathbf{q}j}^\dagger b_{-\mathbf{q}j} + 1) \quad (3.158)$$

$$= \sum_{\mathbf{q}j}^{N_{\text{cell}}} \hbar\omega_{\mathbf{q}j} \left( b_{\mathbf{q}j}^\dagger b_{\mathbf{q}j} + \frac{1}{2} \right). \quad (3.159)$$

We define a new operator  $A_{\mathbf{q}j}$  called a phonon operator as [123]

$$A_{\mathbf{q}j} = b_{\mathbf{q}j} + b_{-\mathbf{q}j}^\dagger \quad (3.160)$$

$$A_{\mathbf{q}j}^\dagger = b_{-\mathbf{q}j} + b_{\mathbf{q}j}^\dagger = A_{-\mathbf{q}j}, \quad (3.161)$$

which satisfy

$$\hat{Q}_{\mathbf{q}j} = \sqrt{\frac{\hbar}{2\omega_{\mathbf{q}j}}} A_{\mathbf{q}j}. \quad (3.162)$$

Expressions written in complex normal coordinates can be rewritten with  $A_{\mathbf{q}j}$  using Eq. (3.162), and it is the translation from classical to quantum mechanics. The  $n$ th order expansion of the energy and dipole moment Eq. (3.122) can be quantized as

$$U_n = \frac{N_{\text{cell}}}{n!} \left( \frac{\hbar}{2N_{\text{cell}}} \right)^{n/2} \sum_{(\mathbf{q}_1 j_1)} \cdots \sum_{(\mathbf{q}_n j_n)} \Delta(\mathbf{q}_1 + \cdots + \mathbf{q}_n) \times \frac{\Phi(\mathbf{q}_1 j_1, \cdots, \mathbf{q}_n j_n)}{\sqrt{\omega_{\mathbf{q}_1 j_1} \cdots \omega_{\mathbf{q}_n j_n}}} A_{\mathbf{q}_1 j_1} \cdots A_{\mathbf{q}_n j_n}, \quad (3.163)$$

$$M_n = \frac{N_{\text{cell}}}{n!} \left( \frac{\hbar}{2N_{\text{cell}}} \right)^{n/2} \sum_{(\mathbf{q}_1 j_1)} \cdots \sum_{(\mathbf{q}_n j_n)} \Delta(\mathbf{q}_1 + \cdots + \mathbf{q}_n) \times \frac{M(\mathbf{q}_1 j_1, \cdots, \mathbf{q}_n j_n)}{\sqrt{\omega_{\mathbf{q}_1 j_1} \cdots \omega_{\mathbf{q}_n j_n}}} A_{\mathbf{q}_1 j_1} \cdots A_{\mathbf{q}_n j_n}. \quad (3.164)$$

## 3.7 Phonon Green's Function

### 3.7.1 Green's function at finite temperature

We consider a system described by Hamiltonian  $H$  in thermal equilibrium states at a finite temperature  $T$ . The expected value of any operator  $A$  is given by

$$\langle A \rangle = \frac{\text{Tr} \{ e^{-\beta H} \hat{A} \}}{Z} \quad (3.165)$$

$$Z = \text{Tr} \{ e^{-\beta H} \}, \quad (3.166)$$

where  $\beta = 1/k_B T$  is the inverse temperature with  $k_B$  being the Boltzman constant, and  $Z$  is the partition function.  $\text{Tr}$  denotes the trace of the expression. In order to align the time-dependence of the operator  $A^{-i\hat{H}t}$ , we introduce imaginary time

$$\tau = it/\hbar. \quad (3.167)$$

In the Heisenberg picture, the imaginary time operator is defined as

$$A(\tau) = e^{\tau H} A(0) e^{-\tau H}. \quad (3.168)$$

We define the Green's function of two operators  $A$  and  $B$

$$G(A(\tau), B(\tau')) = -\langle T_\tau A(\tau) B(\tau') \rangle, \quad (3.169)$$

where the triangular brackets denote the thermal average Eq. (3.165).  $T_\tau$  is the time-ordering operator, which reorders the operators based on the  $\tau$ -values such that they are always in chronological order.

$$T_\tau A(\tau) B(\tau') = \begin{cases} A(\tau) B(\tau') & (\tau > \tau') \\ B(\tau') A(\tau) & (\tau < \tau') \end{cases} \quad (3.170)$$

$$= \theta(\tau - \tau') A(\tau) B(\tau') + \theta(\tau' - \tau) B(\tau') A(\tau) \quad (3.171)$$

where  $\theta(\tau)$  is the step function. Using Eq. (3.166) and (3.168),  $G(A(\tau), B(\tau'))$  is written as

$$G(A(\tau), B(\tau')) = \begin{cases} \frac{-1}{Z} \text{Tr} \left\{ e^{-\beta H} e^{\tau H} A(0) e^{-\tau H} e^{\tau' H} B(0) e^{-\tau' H} \right\} & \tau > 0 \\ \frac{-1}{Z} \text{Tr} \left\{ e^{-\beta H} e^{\tau' H} B(0) e^{-\tau' H} e^{\tau H} A(0) e^{-\tau H} \right\} & \tau < 0 \end{cases} \quad (3.172)$$

The finite temperature Green's function has several important properties. First, it depends only on  $\tau - \tau'$ . To show this, we use the cyclic property of the trace

$$\text{Tr} \{ABC\} = \text{Tr} \{CAB\}. \quad (3.173)$$

For  $\tau > \tau'$ , we have

$$G(A(\tau), B(\tau')) = \frac{1}{Z} \text{Tr} \left\{ e^{-\beta H} e^{\tau H} A(0) e^{-\tau H} e^{\tau' H} B(0) e^{-\tau' H} \right\} \quad (3.174)$$

$$= \frac{1}{Z} \text{Tr} \left\{ e^{-\tau' H} e^{-\beta H} e^{\tau H} A(0) e^{-\tau H} e^{\tau' H} B(0) \right\}. \quad (3.175)$$

Using the fact that the functions of  $H$  commute, we get

$$G(A(\tau), B(\tau')) = \frac{1}{Z} \text{Tr} \left\{ e^{-\beta H} e^{H(\tau - \tau')} A(0) e^{-H(\tau - \tau')} B(0) \right\} \quad (3.176)$$

$$= G(A(\tau - \tau'), B(0)). \quad (3.177)$$

We have the same relation for  $\tau < \tau'$  similarly. Therefore, we conclude that  $G(A(\tau), B(\tau'))$  only depends on  $\tau - \tau'$ . For simplicity, we write

$$G(\tau) = G(A(\tau), B(0)). \quad (3.178)$$

Second,  $G(\tau)$  take finite values with only  $-\beta < \tau < \beta$ . For  $\tau > 0$ , we have

$$G(A, B, \tau) = \frac{1}{Z} \text{Tr} \left\{ e^{(-\beta + \tau)H} A(0) e^{-\tau H} B(0) \right\}. \quad (3.179)$$

Expanding this expression in the eigenstates yields terms like  $e^{-\tau E}$  using the eigenenergy  $E$ , which is positive and generally takes values up to infinity. The exponent becomes negative and converges when  $0 < \tau < \beta$ . Similarly, for  $\tau < 0$ , convergence is achieved for  $\beta < \tau < 0$ . Therefore, the definition range of the finite temperature Green's function can be restricted to  $-\beta < \tau < \beta$ .

Finally,  $G(\tau)$  has the periodicity:

$$G(\tau + \beta) = G(\tau) \quad -\beta < \tau < 0 \quad (3.180)$$

$$G(\tau - \beta) = G(\tau) \quad 0 < \tau < \beta. \quad (3.181)$$

This is again proved using the cyclic property of the trace. For  $0 < \tau < \beta$ , namely  $-\beta < \tau - \beta < 0$ , we obtain

$$G(\tau - \beta) = \frac{-1}{Z} \text{Tr} \left\{ e^{-\beta H} A(0) e^{(\tau - \beta)H} B(0) e^{-(\tau - \beta)H} \right\} \quad (3.182)$$

$$= \frac{-1}{Z} \text{Tr} \left\{ e^{(\tau - \beta)H} B(0) e^{-(\tau - \beta)H} e^{-\beta H} A(0) \right\} \quad (3.183)$$

$$= \frac{-1}{Z} \text{Tr} \left\{ e^{(\tau - \beta)H} B(0) e^{-\tau H} A(0) \right\} \quad (3.184)$$

$$= G(\tau). \quad (3.185)$$

As the finite temperature Green's function is defined in  $[-\beta, \beta]$ , we can expand it in the Fourier series with period  $2\beta$ <sup>\*2</sup>.

$$G(\tau) = \frac{1}{\beta} \sum_{n=-\infty}^{\infty} G(i\omega_n) \exp(-i\omega_n \tau) \quad (3.186)$$

$$\omega_n = \frac{2\pi n}{\beta} \quad (3.187)$$

$\omega_n$  is called Matsubara frequencies for boson<sup>\*3</sup>. The Fourier coefficients are given by:

$$G(i\omega_n) = \frac{1}{2} \int_{-\beta}^{\beta} G(\tau) \exp(i\omega_n \tau) d\tau \quad (3.193)$$

$$= \int_0^{\beta} G(\tau) \exp(i\omega_n \tau) d\tau, \quad (3.194)$$

where we have used Eq. (3.181) for the second line to restrict the range of the integration.

### 3.7.2 Retarded Green's function

The response of a system to an externally applied force is most readily obtained from the retarded Green's function. This function for two field operators is defined by:<sup>\*4</sup>

$$G^R(A, B, t) = \frac{1}{i\hbar} \theta(t) \langle [A(t), B(0)] \rangle \quad (3.195)$$

In this subsection, We review the relationship between the finite temperature Green's function and the retarded Green's function. The Fourier transform of  $G^R(A, B, t)$  is defined as

$$G^R(\omega) = \int_{-\infty}^{\infty} e^{i\omega t} G^R(t) dt \quad (3.196)$$

$$G^R(t) = \frac{1}{2\pi} \int_{-\infty}^{\infty} e^{-i\omega t} G^R(\omega) d\omega. \quad (3.197)$$

We also introduce time-correlation function  $F(A, B, t)$

$$F(A, B, t) = \langle A(t)B(0) \rangle \quad (3.198)$$

---

<sup>\*2</sup> There is a style of which way to push the inverse temperature  $\beta$ . In this document,  $G(\tau)$  is set to have the dimension of energy.

<sup>\*3</sup> It is easily derived as follows. Let us start with the Fourier transformation

$$G(\tau) = \frac{1}{\beta} \sum_{n=-\infty}^{\infty} G(n) \exp(-i\pi n \tau / \beta). \quad (3.188)$$

Dividing the integration region of the inverse transformation into  $[-\beta, 0]$  and  $[0, \beta]$ , and using Eq. (3.181), we obtain

$$G(n) = \frac{1}{2} \int_{-\beta}^{\beta} d\tau e^{i\pi n \tau / \beta} G(\tau) \quad (3.189)$$

$$= \frac{1}{2} \int_{-\beta}^0 d\tau e^{i\pi n \tau / \beta} G(\tau) + \frac{1}{2} \int_0^{\beta} d\tau e^{i\pi n \tau / \beta} G(\tau) \quad (3.190)$$

$$= \frac{1}{2} \int_{-\beta}^0 d\tau e^{i\pi n \tau / \beta} G(\tau + \beta) + \frac{1}{2} \int_0^{\beta} d\tau e^{i\pi n \tau / \beta} G(\tau) \quad (3.191)$$

$$= (e^{-i\pi n} + 1) \frac{1}{2} \int_0^{\beta} d\tau e^{i\pi n \tau / \beta} G(\tau), \quad (3.192)$$

which is none zero only if  $n$  is an odd number.

<sup>\*4</sup> There seem to be several schools of thought on the definition of the delayed Green's function in terms of sign and coefficients, but in this thesis, the analytical connection between the finite temperature Green's function and the delayed Green's function is kept free of extra coefficients.

and its Fourier transform  $F(A, B, \omega)$

$$F(\omega) = \int_{-\infty}^{\infty} \langle A(t)B(0) \rangle e^{i\omega t} dt \quad (3.199)$$

$$F(A, B, t) = \frac{1}{2\pi} \int_{-\infty}^{\infty} F(\omega) e^{-i\omega t} d\omega. \quad (3.200)$$

We show below that  $G$  and  $G^R$  are related by an analytic connection via  $F(\omega)$ . The key equation, called Kubo-Martin-Schwinger identity, is derived using the circularity of the trace and obvious identity  $I = e^{+\beta H} e^{-\beta H}$

$$\langle A(t)B(0) \rangle = \text{Tr} \left\{ e^{-\beta H} e^{iHt/\hbar} A(0) e^{-iHt/\hbar} B(0) \right\} \quad (3.201)$$

$$= \text{Tr} \left\{ e^{-\beta H} e^{iHt/\hbar} A(0) e^{-iHt/\hbar} e^{+\beta H} e^{-\beta H} B(0) \right\} \quad (3.202)$$

$$= \text{Tr} \left\{ e^{-\beta H} B(0) e^{-\beta H} e^{iHt/\hbar} A(0) e^{-iHt/\hbar} e^{+\beta H} \right\} \quad (3.203)$$

$$= \text{Tr} \left\{ e^{-\beta H} B(0) A(t + i\beta) \right\} = \langle B(0) A(t + i\beta\hbar) \rangle \quad (3.204)$$

Using this equation, the Fourier transform of the retarded Green's function Eq. (3.197) becomes

$$G^R(\omega) = \frac{1}{i\hbar} \int_{-\infty}^{\infty} e^{i\omega t} \theta(t) \langle A(t)B(0) - B(0)A(t) \rangle dt \quad (3.205)$$

$$= \frac{1}{i\hbar} \int_{-\infty}^{\infty} e^{i\omega t} \theta(t) \langle A(t)B(0) - A(t - i\beta\hbar)B(0) \rangle dt. \quad (3.206)$$

Substituting Eq. (3.200) into Eq. (3.206) yields

$$G^R(\omega) = \frac{1}{i\hbar} \int_{-\infty}^{\infty} \frac{d\omega'}{2\pi} \int_{-\infty}^{\infty} dt e^{i\omega t} \theta(t) \left\{ F(\omega') e^{-i\omega' t} - F(\omega') e^{-i\omega' (t - i\beta\hbar)} \right\}. \quad (3.207)$$

Executing the integral of time, we have

$$G^R(\omega) = \frac{-1}{i\hbar} \int_{-\infty}^{\infty} \frac{d\omega'}{2\pi} \frac{F(\omega') (1 - e^{-\beta\hbar\omega'})}{i(\omega - \omega') + \delta} \quad (3.208)$$

$$= \int_{-\infty}^{\infty} \frac{d\omega'}{2\pi} \frac{(1 - e^{-\beta\hbar\omega'})}{\hbar(\omega - \omega') + \delta} F(\omega'), \quad (3.209)$$

where we utilize the relation obtained by integrating the step function by parts:

$$\int_{-\infty}^{\infty} e^{i\omega t - \delta t} \theta(t) dt = \left[ \frac{e^{i\omega t - \delta t}}{i\omega - \delta} \theta(t) \right] - \int_{-\infty}^{\infty} \frac{e^{i\omega t - \delta t}}{i\omega - \delta} \delta(t) dt \quad (3.210)$$

$$= \frac{-1}{i\omega - \delta}. \quad (3.211)$$

$\delta > 0$  is an infinitesimal constant added to converge the integral with  $t \rightarrow \infty$ .

Next, we contemplate expressing the Fourier transform of the finite temperature Green's function Eq. (3.194) in terms of  $F(\omega)$ . Substituting Eq. (3.200) into Eq. (3.194) and using the relation  $\tau = t/i\hbar$  yields

$$G(i\omega_n) = - \int_0^\beta e^{i\omega_n \tau} \langle A(\tau)B(0) \rangle d\tau \quad (3.212)$$

$$= - \int_0^\beta d\tau \int_{-\infty}^{\infty} \frac{d\omega'}{2\pi} e^{i\omega_n \tau} F(\omega') e^{-i\omega'(-i\hbar\tau)} \quad (3.213)$$

$$= \int_{-\infty}^{\infty} \frac{d\omega'}{2\pi} \frac{1 - e^{-\beta\hbar\omega'}}{i\omega_n - \hbar\omega'} F(\omega') \quad (3.214)$$

Comparing Eq. (3.209) and (3.214), we find that the both  $G^R(\omega)$  and  $G(i\omega_n)$  are written in terms of the newly defined complex function  $Z(z)$

$$Z(z) = \int_{-\infty}^{\infty} \frac{d\omega'}{2\pi} \frac{1 - e^{-\beta\hbar\omega'}}{z - \hbar\omega'} F(\omega') \quad (3.215)$$

$$G^R(\omega) = Z(z = \hbar\omega + i\delta) \quad (3.216)$$

$$G(i\omega_n) = Z(z = \omega_n), \quad (3.217)$$

where

$$\rho(\omega) = (1 - e^{-\beta\hbar\omega}) F(\omega) \quad (3.218)$$

is called the spectral function. For practical calculations, the finite temperature Green's function can first be obtained by perturbation theory, which allows the complex function  $Z(z)$  to be known on a limited number of points  $i\omega_n$ . From here,  $G^R(\omega)$  can be obtained by determining  $Z(z)$  in the full complex plane by analytic connection. The behavior of  $G^R(\omega)$  at infinity is  $G^R(\omega) \simeq 1/\omega$  [124], so this analytic connection can be uniquely determined by simply replacing  $i\omega_n = \hbar\omega + i\delta$ ,

$$G^R(\omega) = G(i\omega_n \rightarrow \hbar\omega + i\delta). \quad (3.219)$$

### 3.7.3 Perturbation theory for the thermodynamic Green's function

The Hamiltonian is divided into an unperturbed  $H_0$  and a perturbed part  $H_A$ . Although, in our case, the harmonic Hamiltonian is chosen as the non-perturbative Hamiltonian, we will not specify the form of  $H_0$  in this subsection.

$$H = H_0 + H_A \quad (3.220)$$

Operators are written in the interaction representation as

$$\tilde{A}(\tau) = \exp(\tau H_0) A(0) \exp(-\tau H_0) \quad (3.221)$$

To derive the perturbative expansion for the Green's function, we first consider the imaginary time evolution operator

$$U(\tau, \tau') = e^{\tau H_0} e^{-(\tau - \tau') H} e^{-\tau' H_0}, \quad (3.222)$$

with which we can connect the Heisenberg and interacting pictures as

$$O_H(\tau) = U(0, \tau) O_I(\tau) U(\tau, 0). \quad (3.223)$$

The derivative of  $U(\tau, \tau')$  with  $\tau$  is given by

$$\frac{dU(\tau, \tau')}{d\tau} = -H_A(\tau) U(\tau, \tau'), \quad (3.224)$$

where

$$H_A(\tau) = \exp(\tau H_0) H_A(0) \exp(-\tau H_0) \quad (3.225)$$

is the perturbative Hamiltonian in the interacting representation. We can solve this differential equation with the initial condition  $U(\tau, \tau') = 1$

$$U(\tau, \tau') = \sum_{n=0}^{\infty} \frac{(-1)^n}{n!} \int_{\tau'}^{\tau} d\tau_1 \cdots \int_{\tau'}^{\tau} d\tau_n T_{\tau} [H_A(\tau_1) \cdots H_A(\tau_n)], \quad (3.226)$$

which is formally written as

$$U(\tau, \tau') = T_{\tau} \exp \left[ - \int_{\tau'}^{\tau} d\tau_1 H_A(\tau_1) \right]. \quad (3.227)$$

As the finite temperature Green's function is defined using the Heisenberg picture in Eq. (3.169), we rewrite it in terms of the interacting picture using Eq. (3.223). For  $\tau > 0$ , we have

$$G(\tau) = -\frac{1}{Z} \text{Tr} \{ e^{-\beta H} A(\tau) B(0) \} \quad (3.228)$$

$$= -\frac{1}{Z} \text{Tr} \{ e^{-\beta H} U(0, \tau) A_I(\tau) U(\tau, 0) B_I(0) \} \quad (3.229)$$

Using

$$e^{-\beta H} = e^{-\beta H_0} U(\beta, 0), \quad (3.230)$$

and the chain rule

$$U(\tau, \tau') = U(\tau, \tau'')U(\tau'', \tau), \quad (3.231)$$

we obtain

$$G(\tau) = -\frac{1}{Z} \text{Tr} \{ e^{-\beta H_0} U(\beta, 0) U(0, \tau) A_I(\tau) U(\tau, 0) B_I(0) \} \quad (3.232)$$

$$= -\frac{1}{Z} \text{Tr} \{ e^{-\beta H_0} U(\beta, 0) U(0, \tau) A_I(\tau) U(\tau, 0) B_I(0) \} \quad (3.233)$$

$$= -\frac{1}{Z} \text{Tr} \{ e^{-\beta H_0} U(\beta, \tau) A_I(\tau) U(\tau, 0) B_I(0) \}. \quad (3.234)$$

In the same way, we get the expression for  $\tau < 0$

$$G(\tau) = -\frac{1}{Z} \text{Tr} \{ e^{-\beta H_0} U(\beta) B_I(0) U(0, \tau) A_I(\tau) U(\tau, 0) \}. \quad (3.235)$$

Substituting Eq. (3.226) into Eq. (3.234) and (3.235) with doing some algebra, we finally reach to

$$G(\tau) = -\frac{1}{Z} \text{Tr} e^{-\beta H_0} \sum_{n=0}^{\infty} \frac{(-1)^n}{n!} \int_0^{\beta} d\tau_1 \cdots \int_0^{\beta} d\tau_n T_{\tau} [A_I(\tau) B_I(0) H_A(\tau_1) \cdots H_A(\tau_n)] \quad (3.236)$$

The partition function Eq. (3.166) is also written in terms of the interacting representation using Eq. (3.230):

$$Z = \text{Tr} e^{-\beta H_0} \sum_{n=0}^{\infty} \frac{(-1)^n}{n!} \int_0^{\beta} d\tau_1 \cdots \int_0^{\beta} d\tau_n T_{\tau} [H_A(\tau_1) \cdots H_A(\tau_n)]. \quad (3.237)$$

In the above equations, all the operators are written in the interacting picture, and the thermal average is taken using the non-interacting Hamiltonian  $H_0$ , which we define with the subscription  $\langle \cdot \rangle_0$  as

$$\langle O \rangle_0 = \frac{1}{Z_0} \text{Tr} e^{-\beta H_0} O. \quad (3.238)$$

$Z_0$  is the partition function in the non-interacting system

$$Z_0 = \text{Tr} e^{-\beta H_0}. \quad (3.239)$$

Using this notation, Eq. (3.236) is written as

$$G(\tau) = -\frac{\sum_{n=0}^{\infty} \frac{(-1)^n}{n!} \int_{\tau'}^{\tau} d\tau_1 \cdots \int_{\tau'}^{\tau} d\tau_n \langle T_{\tau} [A_I(\tau) B_I(0) H_A(\tau_1) \cdots H_A(\tau_n)] \rangle_0}{\sum_{n=0}^{\infty} \frac{(-1)^n}{n!} \int_{\tau'}^{\tau} d\tau_1 \cdots \int_{\tau'}^{\tau} d\tau_n \langle T_{\tau} [H_A(\tau_1) \cdots H_A(\tau_n)] \rangle_0}. \quad (3.240)$$

In our case, the operators  $A$ ,  $B$ ,  $H_A$  are expanded in powers of the phonon operators defined in the wave vector representation (Eq. (3.160)). We can use Bloch-De Dominics theorem [125] to decompose those phonon operators into the sum of the products of non-interacting Green's functions, each of which contribution can be represented schematically in a so-called Feynman diagram.

### 3.7.4 Harmonic phonon Green's function

The one-phonon Green's function is defined by

$$G_{q,q'}(\tau) = \langle T_{\tau} A_q(\tau) A_{q'}^{\dagger}(0) \rangle \quad (3.241)$$

Here and in the following, we use  $q$  for the shorthand notation of  $(\mathbf{q}, j)$ , satisfying  $q = (\mathbf{q}, j)$  and  $-q = (-\mathbf{q}, j)$ . In the case of harmonic approximation, the Hamiltonian is given by

$$\hat{H}_0 = \sum_q \hbar \omega_q \left( b_q^{\dagger} b_q + \frac{1}{2} \right). \quad (3.242)$$

In particular, the phonon Green's function in the harmonic approximation is called the free phonon Green's function, denoted by  $G_{q,q'}^0(\tau)$ . As we will see below,  $G_{q,q'}^0(\tau)$  is easily calculated and is diagonal with respect to mode indices  $q$  and  $q'$ . Using the Baker-Hausdorff theorem

$$e^A C e^{-A} = C + [A, C] + \frac{1}{2!} [A, [A, C]] + \frac{1}{3!} [A, [A, [A, C]]] + \cdots, \quad (3.243)$$

the Heisenberg operators can be written

$$b_q(\tau) = e^{\tau H_0} b_q(0) e^{-\tau H_0} = e^{-\tau \omega_q} b_q(0) \quad (3.244)$$

$$b_q^\dagger(\tau) = e^{\tau H_0} b_q^\dagger(0) e^{-\tau H_0} = e^{\tau \omega_q} b_q^\dagger(0). \quad (3.245)$$

The one-phonon Green's function for  $0 < \tau < \beta$  is then given by

$$G_{q,q'}^0(\tau) = \langle A_q(\tau) A_{q'}^\dagger(0) \rangle \quad (3.246)$$

$$= \langle (b_q(\tau) + b_{-q}^\dagger(\tau)) (b_{-q'} + b_{q'}^\dagger) \rangle \quad (3.247)$$

$$= \langle (e^{-\tau \omega_q} b_q + e^{\tau \omega_q} b_{-q}^\dagger) (b_{-q'} + b_{q'}^\dagger) \rangle \quad (3.248)$$

We use Eq. (3.160) for the second line and Eq. (3.244) and (3.245) for the last line. Applying the commutation relations yields

$$G_{q,q'}^0(\tau) = \delta_{qq'} \left( e^{-\tau \omega_q} \langle b_q^\dagger b_q + 1 \rangle + e^{\tau \omega_q} \langle b_{-q}^\dagger b_{-q} \rangle \right) \quad (3.249)$$

$$= e^{-\tau \omega_q} (n_q + 1) + e^{\tau \omega_q} n_{-q}, \quad (3.250)$$

where  $n_q = \langle b_q^\dagger b_q \rangle$  is the expectation value of the particle number. For bosonic free particle systems, it is identical to the Bose-Einstein distribution function:

$$n_q = n(\omega_q) = \frac{1}{e^{\beta \omega_q} - 1}. \quad (3.251)$$

Obviously, we have  $n_q = n_{-q}$ . Expression in terms of Matsubara frequencies is given by Eq. (3.194)

$$G_{qq'}^0(i\omega_n) = \delta_{qq'} \int_0^\beta d\tau [e^{-\tau \omega_q} (n_q + 1) + e^{\tau \omega_q} n_{-q}] e^{-i\omega_n \tau} \quad (3.252)$$

$$= \delta_{qq'} \left[ -\frac{e^{-\beta \omega_q} - 1}{\omega_q + i\omega_n} (n_q + 1) + \frac{e^{\beta \omega_q} - 1}{\omega_q - i\omega_n} n_q \right] \quad (3.253)$$

$$= \delta_{qq'} \frac{2\hbar \omega_q}{(\hbar \omega_q)^2 - (i\omega_n)^2}, \quad (3.254)$$

where we use the relation  $e^{-i\omega_n \beta} = 1$ .

### 3.7.5 Phonon self-energy

It is convenient to introduce self-energy  $\Sigma_q(i\omega_n)$  through the Dyson equation

$$G_q(i\omega_n) = G_q^0(i\omega_n) + G_q^0(i\omega_n) \Sigma_q(i\omega_n) G_q(i\omega_n). \quad (3.255)$$

Substituting Eq. (3.254) into Eq. (3.255), we obtain the expression for the one-phonon Green's function.

$$G_q(i\omega_n) = \frac{2\hbar \omega_q}{(\omega_q)^2 - (i\omega_n)^2 - 2\omega_q \Sigma_q(\omega)}. \quad (3.256)$$

In general, the self-energy is complex, and its real part is called the frequency shift  $\Delta_q(\omega)$  and its imaginary part is called the linewidth  $\Gamma_q(\omega)$ . We note that the frequency shift is defined as the minus of the real part of the self-energy.

$$\Sigma_q(\omega) = \text{Re } \Sigma_q(\omega) + i \text{Im } \Sigma_q(\omega) \quad (3.257)$$

$$\Delta_q(\omega) = -\text{Re } \Sigma_q(\omega) \quad (3.258)$$

$$\Gamma_q(\omega) = \text{Im } \Sigma_q(\omega) \quad (3.259)$$

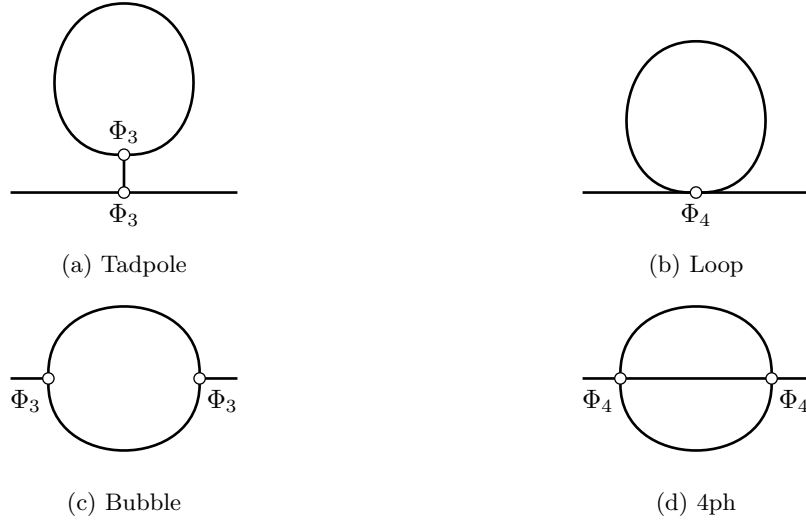


Fig. 3.2: Feynman diagrams of phonon self energies. Solid lines and open circles represent phonon proper-gators and phonon vertexes, respectively.

The physical meanings of frequency shift and line width are as follows. Assuming that they are independent of frequency and sufficiently small, the Green's function may be rewritten as follows:

$$G_q(\omega) = \frac{2\omega_q}{(\omega_q + \Delta)^2 - \omega^2 - \Delta^2 - 2i\omega_q\Gamma} \quad (3.260)$$

$$\simeq \frac{2\omega_q}{(\omega_q + \Delta)^2 - \omega^2 - 2i\omega_q\Gamma}. \quad (3.261)$$

The Green's function is peaked at the renormalized phonon frequency  $\omega_q + \Delta$  with the width at half maximum of  $\Gamma$ .

Perturbation theory is used to calculate specific self-energy expressions. We rewrite the Hamiltonian Eq. (3.163) specifying the order  $\lambda$

$$H = H_0 + \lambda\hat{U}_3 + \lambda^2\hat{U}_4 + \lambda^3\hat{U}_5 + \lambda^4\hat{U}_6 + \dots \quad (3.262)$$

The order of the perturbation is defined as the order of the lambda. As there is no first order  $\mathcal{O}(\lambda)$  contribution, the lowest order is  $\mathcal{O}(\lambda^2)$  and the corresponding Feynman diagrams are called tadpole ( $U_3^2$ ), Bubble ( $U_3^2$ ), and Loop ( $U_4$ ) diagrams. The bubble diagram is physically interpreted as three phonon scattering, which means one phonon emits two phonons or two phonons merge into one phonon. The next order is  $\mathcal{O}(\lambda^4)$ , where 4-phonon scattering, which has recently attracted much attention, belongs. For later discussion, we introduce the phonon scattering matrix  $V$  as

$$V(q_1, \dots, q_n) = N_{\text{cell}} \left( \frac{\hbar}{2N_{\text{cell}}} \right)^{n/2} \Delta(\mathbf{q}_1 + \dots + \mathbf{q}_n) \times \frac{\Phi(\mathbf{q}_1 j_1, \dots, \mathbf{q}_n j_n)}{\sqrt{\omega_{\mathbf{q}_1 j_1} \dots \omega_{\mathbf{q}_n j_n}}}, \quad (3.263)$$

with which the  $n$ th order Hamiltonian is rewritten as

$$\hat{U}_n = \frac{1}{n!} \sum_{(\mathbf{q}_1 j_1)} \dots \sum_{(\mathbf{q}_n j_n)} V(q_1, \dots, q_n) A_{\mathbf{q}_1 j_1} \dots A_{\mathbf{q}_n j_n}. \quad (3.264)$$

In this thesis, we concentrate on the following terms

$$\Sigma = \Sigma^T + \Sigma^B + \Sigma^L + \Sigma^{4\text{ph}}. \quad (3.265)$$

Here, T, B, L, and 4ph stand for tadpole, bubble, loop, and four phonon scattering. Figure 3.2 depicts the Feynman diagrams of these self-energies. These diagrams are given by the following formulae [126] according to the Feynman rule.

$$\Sigma_q^T(\omega) = \frac{-1}{\hbar} \sum_{q_2, j_1 = \text{TO}} V(-q, q, \mathbf{0}j_1) V(\mathbf{0}j_1, q_2, -q_2) \frac{2n_2 + 1}{\omega_{\mathbf{0}j_1}} \quad (3.266)$$

$$\Sigma_q^B(\omega) = \frac{1}{2\hbar} \sum_{q_1, q_2, s \pm 1} |V(-q, q_1, q_2)|^2 \left[ \frac{n_1 + n_2 + 1}{s\omega_c + \omega_{q_1} + \omega_{q_2}} - \frac{n_1 - n_2}{s\omega_c + \omega_{q_1} - \omega_{q_2}} \right] \quad (3.267)$$

$$\Sigma_q^L(\omega) = - \sum_{q_1} V(q, -q, q_1, -q_1) \frac{2n_1 + 1}{2} \quad (3.268)$$

$$\Sigma_q^{4\text{ph}}(\omega) = \frac{1}{6\hbar} \sum_{q_1 q_2 q_3, s \pm 1} V(-q, q_1, q_2, q_3) V(-q_1, -q_2, -q_3, q) \left[ \frac{(n_1 + 1)(n_2 + 1)(n_3 + 1) - n_1 n_2 n_3}{s\omega_c + \omega_{q_1} + \omega_{q_2} + \omega_{q_3}} + \frac{3n_1(n_2 + 1)(n_3 + 1) - (n_1 + 1)n_2 n_3}{s\omega_c - \omega_{q_1} + \omega_{q_2} + \omega_{q_3}} \right] \quad (3.269)$$

$n_i = n(\omega_{q_i}) = 1/(e^{\beta\hbar\omega_{q_i}} - 1)$  is the Bose – Einstein distribution function and  $\omega_c = \omega + i0^+$  with  $0^+$  being a positive infinitesimal. In addition, the summation in Eq. (3.267) is restricted to the pairs  $(\mathbf{q}_1, \mathbf{q}_2)$  satisfying the momentum conservation  $\mathbf{q}_1 + \mathbf{q}_2 = \mathbf{q} + \mathbf{G}$ , where  $\mathbf{G}$  is a reciprocal lattice vector. Similarly, the sum of the 4ph diagram in Eq. (3.269) is limited to the pairs  $(\mathbf{q}_1, \mathbf{q}_2, \mathbf{q}_3)$  satisfying  $\mathbf{q}_1 + \mathbf{q}_2 + \mathbf{q}_3 = \mathbf{q} + \mathbf{G}$ .  $V(q_1, q_2, q_3)$  and  $V(q_1, q_2, q_3, q_4)$  are three and four phonon scattering matrices defined as (see Eq. (3.163))

$$V(q_1, q_2, q_3) = \frac{1}{N_{\text{cell}}^{1/2}} \left( \frac{\hbar}{2} \right)^{3/2} \sum_{\substack{\kappa_1 \mu_1 \\ l_2 \kappa_2 \mu_2 \\ l_3 \kappa_3 \mu_3}} \Phi_{\mu_1 \mu_2 \mu_3}^{0\kappa_1, l_2 \kappa_2, l_3 \kappa_3} \times \frac{e_{\kappa_1 \mu_1}(q_1) e_{\kappa_2 \mu_2}(q_2) e_{\kappa_3 \mu_3}(q_3)}{\sqrt{m_{\kappa_1} m_{\kappa_2} m_{\kappa_3}}} \times \frac{e^{i(\mathbf{q}_2 \cdot \mathbf{r}_2 + \mathbf{q}_3 \cdot \mathbf{r}_3)}}{\sqrt{\omega_{\mathbf{q}_1 j_1} \omega_{\mathbf{q}_2 j_2} \omega_{\mathbf{q}_3 j_3}}}, \quad (3.270)$$

$$V(q_1, q_2, q_3, q_4) = \frac{1}{N_{\text{cell}}} \left( \frac{\hbar}{2} \right)^2 \sum_{\substack{\kappa_1 \mu_1 \\ l_2 \kappa_2 \mu_2 \\ l_3 \kappa_3 \mu_3 \\ l_4 \kappa_4 \mu_4}} \Phi_{\mu_1 \mu_2 \mu_3 \mu_4}^{0\kappa_1, l_2 \kappa_2, l_3 \kappa_3, l_4 \kappa_4} \times \frac{e_{\kappa_1 \mu_1}(q_1) e_{\kappa_2 \mu_2}(q_2) e_{\kappa_3 \mu_3}(q_3) e_{\kappa_4 \mu_4}(q_4)}{\sqrt{m_{\kappa_1} m_{\kappa_2} m_{\kappa_3} m_{\kappa_4}}} \times \frac{e^{i(\mathbf{q}_2 \cdot \mathbf{r}_2 + \mathbf{q}_3 \cdot \mathbf{r}_3 + \mathbf{q}_4 \cdot \mathbf{r}_4)}}{\sqrt{\omega_{\mathbf{q}_1 j_1} \omega_{\mathbf{q}_2 j_2} \omega_{\mathbf{q}_3 j_3} \omega_{\mathbf{q}_4 j_4}}}, \quad (3.271)$$

where  $\mu$  is a Cartesian index,  $l$  is the index of unit cells,  $\mathbf{r}_l$  is the position of the  $l$ th primitive cell, and  $\Phi$  represents the third- and fourth-order IFCs defined in Eq. (3.8)

$$\Phi_{\mu_1 \dots \mu_n}^{l_1 \kappa_1, \dots, l_n \kappa_n} = \Phi_{\mu_1 \dots \mu_n}(l_1 \kappa_1, \dots, l_n \kappa_n), \quad (3.272)$$

where we introduce a new notation to shorten the description. The tadpole and loop diagrams are real constants, while the bubble and 4ph diagrams are complex numbers that depend on the frequency. Thus, only the bubble and 4ph diagrams contribute to phonon linewidths.

### 3.8 Self-Consistent Phonon Theory

Calculations based on perturbation theory only apply when the anharmonic term is sufficiently small. When the anharmonic term is large, it is necessary to calculate the self-energy in a self-consistent manner. SCPH theory is one theory that makes this possible. The SCPH theory assumes the existence of an effective one-body Hamiltonian

$$H^S = \sum_q \omega_q^S \left( b_q^\dagger b_q + \frac{1}{2} \right), \quad (3.273)$$

which incorporates the effects of anharmonic terms and determines it from self-energies.  $\omega_q^S$  are renormalized phonon frequencies called SCPH frequencies. The starting point is the Dyson equation considering the

tadpole and loop diagrams, which are frequency independent.

$$[G_q(\omega)]^{-1} = [G_q^0(\omega)]^{-1} - \Sigma[G] \quad (3.274)$$

$$\Sigma[G] = \Sigma^T[G] + \Sigma^L[G] \quad (3.275)$$

In the SCPH approach, we approximate anharmonic Green's function as

$$G_q^S(\omega) = \frac{2\omega_q^S}{(\omega_q^S)^2 - (\omega)^2}. \quad (3.276)$$

Since the left-hand side of Eq. (3.274) becomes zero at  $\omega_q^S$ , finding the solution  $\omega_q^S$  is equivalent to solving the following equation:

$$\det \left[ [G_q^0(\omega)]^{-1} - \Sigma[G^S] \right] = 0. \quad (3.277)$$

We note that  $\Sigma$  depends on  $G^S$ . Looking at Eq. (3.266) to (3.269),  $\Sigma$  depends on the phonon frequencies and eigenvectors, which are replaced by the SCPH phonon frequencies and eigenvectors. Defining a new diagonal matrix

$$\Lambda_{\mathbf{q}jj'} = 2\omega_{\mathbf{q}j}\delta_{jj'}, \quad (3.278)$$

and multiplying  $\det |\Lambda_{\mathbf{q}}^{1/2}|$  from the left and right of Eq. (3.277), we obtain the following SCPH equation:

$$\det \left[ (\omega_q^S)^2 - V_{\mathbf{q}}(\omega_q^S) \right] = 0 \quad (3.279)$$

$$V_{\mathbf{q}jj'}(\omega) = \omega_{\mathbf{q}j}^2\delta_{jj'} - 2\sqrt{\omega_{\mathbf{q}j}\omega_{\mathbf{q}j'}}\Sigma[G^S]. \quad (3.280)$$

This equation needs to be solved self-consistently. If we only consider the loop diagram and neglect the off-diagonal elements of self-energies, the above SCPH equations can be simplified to the diagonal form:

$$\Omega_q^2 = \omega_q^2 + 2\Omega_q I_q \quad (3.281)$$

$$I_q = \frac{1}{2} \sum_{q_1} \frac{\hbar V(q, -q, q_1, -q_1)}{4\Omega_q \Omega_{q_1}} [1 + 2n(\Omega_{q_1})] \quad (3.282)$$

Although the SCPH theory can treat the tadpole and loop self-consistently, the bubble diagram is also of the same order and often has a magnitude similar to these diagrams. As a result, the SCPH theory has been known to often overestimate phonon frequencies. The SCPH+bubble (SCPH+B) theory [36] has recently been proposed to consider  $\Sigma^B$  in the SCPH theory. After solving the SCPH equation in Eq. (3.274), this method solves the following non-linear equation for  $\Omega$ ,

$$\Omega_q^2 = (\omega_q^S)^2 - 2\omega_q^S \text{Re} \Sigma_q^B[G^S, \Phi_3](\omega = \Omega_q). \quad (3.283)$$

In this thesis, we write the SCPH+B phonon frequencies as  $\Omega^{\text{SCPH+B}}$ .

## 3.9 Dielectric Function

### 3.9.1 Cowley's formula

The dielectric function can be described by the linear response theory with respect to an electric field. The interactive Hamiltonian with an external electric field  $\mathbf{E}(t) = \mathbf{E}_0 e^{-i\omega t + \delta t}$  and the system is described by

$$H_I = -\mathbf{M} \cdot \mathbf{E}(t), \quad (3.284)$$

where  $\mathbf{M}$  is the dipole moment operator of the system. According to the linear response theory, the expectation value of the polarization  $\mathbf{P} = \mathbf{M}/V_0$  of the system is described by the retarded Green's function of the dipole moment operator

$$\bar{P}_\alpha(t) = \frac{1}{V_0} G^R(M_\alpha, \mathbf{M}, \omega) \cdot \mathbf{E}(t), \quad (3.285)$$

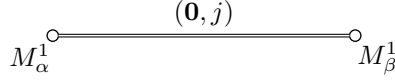


Fig. 3.3: The lowest order of the dielectric function. The double line represents the full-phonon Green's function.

where  $V_0$  is the volume of the supercell. Using the relation between the dielectric susceptibility  $\chi$  and the electric field as  $P_\alpha = \chi_{\alpha\beta} \varepsilon_0 E_\beta$ , the susceptibility is given by

$$\chi_{\alpha\beta} = \frac{1}{V_0} G^R(M_\alpha, M_\beta, \omega). \quad (3.286)$$

Noting that the total dielectric function  $\varepsilon$  in the IR region is the sum of the phonon contribution  $\chi$  and the electron contribution  $\varepsilon^\infty$  as  $\varepsilon_{\alpha\beta} = \varepsilon_{\alpha\beta}^\infty + \chi_{\alpha\beta}$ , the dielectric function can be written as

$$\varepsilon_{\alpha\beta}(\omega) = \varepsilon_{\alpha\beta}^\infty + \frac{1}{V_0} G^R(M_\alpha, M_\beta, \omega). \quad (3.287)$$

Let us consider the expression Eq. (3.164) for the dipole moment by the phonon operator:

$$\mathbf{M}_n = \frac{N_{\text{cell}}}{n!} \left( \frac{\hbar}{2N_{\text{cell}}} \right)^{n/2} \sum_{q_1, \dots, q_n} \Delta(\mathbf{q}_1 + \dots + \mathbf{q}_n) \times \frac{\mathbf{M}(q_1, \dots, q_n)}{\sqrt{\omega_{q_1} \dots \omega_{q_n}}} A_{q_1} \dots A_{q_n}. \quad (3.288)$$

The coefficients  $\mathbf{M}(q_1, \dots, q_n)$  are defined in Eq. (3.122)

$$\begin{aligned} \mathbf{M}(q_1, \dots, q_n) &= \sum_{\kappa_1 \mu_1} \dots \sum_{l_n \kappa_n \mu_n} \mathbf{M}_{\mu_1 \dots \mu_n}^{0\kappa_1, l_2 \kappa_2, \dots, l_n \kappa_n} \\ &\times \frac{1}{\sqrt{m_{\kappa_1} \dots m_{\kappa_n}}} e_{\mu_1}(q_1, \kappa_1) \dots e_{\mu_n}(q_n, \kappa_n) \\ &\times \exp(i(\mathbf{q}_2 \cdot \mathbf{r}_{l_2} + \dots + \mathbf{q}_n \cdot \mathbf{r}_{l_n})). \end{aligned} \quad (3.289)$$

The  $n$ th order terms contain  $n$  phonon operators, and thus Eq. (3.287) is also decomposable by the Bloch-De Dominics theorem. Substituting the  $n = 1$  term

$$\mathbf{M}_1 = \left( \frac{\hbar N_{\text{cell}}}{2} \right)^{1/2} \sum_j \frac{\mathbf{M}(\mathbf{0}j)}{\sqrt{\omega_{\mathbf{0}j}}} A_{\mathbf{0}j} \quad (3.290)$$

$$\mathbf{M}(q_1) = \sum_{\kappa_1 \mu_1} \mathbf{M}_{\mu_1}^{0\kappa_1} \frac{1}{\sqrt{m_{\kappa_1}}} e_{\mu_1}(q_1, \kappa_1) \quad (3.291)$$

into both  $M_\alpha$  and  $M_\beta$  in Eq. (3.287), we have the lowest order contribution of the dielectric function, as shown in Fig. 3.3,

$$\begin{aligned} \varepsilon_{\alpha\beta}(\omega) &= \varepsilon_{\alpha\beta}^\infty + \frac{1}{V_0} \sum_{jj'} \frac{\hbar N_{\text{cell}}}{2} \frac{\mathbf{M}(\mathbf{0}j) \mathbf{M}(\mathbf{0}j')}{\sqrt{\omega_{\mathbf{0}j} \omega_{\mathbf{0}j'}}} G^R(A_{\mathbf{0}j}, A_{\mathbf{0}j'}, \omega) \\ &= \varepsilon_{\alpha\beta}^\infty + \frac{1}{v_0} \sum_{(\mathbf{0}, j)} \frac{S_{\alpha\beta}^j}{(\omega_{\mathbf{0}j})^2 - \omega^2 - 2\omega_{\mathbf{0}j} \Sigma_{\mathbf{0}j}(\omega)}. \end{aligned} \quad (3.292)$$

where  $v_0 = V_0/N_{\text{cell}}$  is the volume of the unitcell.  $S_{\alpha\beta}^j$  is called mode-oscillator strength defined as follows [9],

$$S_{\alpha\beta}^j = \left( \sum_{\kappa\alpha'} Z_{\kappa, \alpha\alpha'}^* \frac{e_{\kappa\alpha'}(\mathbf{0}j)}{\sqrt{m_\kappa}} \right) \left( \sum_{\kappa\beta'} Z_{\kappa, \beta\beta'}^* \frac{e_{\kappa\beta'}(\mathbf{0}j)}{\sqrt{m_\kappa}} \right), \quad (3.293)$$

where  $Z^*$  is a Born effective charge. We note that summations in Eq. (3.292) are taken only for TO phonons at the  $\Gamma$  point.

Table 3.1: Treatment of the four diagrams in this thesis.

|                      | Tadpole   | Loop | Bubble | 4ph                      |                          |
|----------------------|-----------|------|--------|--------------------------|--------------------------|
| Imaginary            | ×         | ×    | ○      | ○                        |                          |
| Frequency-dependence | ×         | ×    | ○      | ○                        |                          |
| Treatment            | Real      | SCPH | SCPH   | SCPH+B                   | Perturbation Eq. (3.294) |
|                      | Imaginary | -    | -      | Perturbation Eq. (3.294) | Perturbation Eq. (3.294) |

### 3.9.2 Dielectric function from SCPH+B

Combining the theory of dielectric functions described in Sec. 3.9.1 and the theory of SCPH+B described in Sec. 3.8, we propose a method for calculating dielectric functions in the case of strong anharmonicity. Evaluating the dielectric function of Eq. (3.292) after calculating the self-energy using the usual perturbation theory gives incorrect results when anharmonicity is strong. Therefore, by evaluating the self-energy on the basis of the effective Hamiltonian obtained by SCPH+B, the dielectric function can be calculated in a way that includes the frequency renormalization effect of SCPH+B. Similar methods are widely used in heat conduction calculations [28, 29].

After obtaining the anharmonic phonon frequencies and eigenvectors from the SCPH+B equation, the imaginary part of  $\Sigma^B$  and  $\Sigma^{4ph}$  are considered in a frequency-dependent form as

$$\Sigma^{B+4ph}(\omega) = \text{Im} \Sigma^B[G^{\text{SCPH+B}}, \Phi_3](\omega) + \text{Im} \Sigma^{4ph}[G^{\text{SCPH+B}}, \Phi_4](\omega). \quad (3.294)$$

Here, we do not use harmonic Green's functions for evaluating self-energies but use SCPH+B Green's functions to include the phonon frequencies renormalization effect, of which importance has been pointed out in previous studies [29, 127]. The treatment of the four diagrams is summarized in Table 3.1.

After evaluating all four diagrams, we finally obtain a dielectric function by substituting these self-energies into Eq. (1.32) as

$$\varepsilon_{\alpha\beta}(\omega) = \varepsilon_{\alpha\beta}^{\infty} + \frac{1}{v_0} \sum_j \frac{S_{\alpha\beta}^j}{(\Omega_{0j}^{\text{SCPH+B}})^2 - \omega^2 - 2\Omega_{0j}^{\text{SCPH+B}} \Sigma^{B+4ph}(\omega)}, \quad (3.295)$$

where the mode-oscillator strength is also evaluated on the SCPH+B eigenvectors. The whole procedure to calculate the dielectric function of Eq. (3.295) is illustrated in Fig. 3.4.

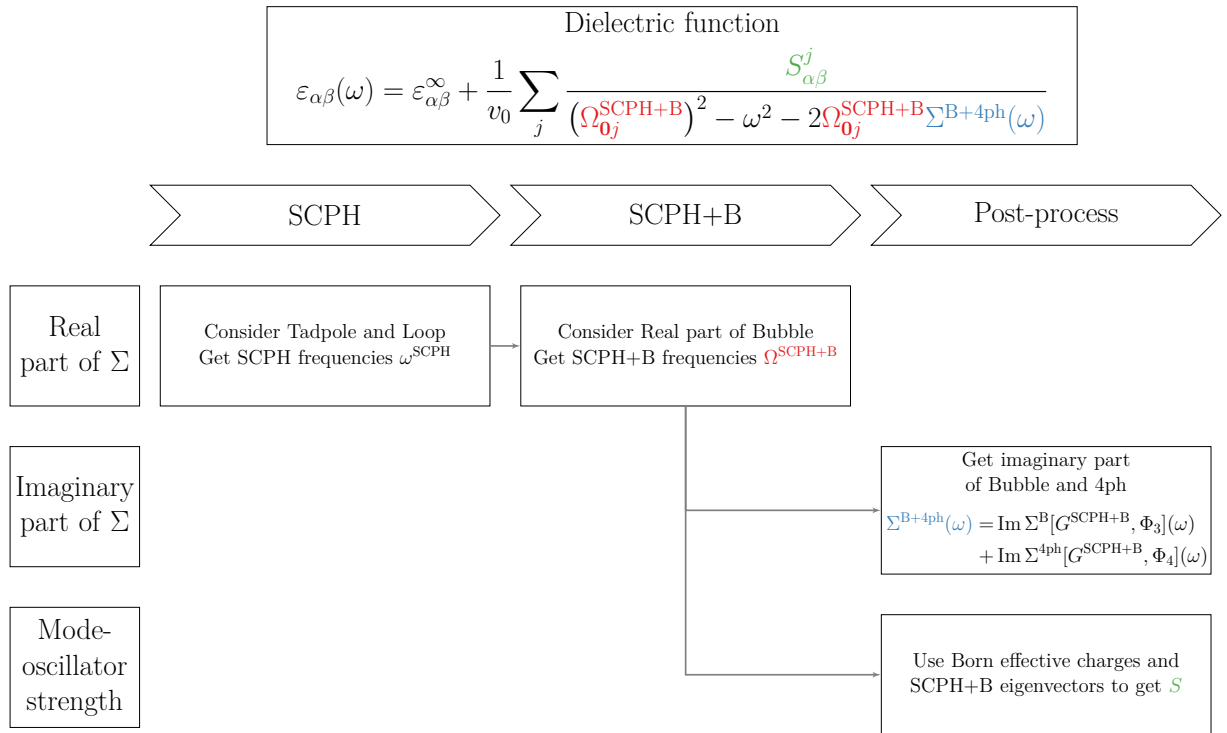


Fig. 3.4: Workflow to calculate the dielectric function of Eq. (3.295).



## Chapter 4

# Modern Theory and Machine Learning of Polarization

This chapter is not disclosed because it will be published in a journal within 5 years.



## Chapter 5

# Dielectric Properties of Strongly Anharmonic TiO<sub>2</sub>

In this chapter, we study the lattice dielectric properties of strongly anharmonic rutile TiO<sub>2</sub> from *ab initio* anharmonic lattice dynamics methods. We employ the modified self-consistent approach, including third-order anharmonicity as well as fourth-order anharmonicity to calculate the  $\Gamma$  point phonons as accurate as possible for determining optical properties. The resulting optical phonon frequencies and linewidths at the  $\Gamma$  point much better coincide with experimental values than those from a perturbative approach. We show that the four-phonon scattering process contributes as much as the third-order anharmonic term to phonon linewidths of some phonon modes. Furthermore, the frequency dependence of phonon linewidth reveals that experimentally known but unidentified peaks of the dielectric function are ascribed to two-phonon process. These calculations underscore the importance of the self-consistent approach in predicting the optical properties of highly anharmonic materials. The part of this chapter was published in Ref. [146].

### 5.1 Introduction

As a polar semiconductor, titanium dioxide (TiO<sub>2</sub>) has garnered interest due to its extraordinary dielectric constants of 111 and 250 along the  $x$  and  $z$  axes at room temperature, respectively. The resulting high refractive index benefits a number of technical applications, including pigments, capacitors, and high- $\kappa$  dielectric materials for DRAM [1]. Other applications include solar cells and lithium ion batteries.

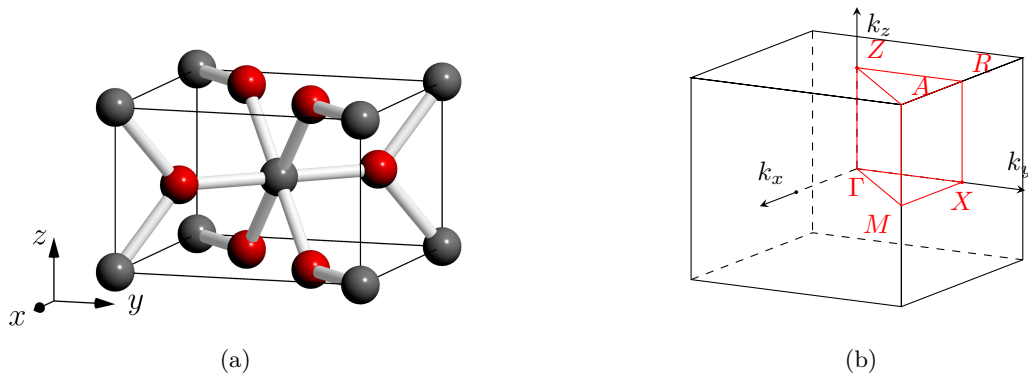


Fig. 5.1: (a) The crystal structure of rutile TiO<sub>2</sub>, which contains two titanium atoms (black) and four oxygen atoms (red). The lattice parameters for  $x$  and  $y$  axis are the same, while that of  $z$  axis is shorter. (b) The first Brillouin zone and its high-symmetry points including  $Z(0, 0, 0.5)$  (reduced coordinates),  $A(0.5, 0.5, 0.5)$ ,  $M(0.5, 0.5, 0)$ ,  $R(0, 0.5, 0.5)$ , and  $X(0, 0.5, 0)$

Figure 5.1 illustrates the tetragonal unit cell of rutile TiO<sub>2</sub> with the  $P4_2/mnm$  space group. The presence of six atoms in the unit cell leads to 15 optical phonon modes and three acoustic phonon modes. The  $\Gamma$  point (the center of the Brillouin zone) optical phonons correspond to the following irreducible representations,

$$\Gamma_{\text{opt}} = A_{1g} + A_{2g} + A_{2u} + 2B_{1u} + B_{1g} + B_{2g} + E_g + 3E_u. \quad (5.1)$$

Subscript g and u (except for  $B_{1u}$ ) mean Raman-active and infrared-active, respectively. The  $E$  symbol expresses degeneracy. We analyse IR active three  $E_u$  and  $A_{2u}$  modes. As shown in Fig. 5.2,  $E_u$  is the vibration in the  $xy$ -direction and  $A_{2u}$  in the  $z$  direction. Therefore, they contribute to the  $xy$  and  $z$  components of the dielectric function. The Ti and O ions move in opposite directions in the  $E_u^1$  phonon, the softest  $E_u$

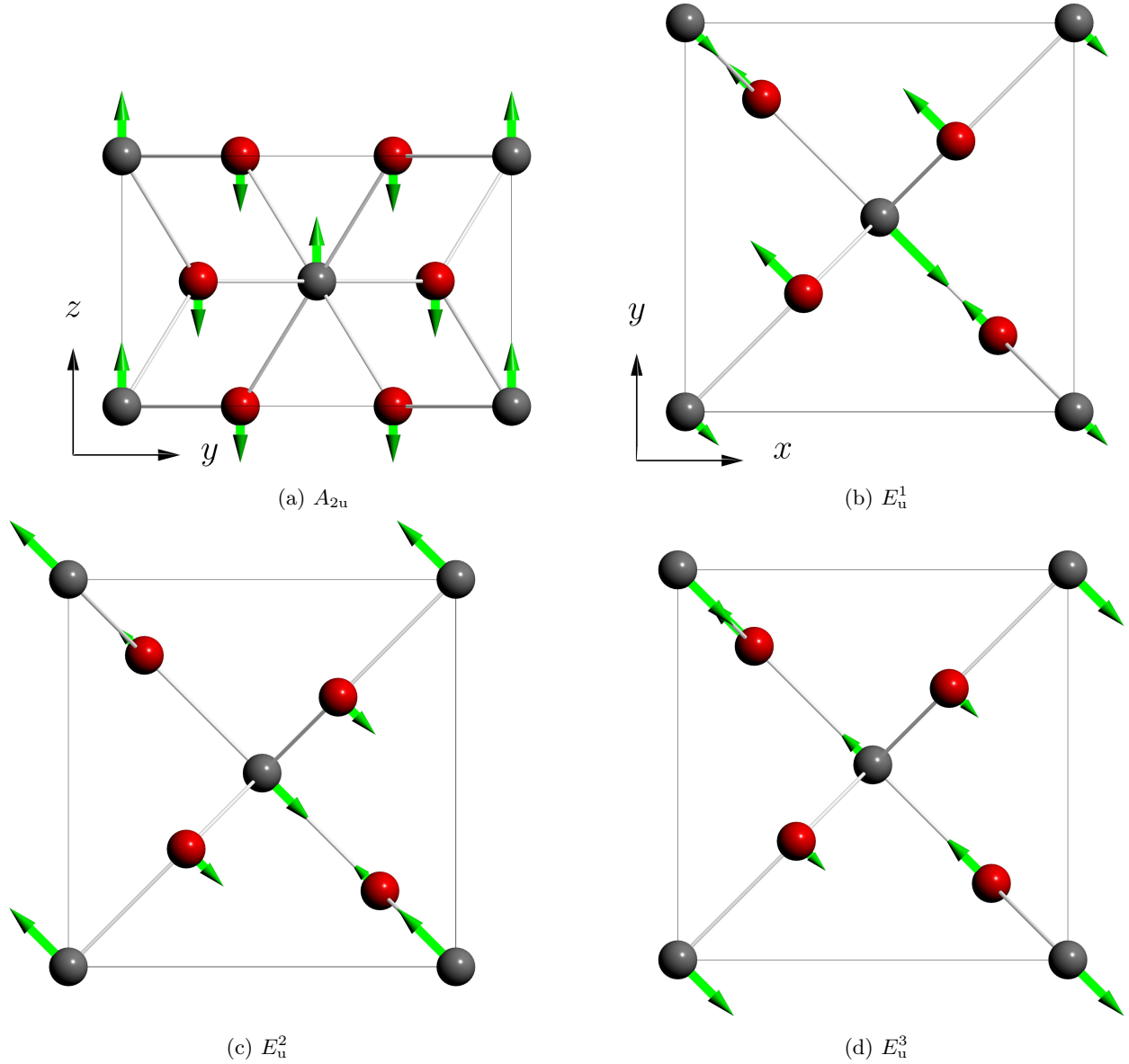


Fig. 5.2: (a-d) Schematic views of atomic displacements for the  $A_{2u}$  mode and the three  $E_u$  modes.

phonon, and the  $A_{2u}$  phonon; in contrast, the two Ti ions move in opposite directions in the  $E_u^2$  and  $E_u^3$  modes. Due to the giant Born effective charges, the IR active phonons at the  $\Gamma$  point show significant LO-TO splitting, with the LO  $A_{2u}$  phonon frequency reaching  $811\text{ cm}^{-1}$  compared to the TO  $A_{2u}$  phonon frequency of  $167\text{ cm}^{-1}$  [147].

The importance of rutile  $\text{TiO}_2$  has instigated several experimental and theoretical studies on dielectric properties [6, 148–156]. Significant Born effective charges and a low-frequency transverse optical phonon mode ( $A_{2u}$ , see Fig. 5.2) are directly responsible for the enormous dielectric constant. The frequency of the  $A_{2u}$  phonon rapidly increases with increasing temperature [157], resulting in a drop in the static dielectric constant. However, unlike ferroelectric crystals, the frequency of the  $A_{2u}$  phonon does not become zero with lowering temperature, and therefore the system does not undergo a phase transition, which is called incipient ferroelectric. Such significant temperature dependence is due to the strong anharmonicity of the lattice [152]. Gervais and Piriou [6, 153, 158] applied the four-parameter semi-quantum model (FPSQ) as a model of the dielectric function, which partially accounts for anharmonic effects employing different damping parameters for each TO and LO phonon, and successfully fitted experimental reflectivity data. The FPSQ model studies [6, 153–155] showed a marked difference in damping parameters between each LO and TO phonon, indicating that the conventional harmonic vibration model breaks down, especially for the  $A_{2u}$  phonon mode.

The first *ab initio* study on the lattice dynamics of rutile  $\text{TiO}_2$  by Lee et al. [159] successfully calculated

large Born effective charges and static dielectric constant, which led to a lot of DFT studies on harmonic phonon properties of rutile  $\text{TiO}_2$  [160–168]. As in other oxides [2, 169], large polarizability due to long-range Coulomb interactions causes the mixing of covalent and ionic bonding of  $s$  orbitals of oxygen and  $d$  orbitals of titanium. The huge Born effective charges could be caused by the dynamical transfer of electrons of associated with atomic displacements [170]. Regarding lattice dynamics, the frequencies of the  $A_{2u}$  and TA phonons show significant strain dependencies [162, 164, 167]. The generalized gradient approximation (GGA) of Perdew-Burke-Ernzerhof yields imaginary phonon frequency [161] of the  $A_{2u}$  mode, due to a well known overestimation of the lattice constants. These results indicate that the lattice dynamical properties are sensitive to exchange-correlation functionals and pseudopotentials [165]. While LDA functionals have been successful in describing lattice dynamics despite the underestimation of the lattice constants, meta-GGA and hybrid functionals yield more accurate lattice constants [165, 168].

Recently, an *ab initio* computational framework of phonon anharmonicity is used to analyze the thermal conductivity of rutile  $\text{TiO}_2$  [127, 171]. Fu et al. [127] found that the finite-temperature effective IFCs [27], effectively including higher order anharmonicity, are essential for predicting thermal conductivity, whereas calculations only including third-order anharmonicity underestimated the thermal conductivity. This finding implies that the lattice properties of rutile  $\text{TiO}_2$  can be explained by incorporating higher-order IFCs. In particular, the anharmonicity of the  $A_{2u}$  mode reaches as high as 20% [6, 153], and the legitimacy of perturbative approaches taken in previous studies is questionable. The self-consistent phonon (SCPH) theory [28, 29] can apply to such highly anharmonic materials incorporating fourth-order anharmonicity in a self-consistent manner. Recently, the SCPH+B theory has been developed to include the frequency shift associated with third-order anharmonicity within a quasiparticle approximation [36]. It could describe the possible cancellation of frequency shifts of third and fourth-order anharmonicity in the  $A_{2u}$  phonon.

In this chapter, we studied the IR optical properties of highly anharmonic rutile  $\text{TiO}_2$  using first-principles lattice dynamics calculations. We extracted IFCs using the least absolute shrinkage and selection operator (LASSO) technique from first-principles calculations. Renormalized anharmonic phonon frequencies were calculated using SCPH+B, with which frequency-dependent phonon linewidths were estimated. The dielectric was calculated from the Cowley formula. We found that the  $r^2\text{SCAN}$  functional reproduces experimental values and that a self-consistent method is essential for describing the strong anharmonicity of the rutile  $\text{TiO}_2$ .

## 5.2 Four Parameter Semi-Quantum Model

In polar semiconductors and insulators, the long range Coulomb forces invoke macroscopic electric fields for LO phonons in the long-wavelength limit to increase phonon energies. Since the Coulomb forces are described by the Born effective charges, the LO-TO splitting is generally larger when the Born effective charges are larger [9, 12, 172].

The four parameter semi-quantum (FPSQ) model, which has four parameters per each IR active phonon mode, is a useful phenomenological model when the LO-TO splitting is large. According to the Maxwell's equations, the poles of a dielectric function are TO phonon frequencies, and the poles of an extinction coefficient  $\eta = 1/\varepsilon$  are LO phonon frequencies. The FPSQ model have different phonon frequencies and dampings for LO and TO phonons as

$$\varepsilon(\omega) = \varepsilon^\infty \prod_j \frac{\omega_{0j,\text{LO}}^2 - \omega^2 + i\omega\gamma_{0j,\text{LO}}}{\omega_{0j,\text{TO}}^2 - \omega^2 + i\omega\gamma_{0j,\text{TO}}}. \quad (5.2)$$

The difference in a damping is more noticeable when LO-TO splitting is substantial, that is,  $\omega_{\text{LO}} \gg \omega_{\text{TO}}$ , and the FPSQ model is more appropriate than the Lorentz model. For a wide variety of materials, the model successfully explains the experimental findings, despite without taking the frequency dependence of damping into account.

## 5.3 Results and Discussion

### 5.3.1 Computational details

The IFCs of rutile  $\text{TiO}_2$  were calculated from *ab initio* calculations using VASP [177]. As mentioned in Sec. 5.1, the choice of functional and pseudopotential is essential for accurate phonon property calculations of this material. The local density approximation (LDA) [178], the PBEsol functional [179], and the  $r^2$  strongly constrained and appropriately normed ( $r^2\text{SCAN}$ ) meta-GGA [180] with the projector augmented-wave method [181] were used for exchange and correlation functionals. These functionals were chosen because

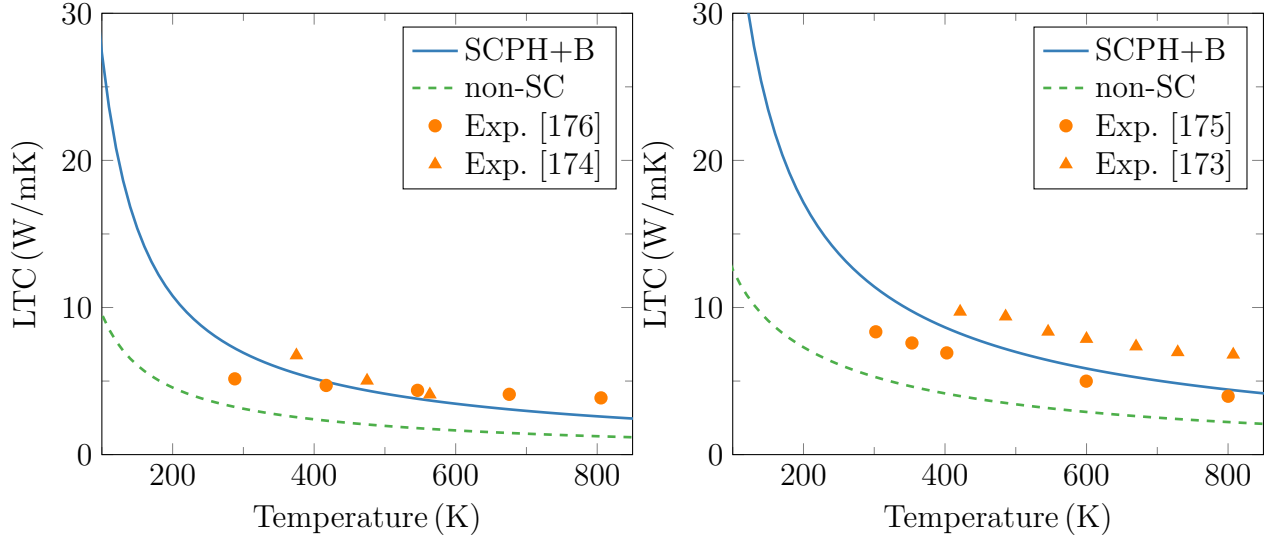


Fig. 5.3: Calculated  $x$ -axis and  $z$ -axis LTC from 100 K to 850 K. The measurements are from Charvat and Kingery [173], Yoshida [174], Touloukian [175], and Ok et al. [176]

LDA has long been used successfully in rutile TiO<sub>2</sub>, and r<sup>2</sup>SCAN is known from its good description for phonon properties. PBEsol was used to validate these two functionals. The semicore  $3s$  and  $3p$  states are considered as the valence electrons in the Ti pseudopotential, of which importance was reported in several studies [164]. The plane-wave energy and charge cutoffs are 800 eV and 1200 eV, respectively, with the energy convergence threshold set at  $1 \times 10^{-9}$  eV.

We first performed the lattice parameter and geometry optimization with the electronic sampling of a  $10 \times 10 \times 10$  Monkhorst-Pack grid, which converged to the maximum error in forces of 1 meV/Å and stresses of 0.01 GPa. Born effective charges are obtained from DFPT calculations for both long-range interactions and dielectric properties.

We estimated IFCs via linear-regression optimization using DFT forces of various atomic configurations as training data. The atomic forces were calculated building a  $2 \times 2 \times 4$  supercell to make the supercell as close to cubic as possible, with a  $5 \times 5 \times 5$  electronic wave vector grid. The least square fitting was employed for the harmonic terms, the number of which is 217 in our case, combined with the finite displacement method with one atom moved by 0.01 Å. For rutile TiO<sub>2</sub>, there were five independent displacement patterns, and calculations were performed for each case by moving the atoms in positive and negative directions. Next, we employed the LASSO method [182] to extract anharmonic IFCs from the 100 displacement-force training datasets, where all atoms are randomly moved 0.04 Å from the equilibrium position. We incorporated all feasible IFCs in a  $2 \times 2 \times 4$  supercell for harmonic IFCs. Cutoffs of 15, 10, 5, and 5 bohr were applied to the cubic, quartic, fifth, and sixth terms, respectively. The hyperparameters of LASSO were determined by 4-fold cross validation. During the fitting of anharmonic terms, we fixed the harmonic IFSs to the values determined by the finite-displacement approach. The fitting error for the harmonic approximation and the anharmonic terms were about 1% and 0.3%, respectively.

The SCPH and SCPH+B equations were solved using a  $2 \times 2 \times 2$   $q$  points grid, where a  $6 \times 6 \times 6$   $q$  points mesh was used for computing the self-energies [28].  $\Sigma^T$  is small enough in rutile TiO<sub>2</sub> for us to ignore it. Finally, we used a  $15 \times 15 \times 15$  and  $10 \times 10 \times 10$   $q$  points grid to calculate the imaginary parts of  $\Sigma^B$  and  $\Sigma^{4ph}$ , respectively. The ALAMODE [25] package was utilized for the extraction of IFCs, the lattice dynamics calculations, and the SCPH calculations.

To verify our anharmonic lattice model, we performed the lattice thermal conductivity (LTC) calculations with the Boltzmann transport equation. In these calculations, we calculated the phonon lifetimes from the bubble diagram using harmonic or 300 K SCPH+B phonons

$$\tau^{\text{SCPH+B}} = \frac{1}{2 \text{Im} \Sigma^B[G^{\text{SCPH+B}}](\omega = \Omega^{\text{SCPH+B}})} \quad (5.3)$$

$$\tau^{\text{non-SC}} = \frac{1}{2 \text{Im} \Sigma^B[G^{\text{harm}}](\omega = \omega^{\text{harm}})}. \quad (5.4)$$

Figure 5.3 depicts the LTC for the  $x$  and  $z$  directions with experimental values [173, 174, 176]. As pointed

out by Fu et al. [127], the LTC is greatly underestimated when phonon lifetimes are calculated using harmonic phonon frequencies, which indicates that the phonon lifetimes are overestimated. On the other hand, calculations using SCPH+B phonons generally agree well with experimental data, and we conclude that our anharmonic lattice model is reliable.

All the parameters in Eq. (3.295) will be determined if second, third, and fourth-order IFCs are provided other than  $\varepsilon^\infty$  and  $Z^*$ , which can be calculated from DFPT. As  $\varepsilon^\infty$  is well known to be overestimated in DFT and the evaluation of  $\varepsilon^\infty$  is outside the scope of our work, we use the experimental values [148] of  $\varepsilon_{xx}^\infty = 5.91$  and  $\varepsilon_{zz}^\infty = 7.20$  in the following calculations. It should be mentioned that the  $\varepsilon^\infty$  was evaluated using the FPSQ model and several values have been reported [6, 154, 155].

Table 5.1: Calculated lattice constants with LDA and r<sup>2</sup>SCAN. Experimental values are taken from a neutron diffraction study [183].  $a$  is the lattice constant in the  $x$  and  $y$  directions, and  $c$  in the  $z$  direction.  $v_0$  is the lattice volume. The four oxygen O ions are located at the  $(u, u, 0)$ ,  $(1 - u, 1 - u, 0)$ ,  $(1/2 - u, 1/2 + u, 1/2)$ , and  $(1/2 + u, 1/2 - u, 1/2)$  in the fractional coordinate, where  $u$  is a parameter.

|                     | $a$ (Å) | $c$ (Å) | $u$    | $c/a$ | $v_0$ (Å <sup>3</sup> ) |
|---------------------|---------|---------|--------|-------|-------------------------|
| LDA                 | 4.552   | 2.922   | 0.3038 | 0.642 | 60.55                   |
| PBEsol              | 4.595   | 2.942   | 0.3044 | 0.640 | 62.12                   |
| r <sup>2</sup> SCAN | 4.602   | 2.961   | 0.3046 | 0.643 | 62.71                   |
| Exp. 300 K [183]    | 4.593   | 2.959   | 0.3048 | 0.644 | 62.42                   |
| Exp. 15 K [183]     | 4.587   | 2.954   | 0.3047 | 0.644 | 62.15                   |

Table 5.2: Calculated Born effective charge tensors  $Z$  of the Ti atom at  $(0, 0, 0)$  and the O atom at  $(u, u, 0)$ .

|                     | Ti       |          |          | O        |          |          |
|---------------------|----------|----------|----------|----------|----------|----------|
|                     | $Z_{xx}$ | $Z_{xy}$ | $Z_{zz}$ | $Z_{xx}$ | $Z_{xy}$ | $Z_{zz}$ |
| LDA                 | 6.34     | -1.01    | 7.66     | -3.17    | 1.81     | -3.83    |
| PBEsol              | 4.95     | -1.13    | 7.66     | -2.48    | 1.80     | -3.83    |
| r <sup>2</sup> SCAN | 5.96     | -0.97    | 7.27     | -2.94    | 1.71     | -3.60    |

### 5.3.2 Phonon frequencies

We first present results for optimized lattice constants from LDA, PBEsol, and r<sup>2</sup>SCAN compared with experimental values at 15 K and 295 K in Table 5.1. As in previous studies, LDA slightly underestimates the lattice constants by 0.8%, while the PBEsol functional shows good agreement with the experimental values. The r<sup>2</sup>SCAN functional, a meta-GGA family, reproduces the experimental values within 0.4%, though the GGA-PBE functional is known to overestimate the lattice constants.

We next offer results for Born effective charges from LDA, PBEsol, and r<sup>2</sup>SCAN. When calculating the Born effective charges, the value is adjusted by the average value of  $Z^*$  to satisfy the acoustic sum rule [9] as

$$\bar{Z}_{\kappa, \alpha\beta}^* = Z_{\kappa, \alpha\beta}^* - \frac{1}{N} \sum_{\kappa} Z_{\kappa, \alpha\beta}, \quad (5.5)$$

where  $N$  is the number of atoms in the unitcell. In the case of rutile TiO<sub>2</sub>, Born effective charges have three non-zero components  $Z_{xx}$ ,  $Z_{xy} = Z_{yz}$  and  $Z_{zz}$  which are independent from the local atomic symmetry. Table 5.2 shows that Born effective charges obtained from r<sup>2</sup>SCAN are around 10% smaller than those from LDA. The LDA values agree well with those of previous LDA studies [159, 165, 170, 186]. The major feature is that the absolute value of Born effective charges is larger than the ionic charges of +4 for Ti and -2 for O, which results from the covalent character of the Ti-O bonds. Based on the LO phonon frequencies results discussed below, Born effective charges calculated from r<sup>2</sup>SCAN are considered more accurate than those from LDA.

Figure 5.4 shows the phonon dispersion spectrum along the high-symmetry points in the first Brillouin zone at 300 K with non-analytic term correction (See also Fig. 5.1). The r<sup>2</sup>SCAN results are displayed in

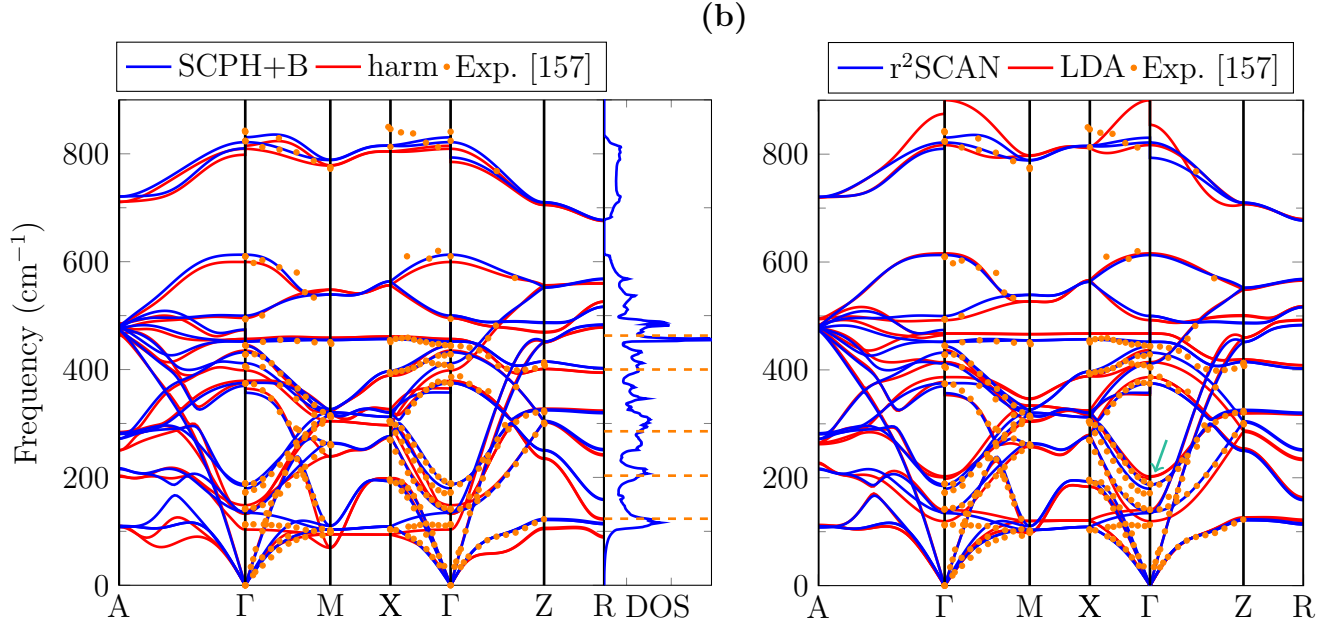


Fig. 5.4: (a) The harmonic (red) and SCPH+B (blue) band structures of  $r^2\text{SCAN}$  functional at 300 K with the experimental values from inelastic neutron scattering (orange dot) [157]. The SCPH+B DOS is also illustrated at the same time. The orange dashed lines are the peak obtained from the inelastic neutron scattering experiment [184]. (b) The SCPH+B band structure with  $r^2\text{SCAN}$  (blue) and LDA (red) functional. The green arrow indicate the  $A_{2u}$  mode, which is overestimated in the LDA functional.

Figure 5.4a, where harmonic phonon frequencies (red, abbreviated as harm) are compared with SCPH+B frequencies (blue). Figure 5.4b compares the SCPH+B frequencies using LDA (red) and  $r^2\text{SCAN}$  (blue), together with inelastic neutron scattering results from Traylor [157] (orange dots). Figure 5.4a also shows the density of states (DOS) of  $r^2\text{SCAN}$  and SCPH+B, with the orange dashed lines being the positions of the five DOS peaks observed in the neutron experiment by Lan and Fultz [187]. Overall, the combination of the  $r^2\text{SCAN}$  functional and the SCPH+B calculation agrees well with the experimental values except for the lowest optical phonon branch ( $B_{1u}$ ), which is sensitive to the choice of functionals [164]. The frequencies of the  $\Gamma$  point  $A_{2u}$  and  $E_u^1$  phonons and the TA phonon branch, considered highly anharmonic in previous studies, are underestimated in the harmonic approximation, while the SCPH+B calculation yields good reproduction of experiments. Figure 5.5 shows the potential energy surface of the  $A_{2u}$  phonon is no longer a quadratic function and is well reproduced with considering functions up to the fourth order. Table 5.3 summarizes the  $\Gamma$  point phonon frequencies with several experiments [147, 155, 157, 185]. For the  $A_{2u}$  and  $E_u^1$  modes, the negative frequency shift by the bubble self-energy counteracts the positive frequency shift by the loop self-energy, resulting in about  $50 \text{ cm}^{-1}$  positive frequency shift. The  $A_{2u}$  phonon frequency is  $139 \text{ cm}^{-1}$  within the harmonic approximation, rises to  $220 \text{ cm}^{-1}$  by SCPH, and decreases to  $179 \text{ cm}^{-1}$  when the bubble self-energy is considered with SCPH+B. The contribution of the anharmonic terms reach 29%. Similarly, the  $E_u^1$  phonon frequency is  $133 \text{ cm}^{-1}$  for the harmonic approximation,  $210 \text{ cm}^{-1}$  for SCPH, and  $189 \text{ cm}^{-1}$  for SCPH+B. We also estimated phonon frequencies from a usual perturbative approach (abbreviated as non-SC) for  $r^2\text{SCAN}$  as  $\omega = \omega_0 + \Delta\omega^T + \Delta\omega^B + \Delta\omega^L$ . The non-SC frequencies differ largely from the SCPH+B frequencies in the  $A_{2u}$  and  $E_u^1$  phonons. In the  $A_{2u}$  phonon mode, we obtained  $\Delta\omega^B = -78 \text{ cm}^{-1}$  and  $\Delta\omega^L = 144 \text{ cm}^{-1}$ , which means that the perturbation theory fails on this mode. We conclude that neither the harmonic approximation nor the perturbation method suffices for optical properties, where an accurate estimation of the optical phonon frequencies at the  $\Gamma$  point is necessary.

Although Fig. 5.4b demonstrates a good agreement between LDA and  $r^2\text{SCAN}$  throughout the Brillouin zone, the LDA calculation overestimates the  $\Gamma$  point  $A_{2u}$  phonon for about  $25 \text{ cm}^{-1}$ . The underestimation of the lattice constants of LDA may cause the overestimation of the  $A_{2u}$  phonon, as the  $A_{2u}$  phonon is sensitive to lattice constants [161]. To clarify this point, we have performed the SCPH+B calculation with LDA using the experimental lattice constants at 300 K shown in Table 5.1. The resultant frequency of the  $A_{2u}$  phonon significantly reduced to  $146 \text{ cm}^{-1}$ , which underestimates the experimental value by 15%. This result shows that the  $A_{2u}$  mode is sensitive to the lattice constant even at the level of anharmonic phonon calculations. For the LO phonons, the LDA results overestimate the  $E_u^3$  and  $A_{2u}$  phonon frequencies, the cause of which is larger Born effective charges by LDA than that by  $r^2\text{SCAN}$ . As  $r^2\text{SCAN}$  gives better results than LDA,

Table 5.3: Comparison of the computed mode frequencies (in  $\text{cm}^{-1}$ ) at the  $\Gamma$  point with various experimental data at room temperature. The results from the harmonic approximation (harm), SCPH and SCPH+B are shown for both LDA and  $r^2\text{SCAN}$  at 300 K, while a usual perturbation calculation (non-SC) are shown only for  $r^2\text{SCAN}$ .

|            | LDA   |       |        | r <sup>2</sup> SCAN |       |        |        | neutron [157]   | Raman [185] | FPSQ [155] |
|------------|-------|-------|--------|---------------------|-------|--------|--------|-----------------|-------------|------------|
|            | harm  | SCPH  | SCPH+B | harm                | SCPH  | SCPH+B | non-SC |                 |             |            |
| IR [147]   |       |       |        |                     |       |        |        |                 |             |            |
| Raman      |       |       |        |                     |       |        |        |                 |             |            |
| $A_{1g}$   | 612.5 | 620.8 | 616.6  | 599.8               | 613.1 | 613.3  | 627.1  | 610             | 612         | -          |
| $A_{2g}$   | 395.0 | 424.0 | 413.7  | 456.5               | 432.9 | 451.8  | 458.9  | NF <sup>1</sup> | NF          | -          |
| $B_{1g}$   | 134.7 | 121.9 | 116.6  | 146.5               | 143.0 | 138.9  | 139.1  | 142             | 143         | -          |
| $B_{2g}$   | 817.5 | 818.2 | 817.2  | 809.6               | 814.4 | 821.8  | 831.4  | 824             | 826         | -          |
| $E_g$      | 464.3 | 476.0 | 467.5  | 434.4               | 463.1 | 431.5  | 429.0  | 445             | 447         | -          |
| non-active |       |       |        |                     |       |        |        |                 |             |            |
| $B_{1u}^1$ | 108.1 | 149.6 | 140.2  | 103.2               | 141.0 | 130.0  | 159.5  | 113             | -           | -          |
| $B_{1u}^2$ | 417.9 | 414.8 | 413.8  | 398.4               | 420.7 | 411.7  | 421.8  | 406             | -           | -          |
| TO         |       |       |        |                     |       |        |        |                 |             |            |
| $A_{2u}$   | 147.8 | 227.9 | 198.0  | 138.5               | 210.1 | 179.4  | 210.6  | 172.6           | 167         | 172.3      |
| $E_u^1$    | 149.0 | 216.8 | 202.0  | 132.7               | 203.6 | 186.9  | 238.4  | 189             | 183         | 188.6      |
| $E_u^2$    | 384.3 | 394.6 | 386.5  | 378.8               | 382.1 | 374.9  | 374.3  | 374             | 388         | 379.3      |
| $E_u^3$    | 489.0 | 504.7 | 492.5  | 495.7               | 513.1 | 500.1  | 495.0  | 494             | 500         | 500.5      |
| LO         |       |       |        |                     |       |        |        |                 |             |            |
| $A_{2u}$   | 843.9 | 861.5 | 854.2  | 784.9               | 800.6 | 793.1  | 805.2  | NF              | 811         | 796.5      |
| $E_u^1$    | 354.6 | 362.7 | 354.0  | 364.5               | 364.9 | 356.9  | 360.0  | 375             | 373         | 365.7      |
| $E_u^2$    | 439.1 | 447.3 | 436.8  | 445.5               | 455.6 | 443.9  | 445.7  | 428             | 458         | 444.9      |
| $E_u^3$    | 882.8 | 904.9 | 904.9  | 815.1               | 836.0 | 830.7  | 851.4  | 842             | 806         | 829.6      |

<sup>1</sup> NF=not found.

all the following calculations are based on  $r^2\text{SCAN}$ .

Finally, we calculated the temperature dependence of the static dielectric constant  $\varepsilon^0 \equiv \varepsilon(\omega = 0)$ ,

$$\varepsilon_{\alpha\beta}^0 = \varepsilon_{\alpha\beta}^\infty + \frac{1}{v_0} \sum_j \frac{S_{\alpha\beta}^j}{(\Omega_{0j}^{\text{SCPH+B}})^2}, \quad (5.6)$$

which directly reflects the effect of the phonon frequency shift with temperature. Figure 5.6 compares the calculated temperature dependence of  $\varepsilon_x^0$  and  $\varepsilon_z^0$  with the experimental data [149]. Both  $\varepsilon_x^0$  and  $\varepsilon_z^0$  increase with lowering temperatures due to a decrease in the phonon frequencies. In particular,  $\varepsilon_z^0$  shows significant increase to 250 at  $T = 0$ . The SCPH+B calculation well reproduced experimental values for  $\varepsilon_x^0$ . On the other hand,  $\varepsilon_z^0$  yields 169 at  $T = 0$  K, which is only 70% of the experimental value. In fact, the frequency of the  $A_{2u}$  mode is  $167 \text{ cm}^{-1}$  at  $T = 0$  K in the SCPH+B calculation, compared to the experimental value of  $140 \text{ cm}^{-1}$  [157], which indicates that the zero-point vibration is very large. This could be improved by using more accurate functionals like hybrid functionals.

### 5.3.3 Results of the PBEsol functional

We have seen that the combination of  $r^2\text{SCAN}$  and SCPH+B agrees very well with experiment, but there are still discrepancies in the phonon frequencies of the  $B_{1u}^1$  modes and the temperature dependence of  $\varepsilon_0^z$ . To

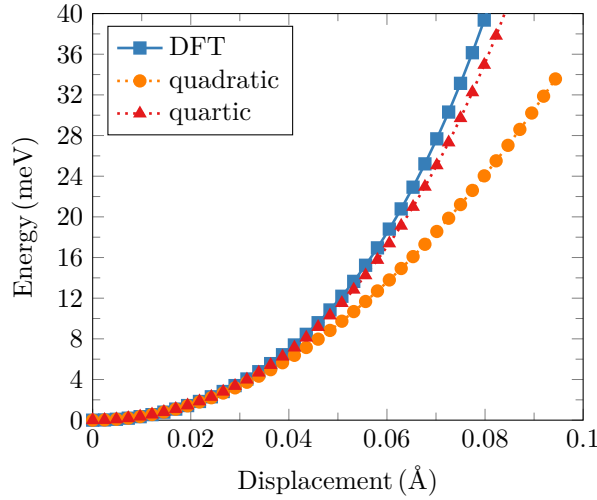


Fig. 5.5: Frozen phonon potential (blue) of  $A_{2u}$  mode with  $x$  axis being the displacement of the Ti atoms. The quartic component (red) describes the DFT potential well, while the harmonic component (orange) deviates from the potential.

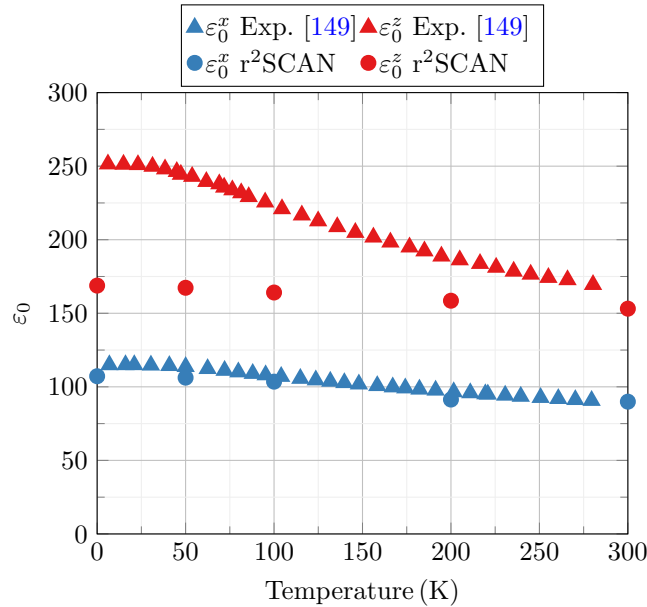


Fig. 5.6: Temperature dependence of the static dielectric constant. The triangular dots show the experimental values and the circular dots show the results from the SCPH+B calculations.

investigate the origin of this discrepancy, we performed similar calculations for the PBEsol functional. The results are summarized in this section. Figure 5.7 shows the phonon dispersion spectrum along the high-symmetry points in the first Brillouin zone at 300 K with non-analytic term correction, together with inelastic neutron scattering results from Traylor [157] (orange dots), while Table 5.4 shows the phonon frequencies at the  $\Gamma$  point. The frequency of the  $B_{1u}^1$  mode is  $121 \text{ cm}^{-1}$ , which is smaller than that of r<sup>2</sup>SCAN and reproduces the experimental value [157] well.

Figure 5.8 shows the temperature-dependent dielectric constants and the SCPH+B phonon frequencies of the  $A_{2u}$  mode from PBEsol, which yielded the  $A_{2u}$  frequency of  $162 \text{ cm}^{-1}$  at 300 K, close to that of r<sup>2</sup>SCAN. Fig. 5.8 shows the temperature dependence of the frequency of the  $A_{2u}$  phonon, where PBEsol is in good agreement with the experiment at low temperatures, while r<sup>2</sup>SCAN overestimates the frequency at low temperatures. As a result, calculated  $\epsilon_0^z$  with PBEsol is in good agreement with the experimental data in Fig. 5.8. From this calculation, we consider that the underestimation of  $\epsilon_0^z$  by the r<sup>2</sup>SCAN functional is more likely to be due to the functional than to anharmonic phonon calculations.

For rutile TiO<sub>2</sub>, several previous studies reported differences in the results originating from functionals and pseudopotentials [161, 164, 188]. The choice of the correct functionals and pseudopotentials is still an open question. The PBEsol functional describes the  $B_{1u}^1$  modes well, but the overall phonon frequency agreement

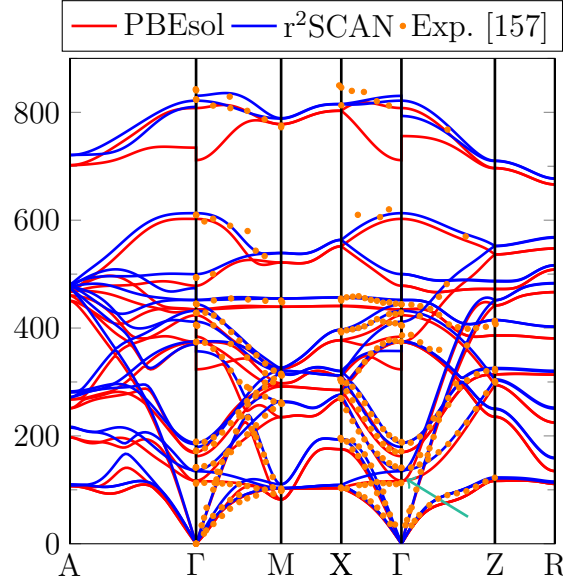


Fig. 5.7: The SCPH+B band structure with  $r^2$ SCAN (blue) and PBEsol (red) functional. The green arrow indicate the  $B_{1u}$  mode, which is overestimated in the  $r^2$ SCAN functional.

is better with  $r^2$ SCAN. In the present study, we have focused on the lattice dielectric properties, and have used the  $r^2$ SCAN functional to better describe the lattice constants and IR-active phonon modes at 300 K.

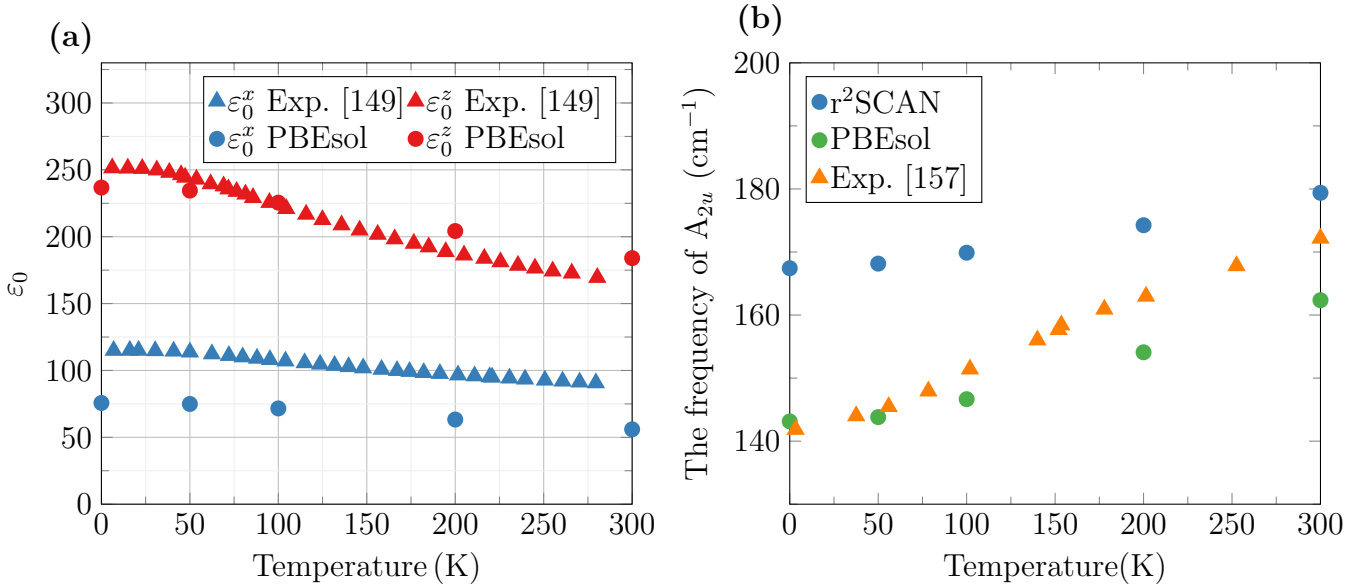


Fig. 5.8: (a) Temperature dependence of the static dielectric constant. The triangular dots show the experimental values and the circular dots show the results from the SCPH+B calculations. (b) Temperature dependence of the SCPH+B phonon frequencies of the  $A_{2u}$  mode.

### 5.3.4 Phonon linewidth

We calculated the frequency-independent linewidths of the four phonon modes involved in the dielectric function in two ways as

$$\gamma^{\text{SCPH+B}} = 2 \text{Im} \Sigma[G^{\text{SCPH+B}}](\omega = \Omega^{\text{SCPH+B}}) \quad (5.7)$$

$$\gamma^{\text{non-SC}} = 2 \text{Im} \Sigma[G^{\text{harm}}](\omega = \omega^{\text{harm}}). \quad (5.8)$$

Here, the factor 2 is attached to connect the linewidth of the FPSQ model and self-energies. While the latter (non-SC) is a usual perturbative calculation estimating self-energies with harmonic phonon frequencies, the

Table 5.4: Comparison of the computed mode frequencies (in  $\text{cm}^{-1}$ ) at the  $\Gamma$  point with experimental data at room temperature. The results from the harmonic approximation (harm), SCPH and SCPH+B are shown at 300 K.

|            | PBEsol |       |        | neutron [157]   |
|------------|--------|-------|--------|-----------------|
|            | harm   | SCPH  | SCPH+B |                 |
| Raman      |        |       |        |                 |
| $A_{1g}$   | 590.2  | 601.3 | 602.4  | 610             |
| $A_{2g}$   | 415.4  | 424.1 | 423.6  | NF <sup>1</sup> |
| $B_{1g}$   | 140.8  | 119.8 | 117.0  | 142             |
| $B_{2g}$   | 793.5  | 802.8 | 807.9  | 824             |
| $E_g$      | 447.4  | 444.8 | 434.5  | 445             |
| non-active |        |       |        |                 |
| $B_{1u}^1$ | 77.9   | 131.9 | 115.9  | 113             |
| $B_{1u}^2$ | 374.4  | 387.4 | 374.3  | 406             |
| TO         |        |       |        |                 |
| $A_{2u}$   | 71.0   | 202.7 | 162.4  | 172.6           |
| $E_u^1$    | 98.8   | 187.0 | 169.9  | 189             |
| $E_u^2$    | 367.3  | 379.2 | 373.8  | 374             |
| $E_u^3$    | 478.0  | 493.0 | 478.4  | 494             |
| LO         |        |       |        |                 |
| $A_{2u}$   | 741.7  | 765.6 | 756.0  | NF              |
| $E_u^1$    | 327.3  | 334.5 | 323.5  | 375             |
| $E_u^2$    | 378.0  | 390.9 | 383.9  | 428             |
| $E_u^3$    | 695.5  | 719.4 | 711.3  | 842             |

<sup>1</sup> NF=not found.

former uses the SCPH+B phonon frequencies. Table 5.5 shows the comparison of computed linewidths with the FPSQ data [155], which is obtained by fitting experimental reflectivity values to the FPSQ model. The SCPH+B calculations agree with the FPSQ data, while the Non-SC linewidths are overestimated significantly. It indicates that the calculation of linewidth requires accurate determination of phonon frequencies, including anharmonicity, as pointed out by Fu et al. [127]. The lifetimes of LO and TO phonons differ, which indicates that the usual Lorenz model does not work for rutile  $\text{TiO}_2$ . Discrepancies in the  $E_u^1$  and  $A_{2u}$  LO modes could be refined by including higher-order diagrams. Self-energies from the four-phonon scattering give a non-negligible contribution in the  $A_{2u}$  and  $E_u^1$  modes. Such phenomena have been observed in other materials [54].

### 5.3.5 Phonon self energy

To see the full frequency-dependence of self-energies, we performed the self-energy calculations for the four LO phonon modes involved in the dielectric function. Figure 5.9 depicts the imaginary part of the bubble and 4ph self energy of the four phonon modes in the SCPH+B calculations. The self-energy of the  $A_{2u}$  mode is greater than that of three  $E$  modes. As a general trend, the bubble self-energy has a rather strong frequency dependence, while the 4ph self-energy has a weaker dependence. The bubble self-energies are generally larger than the 4ph self-energies, indicating that our quasiparticle imaging with SCPH+B is successful. However, for the  $E_u^1$  and  $A_{2u}$  modes, the 4ph self-energy also have non-negligible contributions at their respective TO phonon frequencies. Therefore, the calculation of the 4ph diagram is also important for the accurate calculation of the dielectric function, even though the bubble diagram has overall larger values.

Table 5.5: Calculated linewidth ( $\text{cm}^{-1}$ ) of IR-active phonon modes at 300 K together with the experimental parameters fitted with the FPSQ model. The contributions from the bubble diagram, from the 4ph diagram and the sum of the two are shown for both non-SC and SCPH+B results.

|          | non-SC |      |       | SCPH+B |      |       | FPSQ [155]      |
|----------|--------|------|-------|--------|------|-------|-----------------|
|          | bubble | 4ph  | total | bubble | 4ph  | total |                 |
| TO       |        |      |       |        |      |       |                 |
| $E_u^1$  | 21.2   | 69.9 | 91.1  | 8.54   | 7.95 | 16.4  | $14.7 \pm 8.0$  |
| $E_u^2$  | 40.7   | 7.09 | 47.8  | 14.5   | 1.81 | 16.2  | $19.3 \pm 2.8$  |
| $E_u^3$  | 28.3   | 11.6 | 39.9  | 12.6   | 3.47 | 16.0  | $22.4 \pm 3.1$  |
| $A_{2u}$ | 29.3   | 51.8 | 81.1  | 16.3   | 9.57 | 25.7  | $20.0 \pm 10.2$ |
| LO       |        |      |       |        |      |       |                 |
| $E_u^1$  | 13.8   | 2.71 | 16.5  | 7.12   | 0.97 | 8.09  | $8.8 \pm 1.8$   |
| $E_u^2$  | 24.3   | 8.43 | 32.7  | 11.7   | 2.33 | 14.0  | $18.4 \pm 2.2$  |
| $E_u^3$  | 33.0   | 8.39 | 41.4  | 22.6   | 3.88 | 26.5  | $43.9 \pm 5.6$  |
| $A_{2u}$ | 22.8   | 7.58 | 30.4  | 12.6   | 3.62 | 16.2  | $46.4 \pm 5.3$  |

### 5.3.6 Dielectric function

The dielectric function in the  $x$ -direction has three peaks due to the  $E_u$  phonons and the dielectric function in the  $z$ -direction has one peak due to the  $A_{2u}$  phonon. Figure 5.10b shows the calculated real and imaginary part of dielectric function together with experimental data. The blue line represents the SCPH+B calculation, while the green dashed line corresponds to the non-SC results, where we use harmonic phonon frequencies, and calculate the frequency-dependent self-energy as

$$\Sigma^{\text{non-SC}}(\omega) = \text{Im } \Sigma^{\text{B}}[G^{\text{harm}}] + \text{Im } \Sigma^{\text{4ph}}[G^{\text{harm}}]. \quad (5.9)$$

The SCPH+B calculations agree remarkably well with experimental data, whereas the non-SC calculations failed to reproduce experimental data, especially in the  $A_{2u}$  and  $E_u^1$  peaks due to underestimation of phonon frequencies and overestimation of linewidths. The maximum values of the imaginary part of the dielectric function reach  $\varepsilon_{xx} = 785$  and  $\varepsilon_{zz} = 932$ , which are due to the  $E_u^1$  and  $A_{2u}$  phonons with large mode-oscillator strength of  $S(E_u^1) = 1.87 \text{ e}^2/\text{u}$  and  $S(A_{2u}) = 6.12 \text{ e}^2/\text{u}$ , respectively. As shown in Fig. 5.1, the positively charged Ti atoms and negatively charged O atoms move in opposite directions in the  $A_{2u}$  and  $E_u^1$  phonons. On the other hand, in the  $E_u^2$  and  $E_u^3$  phonons, atoms of the same species move in the opposite directions, leading to much smaller mode oscillator strength. The SCPH renormalization of phonon eigenvectors is negligible, and it is the phonon frequencies and self-energies that affect the calculation results of dielectric properties.

Figure 5.10c shows the reflectivity  $R$  of optical waves normal to the surface in  $x$  and  $z$  directions, which is given by

$$R(\omega) = \left| \frac{\sqrt{\varepsilon(\omega)} - 1}{\sqrt{\varepsilon(\omega)} + 1} \right|^2. \quad (5.10)$$

For the  $x$  direction, the dip due to the  $E_u^2$  phonon ( $380 \text{ cm}^{-1}$ ) is shallower than the experimental data, whereas the dip due to the  $E_u^1$  and  $E_u^3$  phonons (below  $200 \text{ cm}^{-1}$  and  $450 \text{ cm}^{-1}$ ) are in good agreement with experiment. The SCPH+B calculations are overall in better agreement with experiment than the non-SC calculations.

To investigate the influence of the frequency dependence of the self-energy, dielectric functions in the logarithm scale are shown in Fig. 5.11, with the experimental values from Schoche [155].  $\varepsilon_{xx}$  and  $\varepsilon_{zz}$  have one peak each at about  $600 \text{ cm}^{-1}$ , which is not the location of any  $\Gamma$  point IR-active phonon frequency. Several experiments [6, 155] reported that adding these peaks to the FPSQ model improved consistency with experimental values. The peak positions are listed in Table 5.6 with these experimental values.

Although lattice defects or impurities have been suggested as potential origin of these peaks, the causes are still unclear [155]. The imaginary part of frequency-dependent self-energies can explain these peaks.

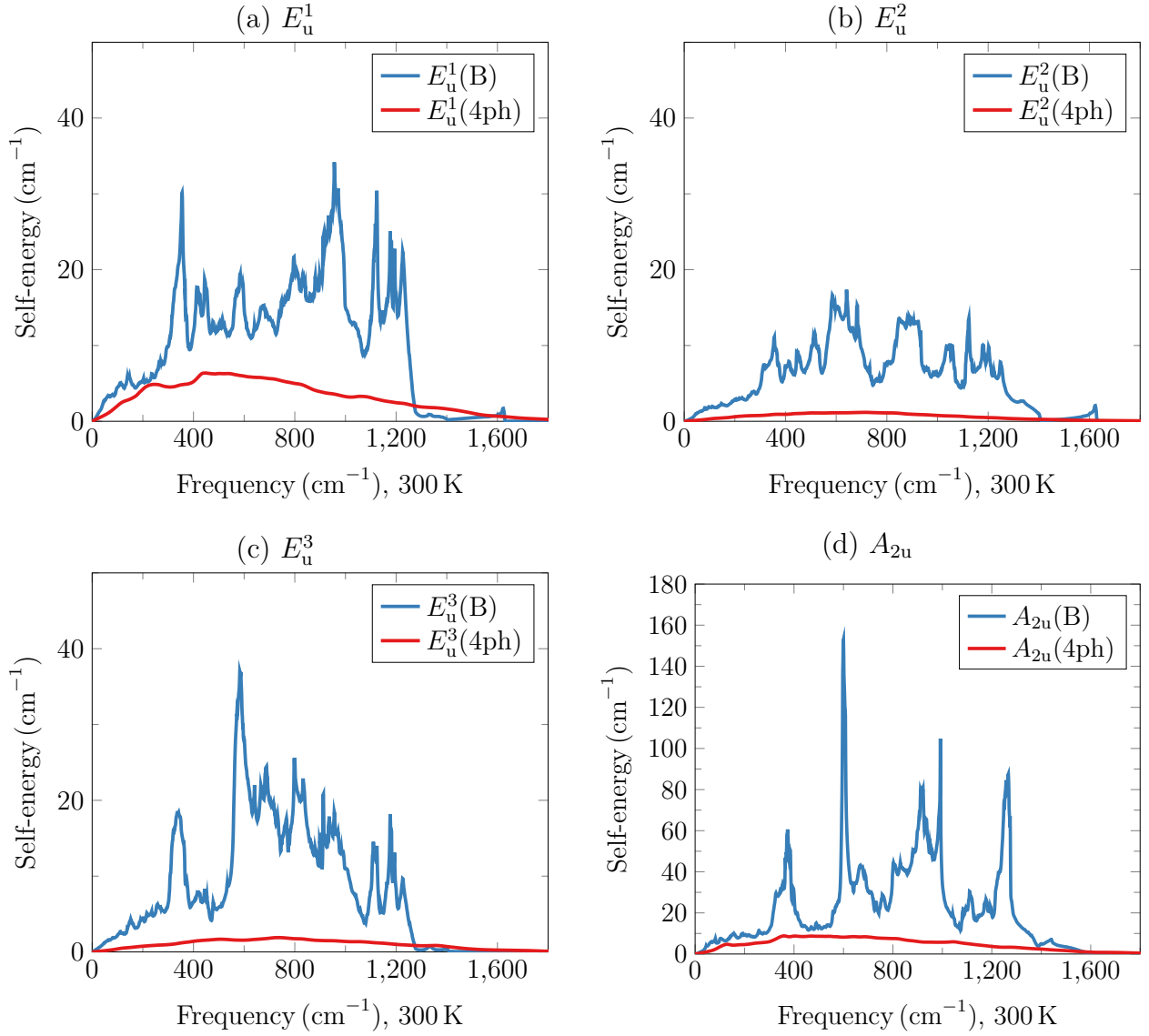


Fig. 5.9: The calculated imaginary part of the bubble (blue) and 4ph (red) self-energy for four IR active phonon modes.

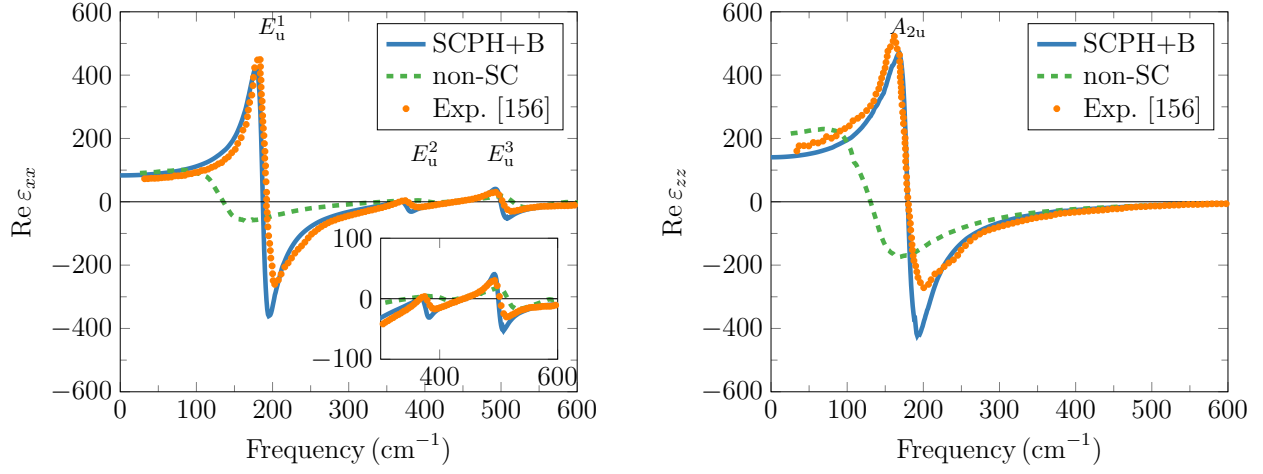
Table 5.6: Positions of additional peaks (cm<sup>-1</sup>).  $\varepsilon_{x,1}$  is for  $\varepsilon_{xx}$  and  $\varepsilon_{z,1}$  is for  $\varepsilon_{zz}$ .

| Mode                | r <sup>2</sup> SCAN | FPSQ [153] | FPSQ [155]   |
|---------------------|---------------------|------------|--------------|
| $\varepsilon_{x,1}$ | 563                 | 585        | $556 \pm 5$  |
| $\varepsilon_{z,1}$ | 598                 | 592        | $587 \pm 12$ |

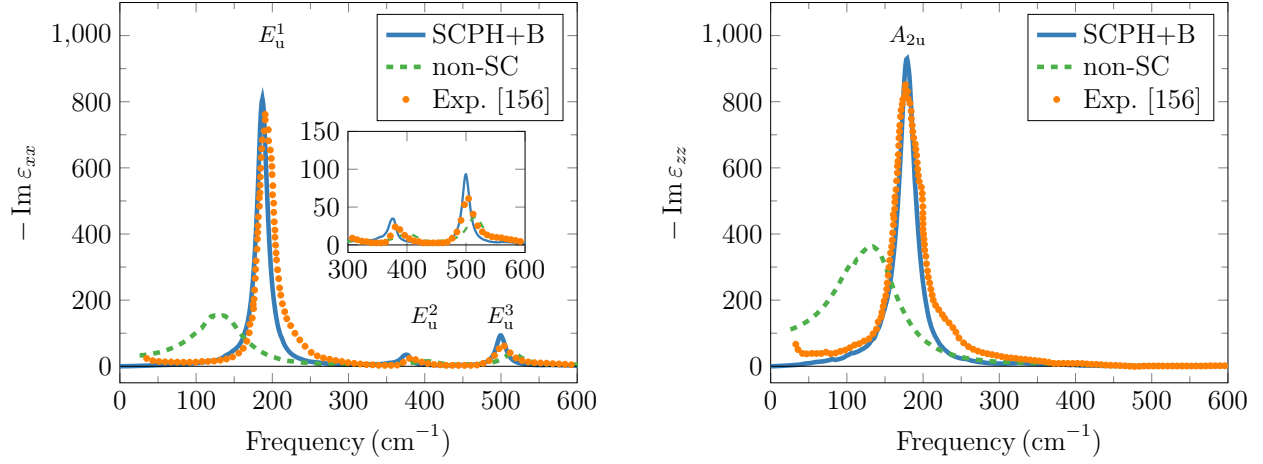
The frequency dependence of the 4ph self-energy is not so strong, whereas the bubble self-energy has strong frequency dependence in rutile TiO<sub>2</sub>, as shown in Fig. 5.9. Figure 5.12 shows the bubble self-energies of the  $E_u^3$  and  $A_{2u}$  phonons which mostly contributed to additional peaks of  $\varepsilon_{xx}$  and  $\varepsilon_{zz}$ , respectively. Vertical dotted lines indicate the locations of additional peaks. There are peaks in the bubble self-energies at the locations of the extra peaks as well. Thus, we ascribe the additional peaks to the bubble self-energy.

When the bubble diagram is taken into account, the dielectric function, and thus the Green's function, has peaks at a certain frequency  $\omega$  when the two phonons with frequencies  $(\omega_1, \omega_2)$  satisfy the relation  $\omega = \omega_1 \pm \omega_2$  and  $\mathbf{q}_1 \pm \mathbf{q}_2 = \mathbf{0}$ . The positive sign corresponds to phonon emission, and the negative sign to phonon absorption. Such phonon pairs can be specified by the two phonon density of state (TDOS), which

(a)



(b)



(c)

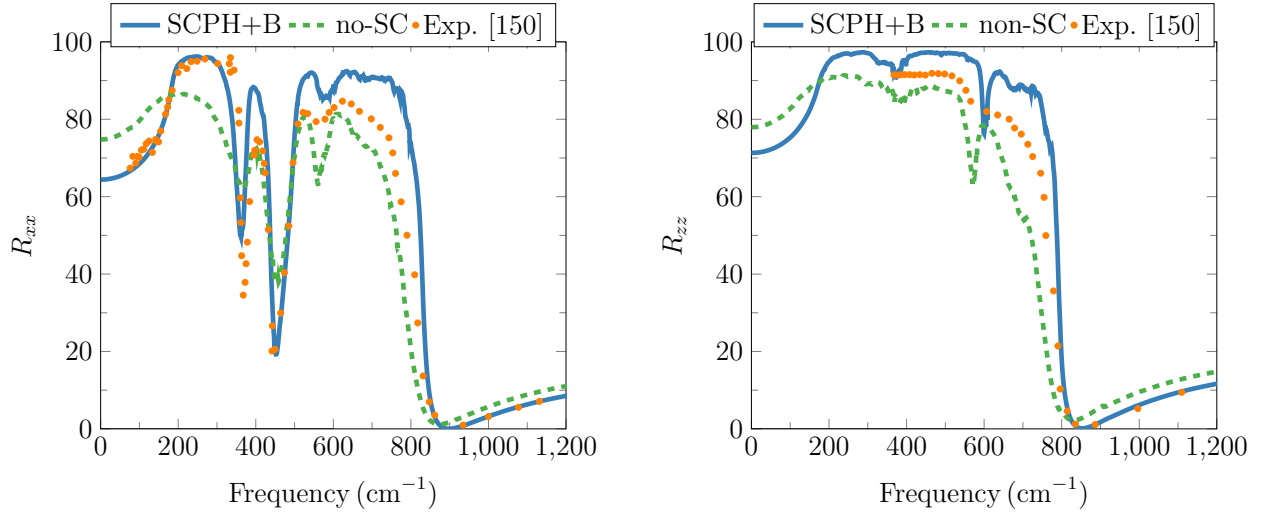


Fig. 5.10: (a,b) Calculated real/imaginary part of dielectric functions  $\epsilon_{xx}$  (left) and  $\epsilon_{zz}$  (right) from SCPH+B (solid blue lines) and harmonic approximation (dashed green lines) with experimental data at room temperature [156] (orange open circles). The TO phonons corresponding to the peaks are marked. (c) Calculated reflectivity from SCPH+B (solid blue lines) with experimental data at room temperature [150].

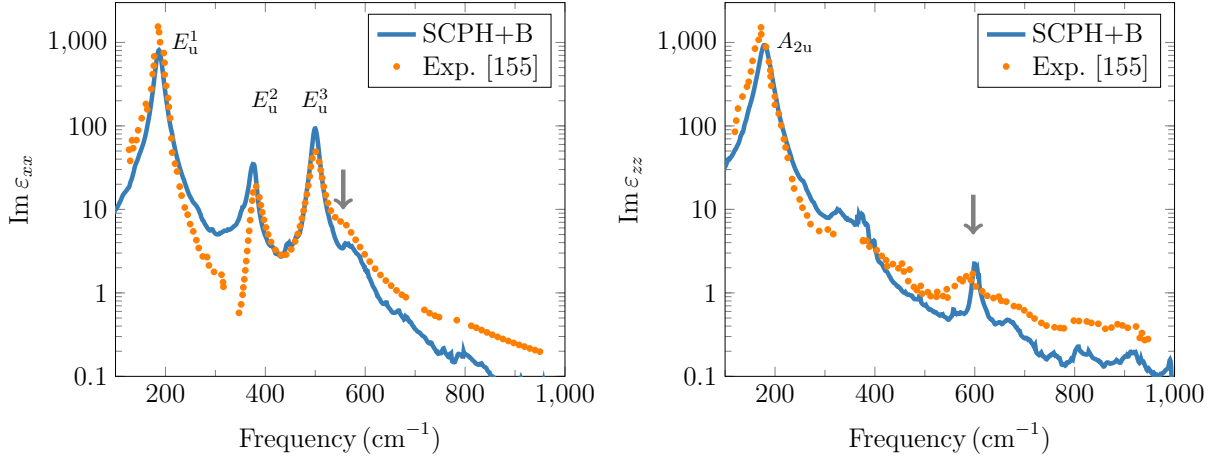


Fig. 5.11: Calculated imaginary part of dielectric functions with experimental data from Schoche [155] in a logarithm scale. Both  $\epsilon_{xx}$  and  $\epsilon_{zz}$  have a peak at about 600 cm<sup>-1</sup>, which does not belong to any IR-active phonon frequency, and these peaks are indicated by the gray arrows.

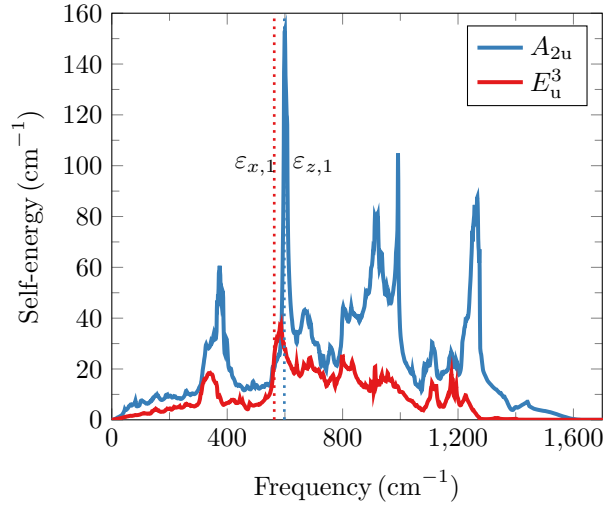


Fig. 5.12: Calculated imaginary part of frequency dependent bubble self-energy of  $A_{2u}$  (blue) and  $E_u^3$  (red) modes. Blue and red vertical lines represent the additional peaks for  $\epsilon_{zz}$  and  $\epsilon_{xx}$ , respectively.

is defined as follows,

$$\text{TDOS}_{\pm}(\omega, \mathbf{q}) = \frac{1}{N_{\text{cell}}} \sum_{\substack{(\mathbf{q}_1, j_1) \\ (\mathbf{q}_2, j_2)}} \delta(\omega \pm \omega_{\mathbf{q}_1 j_1} - \omega_{\mathbf{q}_2 j_2}) \delta_{\mathbf{q} \pm \mathbf{q}_1, \mathbf{q}_2 + \mathbf{G}}, \quad (5.11)$$

where  $N_{\text{cell}}$  is the number of  $\mathbf{q}$  points in the summation (see also Eq. (3.32)), and  $\mathbf{G}$  is a reciprocal lattice vector. Figure 5.13 shows the calculated TDOS( $\omega, \mathbf{q} = \mathbf{0}$ ) with a  $15 \times 15 \times 15$   $\mathbf{q}$  points grid, in which TDOS for the emission process has a considerable value at around 600 cm<sup>-1</sup>. Moreover, phonon DOS peaks from Fig. 5.4 can be seen at around 115, 210, 300, 398, and 455 cm<sup>-1</sup>; acoustic phonons are responsible for the 115 cm<sup>-1</sup> peak, whereas optical phonons are responsible for the remaining peaks. Therefore, the emission process of the pairs (115 cm<sup>-1</sup>, 455 cm<sup>-1</sup>), (210 cm<sup>-1</sup>, 398 cm<sup>-1</sup>) and (300 cm<sup>-1</sup>, 300 cm<sup>-1</sup>) is responsible for the 600 cm<sup>-1</sup> additional peak. Notably, the first pair emission process, involving the acoustic modes, is contributed by phonons with non-zero wave numbers, which can not be detected via single phonon processes by optical probes that are sensitive to  $\Gamma$  point phonons.

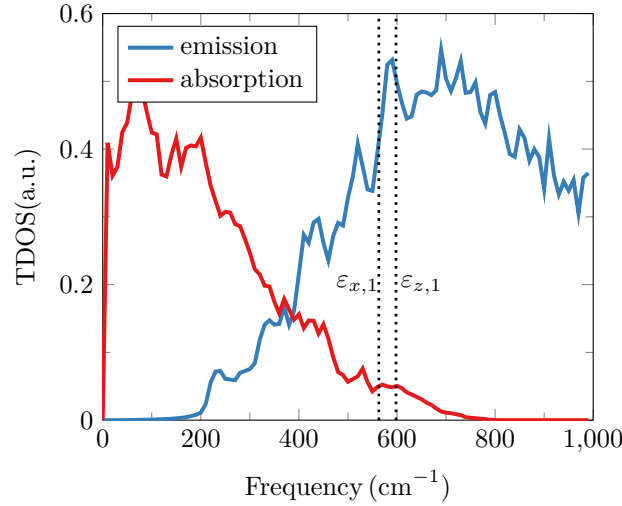


Fig. 5.13: Calculated  $\text{TDOS}_{\pm}(\omega, \mathbf{q} = \mathbf{0})$  for absorption (red)  $\omega = \omega_1 - \omega_2$  and emission (blue)  $\omega = \omega_1 + \omega_2$ . Red vertical lines represent the positions of additional peaks.

## 5.4 Conclusions

We studied the infrared spectra of rutile  $\text{TiO}_2$  using first-principles (DFT) calculations and lattice dynamics calculations. The calculation of phonon frequencies was performed using the SCPH+B theory, a self-consistent anharmonic phonon theory [Fig. 5.4]. The dielectric properties were calculated with fully incorporating the frequency dependence of the self-energies, and in addition to the normally used bubble diagram, a higher-order diagram, the 4ph diagram, was also included. To the best of our knowledge, this is the first attempt to calculate dielectric functions that includes SCPH theory and frequency-dependent self-energies. Three different functionals were also used to investigate their effect on phonon properties.

The SCPH+B calculation very well described the  $E_u^1$  and  $A_{2u}$  phonon frequencies, which were greatly underestimated in the harmonic approximation and overestimated in the perturbative approach. Therefore, self-consistent treatment is essential for accurately describing phonon frequencies. We also compared the three functionals: LDA, PBEsol, and r<sup>2</sup>SCAN, finding that the r<sup>2</sup>SCAN functional is more predictive, especially in describing the  $E_u^1$  and  $A_{2u}$  mode. The phonon frequency of the  $B_{1u}^1$  mode and the temperature dependence of  $\epsilon_0^z$ , which do not match the experiment with the r<sup>2</sup>SCAN, are found to be in good agreement with the PBEsol functional. Although r<sup>2</sup>SCAN is superior for describing the overall dielectric properties, further improvement of the functional may be necessary.

Phonon self-energies were calculated using both the perturbation theory (non-SC) and the SCPH+B theory. They were significantly overestimated in the non-SC calculation, as suggested by Fu et al. [127]. The SCPH+B calculations well reproduced previous studies where FPSQ models were used together with experiments. We also found that the contribution from the 4ph self-energy is non-negligible at 300 K. Our central result is the calculation of dielectric properties by SCPH+B, which is found to reproduce experiments significantly better than calculations based on the perturbation theory. We emphasized that this accuracy can be achieved by phonon frequency estimation by SCPH+B, the subsequent correction of the overestimation of phonon linewidths, and the consideration of the 4ph phonon diagram. Furthermore, we attributed the experimentally known additional peaks at around  $600\text{cm}^{-1}$  to the two phonon emission process included in the frequency-dependent bubble diagram, demonstrating the importance of the frequency dependence of phonon self-energies. We expect the presented approach is effective for predicting the dielectric properties of other materials.



## Chapter 6

# Dielectric Properties of Liquid Alcohols and Its Polymers

This chapter is not disclosed because it will be published in a journal within 5 years.



# Chapter 7

## Conclusion

### 7.1 Summary of This Thesis

In this thesis, we developed methods to calculate dielectric properties based on first principles calculations and studied the dielectric properties of the strongly anharmonic rutile  $\text{TiO}_2$  crystal and primary liquid alcohols.

We have developed two methods suitable for crystalline and liquid systems. The first method targets crystals and is based on anharmonic phonon methods, introduced in chapter 3. Due to the linear response theory, phonon self-energies are important for calculating dielectric properties. At the lowest order of expansion, the real part of the phonon self-energy gives the frequency shift, and the imaginary part gives the linewidth. However, using the usual perturbation theory to calculate the self-energy has the problem that the dielectric properties cannot be calculated correctly for crystals with strong anharmonicity. Therefore, we combined this theory with the self-inconsistent phonon theory, which describes phonons in strongly anharmonic cases, and developed a methodology that can be applied to highly anharmonic crystals.

Another method developed to overcome the long computation time in MD simulations is to predict dipole moments by machine learning, which was introduced in chapter 4 together with the modern theory of polarization. Unlike the anharmonic phonon method, this method is based on MD simulations and can, in principle, be applied to liquids and amorphous materials as well as crystals. In the modern theory of polarization, the contribution of electrons to the dipole moments of a system is identified with the center of mass of its Wannier function (Wannier centers, WCs). In this method, we assign WCs to chemical bonds rather than molecules, and machine learning models predict WCs for each bond species. This not only makes it possible to apply the method to large molecules but also increases the possibility of transferring the models created for each bonding species to other systems, thereby increasing its versatility.

We emphasized that both methods are based on quantum mechanical polarization. The usual static scalar charges classically assigned to atoms cannot represent polarization correctly. Instead of a scalar charge, a  $3 \times 3$  tensor called the Born effective charge was introduced in the anharmonic phonon method. In the latter machine learning model, on the other hand, the contribution of the electrons is explicitly represented as WCs, directly describing subtle changes in polarization due to intramolecular deformations and intermolecular interactions. Both models are, of course, consistent in the limit of small atomic displacements.

Anharmonic phonon methods are faster and generally more accurate than MD methods. On the other hand, the machine learning model of WCs is used in conjunction with MD simulations and has a broader range of applications, including liquids and amorphous materials. Therefore, it is important to use both methods flexibly according to the system to which they are applied.

In chapter 5, the anharmonic phonon method was applied to the strongly anharmonic rutile  $\text{TiO}_2$ . The calculation of phonon frequencies was performed using the SCPH+B theory, a self-consistent anharmonic phonon theory. The SCPH+B calculation described the target phonon frequencies well, which were greatly underestimated in the harmonic approximation. We showed that the anharmonicity in these modes was too strong to treat in a perturbative approach, and self-consistent treatment was essential for accurately describing phonon frequencies. We also found that the contribution from the 4ph self-energy is non-negligible at 300 K. The SCPH+B dielectric function showed good agreement with experimental values. Furthermore, the additional peaks at around  $600\text{cm}^{-1}$  pointed out in the previous experiments can be attributed to the two phonon emission process included in the frequency-dependent bubble diagram, which shows the importance of the frequency dependence of phonon self-energies in accurately calculating the dielectric function.

In chapter 6, we applied our proposed machine learning dipole moments with a bond dipole scheme to the liquid alcohols of methanol and ethanol, propylene glycol (PG), and its polymers. To demonstrate the validity of our scheme, we applied it to methanol and ethanol. Our model showed very high accuracy, with  $\text{RMSE} = 0.05\text{D}$  for each bond and  $\text{RMSE} = 0.1\text{D}$  for the molecular dipoles, considering that we did not include molecular dipoles in loss functions. The models were then used to calculate the dielectric constant

and dielectric function, reproducing the experimental values well. Furthermore, by comparing the results with models created from isolated systems, we showed that the molecular dipoles are greatly enhanced in liquids, especially by the O-lone pair WCs. The 60% of the dielectric constant of methanol is due to the electronic polarization from intermolecular interactions. The other applications are PG, PG2, and PPG725 to demonstrate the applicability and transferability of our model. In this calculation, we have shown two things. First, our model is applicable to giant molecules such as PPG725, which contains 123 atoms in a molecule. Second, we have shown that the model trained on PG2 is also applicable to its polymer, PPG725.

## 7.2 Future Issues

We would like to conclude the thesis by making some remarks on the future prospects of the method presented here. From a methodology development perspective, some remaining work must be done. First, the effects of higher-order phonon diagrams are not well understood. Recently, a new way to incorporate bubble diagrams in a self-consistent manner [217] has been proposed, and such a theory may further clarify the effects of higher-order diagrams. The SCPH+B theory used in this study neglects the effect of phonon linewidth on the anharmonic phonon frequency (thermal phonon effect). The actual extent of the thermal phonon effect has not yet been clarified theoretically, and such theoretical development may be necessary for a better understanding of dielectric properties. In addition to the phonon self-energy, the effect of the higher-order terms in the Born effective charge is also an unresolved issue. This effect is known to be weak in weakly anharmonic materials, but it may have a significant effect in some systems.

With regard to machine learning for WCs, the critical issue is whether it is possible to create more versatile models. In this thesis, we were only able to present calculations for a limited number of materials, but there is potential to create a base model that can be applied to a broader range of materials, and we are currently working on this. It may be necessary to change the machine learning model to a more advanced one, such as a graph neural network, or to generate training data efficiently by active learning. Such base models are essential for industrial applications and to explore more materials in a limited amount of time and computational resources. Another possibility is to incorporate effects from more distant atoms in the form of electric fields. In this thesis, we used classical MD or AIMD, but it is also possible to achieve a balance between accuracy and speed by combining it with machine learning MD. Although not presented in this thesis, such calculations are currently in progress.

We expect that the methods developed in this thesis will be used to calculate the dielectric properties of many materials, including amorphous polymers, and will be effective not only for elucidating the physical origins of dielectric spectra but also for developing various dielectric materials, including materials for high-speed communications.

## Appendix A

# Additional Simulation Results on Rutile $\text{TiO}_2$

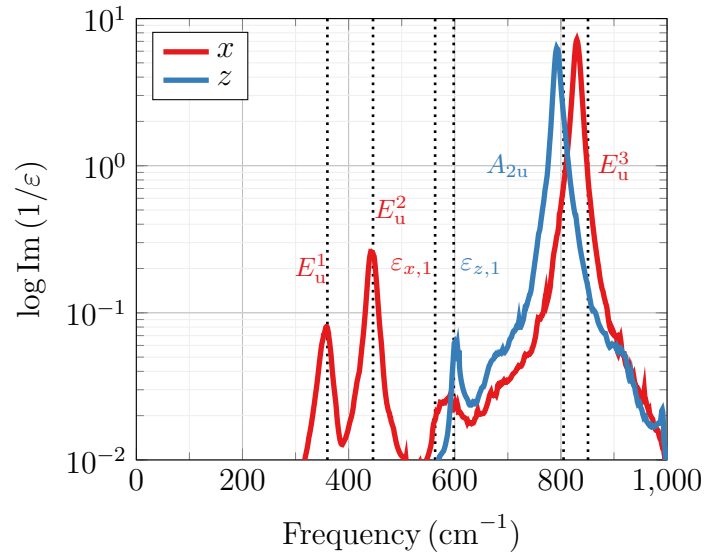


Fig. A.1: Calculated imaginary part of the extinction coefficient  $\eta(\omega) = 1/\varepsilon(\omega)$  for  $x$  (red) and  $z$  (blue) axis. The vertical dotted lines represent the energy positions of LO phonons from Table 5.3 and additional peaks from Table 5.6.

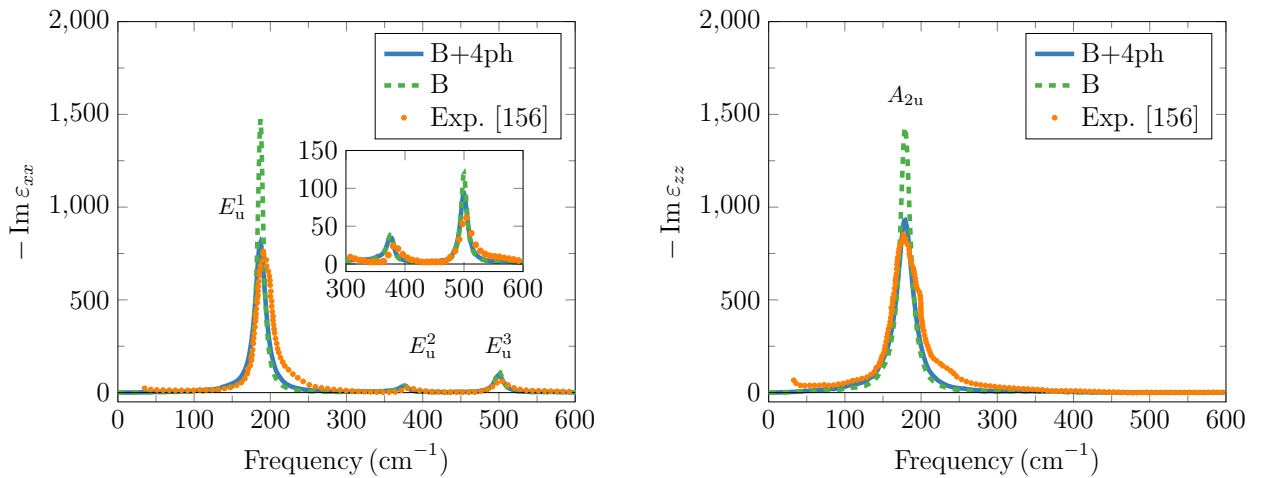


Fig. A.2: Calculated imaginary part of dielectric functions  $\varepsilon_{xx}$  (left) and  $\varepsilon_{zz}$  (right) from SCPH+B using both the bubble and 4ph (solid blue lines) and only bubble (dashed green lines) with experimental data at room temperature [156] (orange circles). The TO phonons corresponding to the peaks are marked.

We present the additional calculation results for rutile  $\text{TiO}_2$ . Figure A.1 shows the imaginary part of the

extinction coefficient

$$\eta(\omega) = \frac{1}{\varepsilon(\omega)}, \quad (\text{A.1})$$

which has the peaks at LO phonon frequencies in theory. Calculated peaks from SCPH+B calculations agree well with experimental LO phonon frequencies illustrated in vertical lines. We also note that the extinction coefficient also spikes at the positions of the additional peaks.

In Table 5.5, we discussed the 4ph diagram is not negligible especially for  $E_u^1$  and  $A_{2u}$ . Figure A.2 demonstrates the impact of the 4ph diagram on the imaginary part of the dielectric function. Without the 4ph diagram, the peak heights of  $E_u^1$  and  $A_{2u}$  are largely overestimated, with narrower linewidths. It is necessary to include the 4ph diagram to reproduce the experimental data.

# Acknowledgement

I would like to express my deepest gratitude to my supervisor, Prof. Shinji Tsuneyuki for his enormous encouragement, guidance, patience and support for my study. I am genuinely grateful to Assistant Prof. Takahiro Ishikawa for stimulative discussions. I am deeply indebted to former Assistant Prof. Ryosuke Akashi for his encouragement and insightful discussions during the research. I also thank all the members of Tsuneyuki research group.

I would like to show my sincere appreciation to my research collaborators. This study was conducted in collaboration with JSR Corporation via JSR-UTokyo Collaboration Hub, CURIE. I am extremely beholden Mr. Tamio Yamazaki (JSR), who has given me extensive advice throughout the research period. My gratitude also goes to Dr. Itti Rittaporn (JSR) and Dr. Kouichi Hasegawa (JSR) for their help in my research with CURIE. I would like to offer my special thanks to Dr. Terumasa Tadano (NIMS) for constructive discussion on the anharmonic phonon method and gracious acceptance of my stay at NIMS.

I am gratefully obliged Mr. Kiyofumi Suzuki (RIST), Mr. Akira Saito (RIST), Mr. Satoru Shingu (RIST), Mr. Shinichi Ichikawa (Fujitsu), and Mr. Kenta Watanabe (Fujitsu) for a lot of advice on technical aspects of the supercomputer Fugaku.

I was supported by MERIT program for leading graduate schools. I would like to convey my appreciation to my supervisor Prof. Ryotaro Arita for his encouragement and helpful discussions throughout the program.

My acknowledgement also goes to Profs. Osamu Sugino, Satoru Nakatsuji, Synge Todo, Ryo Shimano, and Satoshi Watanabe, the referees of this thesis, for their invaluable advice to improve this thesis.

The computations on anharmonic phonon calculations have been done using the facility of the Supercomputer Center, the Institute for Solid State Physics, the University of Tokyo. The calculations related to machine learning and molecular dynamics simulations have been conducted using computational resources of the supercomputer Fugaku provided by the RIKEN Center for Computational Science (ProjectID: hp220331, hp230124). This research was funded by a JST-Mirai Program Grant Number JPMJMI20A1, a MEXT Quantum Leap Flagship Program (MEXT Q-LEAP) grant number JPMXS0118067246, Japan, and JSR Corporation via JSR-UTokyo Collaboration Hub, CURIE.

Lastly, I want to express my heartfelt thankfulness to my family and friends for their unwavering support throughout my doctoral research.



# Bibliography

- [1] S. K. Kim, W.-D. Kim, K.-M. Kim, C. S. Hwang, and J. Jeong, *Applied Physics Letters* **85**, 4112 (2004).
- [2] Ph. Ghosez, J.-P. Michenaud, and X. Gonze, *Physical Review B* **58**, 6224 (1998).
- [3] K. S. Cole and R. H. Cole, *The Journal of Chemical Physics* **9**, 341 (2004).
- [4] S. Havriliak and S. Negami, *Journal of Polymer Science Part C: Polymer Symposia* **14**, 99 (1966).
- [5] R. Kubo, *Journal of the Physical Society of Japan* **12**, 570 (1957).
- [6] F. Gervais and B. Piriou, *Journal of Physics C: Solid State Physics* **7**, 2374 (1974).
- [7] R. Cowley, *Advances in Physics* **12**, 421 (1963).
- [8] M. Born, K. Huang, and M. Lax, *American Journal of Physics* **23**, 474 (1955).
- [9] X. Gonze and C. Lee, *Physical Review B* **55**, 10355 (1997).
- [10] X. Gonze and J.-P. Vigneron, *Physical Review B* **39**, 13120 (1989).
- [11] X. Gonze, *Physical Review A* **52**, 1096 (1995).
- [12] S. Baroni, S. de Gironcoli, A. Dal Corso, and P. Giannozzi, *Reviews of Modern Physics* **73**, 515 (2001).
- [13] M. French, S. Hamel, and R. Redmer, *Physical Review Letters* **107**, 185901 (2011).
- [14] F. Grasselli and S. Baroni, *Nature Physics* **15**, 967 (2019).
- [15] K. Shimizu, R. Otsuka, M. Hara, E. Minamitani, and S. Watanabe, *Science and Technology of Advanced Materials: Methods* **3**, 2253135 (2023).
- [16] E. R. Cowley, *Journal of Physics C: Solid State Physics* **5**, 1345 (1972).
- [17] J. E. Eldridge and P. R. Staal, *Physical Review B* **16**, 4608 (1977).
- [18] E. J. Wu and G. Ceder, *Journal of Applied Physics* **89**, 5630 (2001).
- [19] L. Paulatto, F. Mauri, and M. Lazzeri, *Physical Review B* **87**, 214303 (2013).
- [20] W. Li, J. Carrete, N. A. Katcho, and N. Mingo, *Computer Physics Communications* **185**, 1747 (2014).
- [21] A. Chernatynskiy and S. R. Phillpot, *Computer Physics Communications* **192**, 196 (2015).
- [22] A. Togo, J. Chaput, and I. Tanaka, *Physical Review B* **91**, 094306 (2015).
- [23] F. Bottin, L. Bieder, and J. Bouchet, *Computer Physics Communications* **254**, 107301 (2020).
- [24] L. Monacelli, R. Bianco, M. Cherubini, M. Calandra, I. Errea, and F. Mauri, *Journal of Physics: Condensed Matter* **33**, 363001 (2021).
- [25] T. Tadano, Y. Gohda, and S. Tsuneyuki, *Physical Review B* **26**, 225402 (2014).
- [26] T. Tadano and S. Tsuneyuki, *Journal of the Ceramic Society of Japan* **127**, 404 (2019).
- [27] O. Hellman, I. A. Abrikosov, and S. I. Simak, *Physical Review B* **84**, 180301 (2011).
- [28] T. Tadano and S. Tsuneyuki, *Physical Review B* **92**, 054301 (2015).
- [29] T. Tadano and S. Tsuneyuki, *Journal of the Physical Society of Japan* **87**, 041015 (2018).
- [30] D. J. Hooton, *The London, Edinburgh, and Dublin Philosophical Magazine and Journal of Science* (1955), 10.1080/14786440408520575.
- [31] T. R. Koehler, *Physical Review Letters* **17**, 89 (1966).
- [32] H. Horner, *Zeitschrift für Physik* **205**, 72 (1967).
- [33] N. R. Werthamer, *Physical Review B* **1**, 572 (1970).
- [34] P. Souvatzis, O. Eriksson, M. I. Katsnelson, and S. P. Rudin, *Physical Review Letters* **100**, 095901 (2008).
- [35] I. Errea, M. Calandra, and F. Mauri, *Physical Review B* **89**, 064302 (2014).
- [36] T. Tadano and W. A. Saidi, *Physical Review Letters* **129**, 185901 (2022).
- [37] T. Feng and X. Ruan, *Physical Review B* **93**, 045202 (2016).
- [38] T. Feng, L. Lindsay, and X. Ruan, *Physical Review B* **96**, 161201 (2017).
- [39] T. Feng and X. Ruan, *Physical Review B* **97**, 045202 (2018).
- [40] J. S. Kang, H. Wu, M. Li, and Y. Hu, *Nano Letters* **19**, 4941 (2019).
- [41] C. Kwon, Y. Xia, F. Zhou, and B. Han, *Physical Review B* **102**, 184309 (2020).
- [42] Y. Xia, K. Pal, J. He, V. Ozoliņš, and C. Wolverton, *Physical Review Letters* **124**, 065901 (2020).
- [43] A. van Roekeghem, J. Carrete, S. Curtarolo, and N. Mingo, *Physical Review Materials* **4**, 113804 (2020).
- [44] W. I. Choi, J. S. An, I. Jang, and D. S. Kim, *Current Applied Physics* **29**, 78 (2021).

- [45] F. Bechstedt, P. Käckell, A. Zywietz, K. Karch, B. Adolph, K. Tenelsen, and J. Furthmüller, *physica status solidi (b)* **202**, 35 (1997).
- [46] A. Debernardi, *Physical Review B* **57**, 12847 (1998).
- [47] G. Lang, K. Karch, M. Schmitt, P. Pavone, A. P. Mayer, R. K. Wehner, and D. Strauch, *Physical Review B* **59**, 6182 (1999).
- [48] A. Debernardi, S. Baroni, and E. Molinari, *Physical Review Letters* **75**, 1819 (1995).
- [49] A. Debernardi, C. Ulrich, K. Syassen, and M. Cardona, *Physical Review B* **59**, 6774 (1999).
- [50] X. Tang and B. Fultz, *Physical Review B* **84**, 054303 (2011).
- [51] M. Xu, J. Y. Yang, and L. H. Liu, *Materials Research Express* **3**, 075006 (2016).
- [52] A. Chmeruk and M. Núñez-Valdez, *Applied Physics A* **129**, 477 (2023).
- [53] G. Fugallo, B. Rousseau, and M. Lazzeri, *Physical Review B* **98**, 184307 (2018).
- [54] X. Yang, T. Feng, J. S. Kang, Y. Hu, J. Li, and X. Ruan, *Physical Review B* **101**, 161202 (2020).
- [55] Z. Tong, X. Yang, T. Feng, H. Bao, and X. Ruan, *Physical Review B* **101**, 125416 (2020).
- [56] A. Rahman, *Physical Review* **136**, A405 (1964).
- [57] M. Neumann, *Molecular Physics* **50**, 841 (1983).
- [58] M. Neumann and O. Steinhauser, *Chemical Physics Letters* **102**, 508 (1983).
- [59] M. Neumann and O. Steinhauser, *Chemical Physics Letters* **106**, 563 (1984).
- [60] J. Kolafa and L. Viererblová, *Journal of Chemical Theory and Computation* **10**, 1468 (2014).
- [61] T. M. Nymand, C. Rønne, and S. R. Keiding, *The Journal of Chemical Physics* **114**, 5246 (2001).
- [62] R. S. Mulliken, *The Journal of Chemical Physics* **36**, 3428 (2004).
- [63] F. L. Hirshfeld, *Theoretica chimica acta* **44**, 129 (1977).
- [64] R. F. W. Bader, T. T. Nguyen-Dang, and Y. Tal, *Reports on Progress in Physics* **44**, 893 (1981).
- [65] C. I. Bayly, P. Cieplak, W. Cornell, and P. A. Kollman, *The Journal of Physical Chemistry* **97**, 10269 (1993).
- [66] P. L. Silvestrelli and M. Parrinello, *Physical Review Letters* **82**, 3308 (1999).
- [67] P. J. Dyer and P. T. Cummings, *The Journal of Chemical Physics* **125**, 144519 (2006).
- [68] R. Car and M. Parrinello, *Physical Review Letters* **55**, 2471 (1985).
- [69] J.-W. Handgraaf, T. S. van Erp, and E. J. Meijer, *Chemical Physics Letters* **367**, 617 (2003).
- [70] J.-W. Handgraaf, E. J. Meijer, and M.-P. Gaigeot, *The Journal of Chemical Physics* **121**, 10111 (2004).
- [71] K. N. Woods and H. Wiedemann, *The Journal of Chemical Physics* **123**, 134506 (2005).
- [72] M. J. McGrath, I.-F. W. Kuo, J. N. Ghogomu, C. J. Mundy, and J. I. Siepmann, *The Journal of Physical Chemistry B* **115**, 11688 (2011).
- [73] M. J. McGrath, I.-F. W. Kuo, and J. I. Siepmann, *Physical Chemistry Chemical Physics* **13**, 19943 (2011).
- [74] V. K. Yadav, A. Karmakar, J. R. Choudhuri, and A. Chandra, *Chemical Physics* **408**, 36 (2012).
- [75] C. C. Wang, J. Y. Tan, and L. H. Liu, *AIP Advances* **7**, 035115 (2017).
- [76] A. Jindal and S. Vasudevan, *Physical Chemistry Chemical Physics* **22**, 6690 (2020).
- [77] R. D. King-Smith and D. Vanderbilt, *Physical Review B* **47**, 1651 (1993).
- [78] R. Resta, *Ferroelectrics* **151**, 49 (1994).
- [79] R. Resta, *Reviews of Modern Physics* **66**, 899 (1994).
- [80] R. Resta, *Physical Review Letters* **80**, 1800 (1998).
- [81] R. Resta and D. Vanderbilt, in *Physics of Ferroelectrics: A Modern Perspective*, Topics in Applied Physics (Springer, Berlin, Heidelberg, 2007) pp. 31–68.
- [82] A. Debernardi, M. Bernasconi, M. Cardona, and M. Parrinello, *Applied Physics Letters* **71**, 2692 (1997).
- [83] M. Sharma, Y. Wu, and R. Car, *International Journal of Quantum Chemistry* **95**, 821 (2003).
- [84] P. Partovi-Azar and T. D. Kühne, *Journal of Computational Chemistry* **36**, 2188 (2015).
- [85] M. Pagliai, C. Cavazzoni, G. Cardini, G. Erbacci, M. Parrinello, and V. Schettino, *The Journal of Chemical Physics* **128**, 224514 (2008).
- [86] H. Bao, B. Qiu, Y. Zhang, and X. Ruan, *Journal of Quantitative Spectroscopy and Radiative Transfer* **113**, 1683 (2012).
- [87] J. Y. Yang, W. J. Zhang, L. H. Liu, J. Qiu, K. Wang, and J. Y. Tan, *The Journal of Chemical Physics* **141**, 104703 (2014).
- [88] A. Krishnamoorthy, K.-i. Nomura, N. Baradwaj, K. Shimamura, P. Rajak, A. Mishra, S. Fukushima, F. Shimojo, R. Kalia, A. Nakano, and P. Vashishta, *Physical Review Letters* **126**, 216403 (2021).
- [89] J. Behler and M. Parrinello, *Physical Review Letters* **98**, 146401 (2007).
- [90] J. Behler, *International Journal of Quantum Chemistry* **115**, 1032 (2015).
- [91] H. Wang, L. Zhang, J. Han, and W. E, *Computer Physics Communications* **228**, 178 (2018).
- [92] J. Zeng, D. Zhang, D. Lu, P. Mo, Z. Li, Y. Chen, M. Rynik, L. Huang, Z. Li, S. Shi, Y. Wang, H. Ye,

- P. Tuo, J. Yang, Y. Ding, Y. Li, D. Tisi, Q. Zeng, H. Bao, Y. Xia, J. Huang, K. Muraoka, Y. Wang, J. Chang, F. Yuan, S. L. Bore, C. Cai, Y. Lin, B. Wang, J. Xu, J.-X. Zhu, C. Luo, Y. Zhang, R. E. A. Goodall, W. Liang, A. K. Singh, S. Yao, J. Zhang, R. Wentzcovitch, J. Han, J. Liu, W. Jia, D. M. York, W. E. R. Car, L. Zhang, and H. Wang, *The Journal of Chemical Physics* **159**, 054801 (2023).
- [93] N. Artrith and A. Urban, *Computational Materials Science* **114**, 135 (2016).
- [94] A. Musaelian, S. Batzner, A. Johansson, L. Sun, C. J. Owen, M. Kornbluth, and B. Kozinsky, “[Learning Local Equivariant Representations for Large-Scale Atomistic Dynamics](#),” (2022), [arxiv:2204.05249 \[cond-mat, physics:physics\]](#).
- [95] M. Geiger and T. Smidt, “[E3nn: Euclidean Neural Networks](#),” (2022), [arxiv:2207.09453 \[cs\]](#).
- [96] S. Batzner, A. Musaelian, L. Sun, M. Geiger, J. P. Mailoa, M. Kornbluth, N. Molinari, T. E. Smidt, and B. Kozinsky, *Nature Communications* **13**, 2453 (2022).
- [97] J. Gilmer, S. S. Schoenholz, P. F. Riley, O. Vinyals, and G. E. Dahl, “[Neural Message Passing for Quantum Chemistry](#),” (2017), [arxiv:1704.01212 \[cs\]](#).
- [98] M. Gastegger, J. Behler, and P. Marquetand, *Chemical Science* **8**, 6924 (2017).
- [99] R. Hou, Y. Quan, and D. Pan, *The Journal of Chemical Physics* **153**, 101103 (2020).
- [100] L. Zhang, M. Chen, X. Wu, H. Wang, W. E, and R. Car, *Physical Review B* **102**, 041121 (2020).
- [101] G. M. Sommers, M. F. C. Andrade, L. Zhang, H. Wang, and R. Car, *Physical Chemistry Chemical Physics* **22**, 10592 (2020).
- [102] L. Zhang, H. Wang, M. C. Muniz, A. Z. Panagiotopoulos, R. Car, and W. E, *The Journal of Chemical Physics* **156**, 124107 (2022).
- [103] M. Born and R. Oppenheimer, *Annalen der Physik* **389**, 457 (1927).
- [104] M. E. Tuckerman, *Journal of Physics: Condensed Matter* **14**, R1297 (2002).
- [105] R. P. Feynman, *Physical Review* **56**, 340 (1939).
- [106] P. Hohenberg and W. Kohn, *Physical Review* **136**, B864 (1964).
- [107] M. Levy, *Proceedings of the National Academy of Sciences* **76**, 6062 (1979).
- [108] M. Levy, *Physical Review A* **26**, 1200 (1982).
- [109] E. H. Lieb, *International Journal of Quantum Chemistry* **24**, 243 (1983).
- [110] W. Kohn and L. J. Sham, *Physical Review* **140**, A1133 (1965).
- [111] P. Geerlings, F. De Proft, and W. Langenaeker, *Chemical Reviews* **103**, 1793 (2003).
- [112] R. O. Jones, *Reviews of Modern Physics* **87**, 897 (2015).
- [113] R. G. Parr and W. Yang, *Density-Functional Theory of Atoms and Molecules* (Oxford University Press, 1994).
- [114] H. Eschrig, *The Fundamentals of Density Functional Theory*, edited by W. Ebeling, M. Pilkuhn, and B. Wilhelmi, TEUBNER-TEXTE Zur Physik, Vol. 32 (Vieweg+Teubner Verlag, Wiesbaden, 1996).
- [115] E. Engel and R. M. Dreizler, *Density Functional Theory: An Advanced Course*, Theoretical and Mathematical Physics (Springer Berlin Heidelberg, Berlin, Heidelberg, 2011).
- [116] W. Koch and M. C. Holthausen, *A Chemist’s Guide to Density Functional Theory* (John Wiley & Sons, 2015).
- [117] J. K. Percus, *International Journal of Quantum Chemistry* **13**, 89 (1978).
- [118] M. Levy and J. P. Perdew, in *Density Functional Methods In Physics*, NATO ASI Series, edited by R. M. Dreizler and J. da Providência (Springer US, Boston, MA, 1985) pp. 11–30.
- [119] J. P. Perdew and A. Zunger, *Physical Review B* **23**, 5048 (1981).
- [120] S. Baroni, P. Giannozzi, and A. Testa, *Physical Review Letters* **58**, 1861 (1987).
- [121] G. D. Mahan, *Physical Review A* **22**, 1780 (1980).
- [122] R. M. Sternheimer, *Physical Review* **96**, 951 (1954).
- [123] Y. Oba, T. Tadano, R. Akashi, and S. Tsuneyuki, *Physical Review Materials* **3**, 033601 (2019).
- [124] A. L. Fetter and J. D. Walecka, *Quantum Theory of Many-particle Systems* (Courier Corporation, 2003).
- [125] C. Bloch and C. De Dominicis, *Nuclear Physics* **7**, 459 (1958).
- [126] R. G. Della Valle and P. Procacci, *Physical Review B* **46**, 6141 (1992).
- [127] B. Fu, G. Tang, and A. J. H. McGaughey, *Physical Review Materials* **6**, 015401 (2022).
- [128] G. H. Wannier, *Physical Review* **52**, 191 (1937).
- [129] E. I. Blount, in *Solid State Physics*, Vol. 13, edited by F. Seitz and D. Turnbull (Academic Press, 1962) pp. 305–373.
- [130] N. Marzari and D. Vanderbilt, *Physical Review B* **56**, 12847 (1997).
- [131] N. Marzari, A. A. Mostofi, J. R. Yates, I. Souza, and D. Vanderbilt, *Reviews of Modern Physics* **84**, 1419 (2012).
- [132] J. M. Foster and S. F. Boys, *Reviews of Modern Physics* **32**, 303 (1960).
- [133] J. M. Foster and S. F. Boys, *Reviews of Modern Physics* **32**, 300 (1960).

- [134] S. F. Boys, [Reviews of Modern Physics](#) **32**, 296 (1960).
- [135] R. Resta, [Ferroelectrics](#) **136**, 51 (1992).
- [136] R. Resta, [Europhysics Letters](#) **22**, 133 (1993).
- [137] R. Resta, M. Posternak, and A. Baldereschi, [Physical Review Letters](#) **70**, 1010 (1993).
- [138] D. Vanderbilt and R. D. King-Smith, [Physical Review B](#) **48**, 4442 (1993).
- [139] M. V. Berry, [Proceedings of the Royal Society of London. A. Mathematical and Physical Sciences](#) **392**, 45 (1984).
- [140] R. Resta, [Reviews of Modern Physics](#) **66**, 899 (1994).
- [141] D. Xiao, M.-C. Chang, and Q. Niu, [Reviews of Modern Physics](#) **82**, 1959 (2010).
- [142] N. A. Spaldin, [Journal of Solid State Chemistry Polar Inorganic Materials: Design Strategies and Functional Properties](#), **195**, 2 (2012).
- [143] M. Neumann, O. Steinhauser, and G. S. Pawley, [Molecular Physics](#) (1984), [10.1080/00268978400101081](#).
- [144] R. Ramírez, T. López-Ciudad, P. Kumar P, and D. Marx, [The Journal of Chemical Physics](#) **121**, 3973 (2004).
- [145] R. Iftimie and M. E. Tuckerman, [The Journal of Chemical Physics](#) **122**, 214508 (2005).
- [146] T. Amano, T. Yamazaki, R. Akashi, T. Tadano, and S. Tsuneyuki, [Physical Review B](#) **107**, 094305 (2023).
- [147] D. M. Eagles, [Journal of Physics and Chemistry of Solids](#) **25**, 1243 (1964).
- [148] J. R. DeVore, [JOSA](#) **41**, 416 (1951).
- [149] R. A. Parker, [Physical Review](#) **124**, 1719 (1961).
- [150] W. G. Spitzer, R. C. Miller, D. A. Kleinman, and L. E. Howarth, [Physical Review](#) **126**, 1710 (1962).
- [151] A. S. Barker and M. Tinkham, [The Journal of Chemical Physics](#) **38**, 2257 (1963).
- [152] G. A. Samara and P. S. Peercy, [Physical Review B](#) **7**, 1131 (1973).
- [153] F. Gervais and B. Piriou, [Physical Review B](#) **10**, 1642 (1974).
- [154] N. Matsumoto, T. Hosokura, K. Kageyama, H. Takagi, Y. Sakabe, and M. Hangyo, [Japanese Journal of Applied Physics](#) **47**, 7725 (2008).
- [155] S. Schöche, T. Hofmann, R. Korlacki, T. E. Tiwald, and M. Schubert, [Journal of Applied Physics](#) **113**, 164102 (2013).
- [156] K. Kanehara, T. Hoshina, H. Takeda, and T. Tsurumi, [Journal of the Ceramic Society of Japan](#) **123**, 303 (2015).
- [157] J. G. Traylor, H. G. Smith, R. M. Nicklow, and M. K. Wilkinson, [Physical Review B](#) **3**, 3457 (1971).
- [158] F. Gervais, [Materials Science and Engineering: R: Reports](#) **39**, 29 (2002).
- [159] C. Lee and X. Gonze, [Physical Review B](#) **49**, 14730 (1994).
- [160] K. M. Glassford and J. R. Chelikowsky, [Physical Review B](#) **46**, 1284 (1992).
- [161] B. Montanari and N. M. Harrison, [Chemical Physics Letters](#) **364**, 528 (2002).
- [162] B. Montanari and N. M. Harrison, [Journal of Physics: Condensed Matter](#) **16**, 273 (2004).
- [163] R. Sikora, [Journal of Physics and Chemistry of Solids](#) **66**, 1069 (2005).
- [164] P. D. Mitev, K. Hermansson, B. Montanari, and K. Refson, [Physical Review B](#) **81**, 134303 (2010).
- [165] B. Lee, C.-k. Lee, C. S. Hwang, and S. Han, [Current Applied Physics International Conference on Electronic Materials](#), **11**, S293 (2011).
- [166] A. Grünebohm, C. Ederer, and P. Entel, [Physical Review B](#) **84**, 132105 (2011).
- [167] B. Wehinger, A. Bosak, and P. T. Jochym, [Physical Review B](#) **93**, 014303 (2016).
- [168] Y. Zhang, J. W. Furness, B. Xiao, and J. Sun, [The Journal of Chemical Physics](#) **150**, 014105 (2019).
- [169] P. Ghosez, X. Gonze, and J.-P. Michenaud, [Europhysics Letters](#) **33**, 713 (1996).
- [170] F. Labat, P. Baranek, C. Domain, C. Minot, and C. Adamo, [The Journal of Chemical Physics](#) **126**, 154703 (2007).
- [171] P. Torres, F. X. Alvarez, X. Cartoixà, and R. Rurali, [2D Materials](#) **6**, 035002 (2019), [arxiv:1903.11920](#).
- [172] W. Cochran and R. A. Cowley, [Journal of Physics and Chemistry of Solids](#) **23**, 447 (1962).
- [173] F. R. Charvat and W. D. Kingery, [Journal of the American Ceramic Society](#) **40**, 306 (1957).
- [174] I. Yoshida, [Journal of the Physical Society of Japan](#) **15**, 2211 (1960).
- [175] P. U. T. P. R. Center and Y. S. Y. S. Touloukian, [Thermophysical properties of matter](#) (IFI/Plenum, 1970).
- [176] K. M. Ok, Y. Ohishi, H. Muta, K. Kurosaki, and S. Yamanaka, [Journal of the American Ceramic Society](#) **101**, 334 (2018).
- [177] G. Kresse and J. Furthmüller, [Physical Review B](#) **54**, 11169 (1996).
- [178] J. P. Perdew and A. Zunger, [Physical Review B](#) **23**, 5048 (1981).
- [179] J. P. Perdew, A. Ruzsinszky, G. I. Csonka, O. A. Vydrov, G. E. Scuseria, L. A. Constantin, X. Zhou,

- and K. Burke, [Physical Review Letters](#) **100**, 136406 (2008).
- [180] J. W. Furness, A. D. Kaplan, J. Ning, J. P. Perdew, and J. Sun, [The Journal of Physical Chemistry Letters](#) **11**, 8208 (2020).
- [181] G. Kresse and D. Joubert, [Physical Review B](#) **59**, 1758 (1999).
- [182] F. Zhou, W. Nielson, Y. Xia, and V. Ozoliņš, [Physical Review Letters](#) **113**, 185501 (2014).
- [183] J. K. Burdett, T. Hughbanks, G. J. Miller, J. W. Richardson, and J. V. Smith, [Journal of the American Chemical Society](#) **109**, 3639 (1987).
- [184] T. Lan, C. W. Li, O. Hellman, D. S. Kim, J. A. Muñoz, H. Smith, D. L. Abernathy, and B. Fultz, [Physical Review B](#) **92**, 054304 (2015).
- [185] S. P. S. Porto, P. A. Fleury, and T. C. Damen, [Physical Review](#) **154**, 522 (1967).
- [186] M. Dou and C. Persson, [Journal of Applied Physics](#) **113**, 083703 (2013).
- [187] T. Lan, X. Tang, and B. Fultz, [Physical Review B](#) **85**, 094305 (2012).
- [188] E. Shojaei and M. R. Mohammadzadeh, [Journal of Physics: Condensed Matter](#) **22**, 015401 (2009).
- [189] Y. Yomogida, Y. Sato, R. Nozaki, T. Mishina, and J. Nakahara, [Journal of Molecular Liquids](#) **154**, 31 (2010).
- [190] S. Sarkar, D. Saha, S. Banerjee, A. Mukherjee, and P. Mandal, [Chemical Physics Letters](#) **678**, 65 (2017).
- [191] J. Alonso, F. J. Bermejo, M. García-Hernández, J. L. Martínez, W. S. Howells, and A. Criado, [The Journal of Chemical Physics](#) **96**, 7696 (1992).
- [192] V. Schettino, R. Chelli, S. Marsili, A. Barducci, C. Faralli, M. Pagliai, P. Procacci, and G. Cardini, [Theoretical Chemistry Accounts](#) **117**, 1105 (2007).
- [193] “Car-Parrinello Molecular Dynamics,” .
- [194] A. D. Becke, [Physical Review A](#) **38**, 3098 (1988).
- [195] C. Lee, W. Yang, and R. G. Parr, [Physical Review B](#) **37**, 785 (1988).
- [196] S. Goedecker, M. Teter, and J. Hutter, [Physical Review B](#) **54**, 1703 (1996).
- [197] U. E. N. C. f. E. Assessment, [CRC Handbook of Chemistry and Physics](#) (2009).
- [198] M. J. Abraham, T. Murtola, R. Schulz, S. Páll, J. C. Smith, B. Hess, and E. Lindahl, [SoftwareX](#) **1–2**, 19 (2015).
- [199] J. Wang, R. M. Wolf, J. W. Caldwell, P. A. Kollman, and D. A. Case, [Journal of Computational Chemistry](#) **25**, 1157 (2004).
- [200] A. Jakalian, D. B. Jack, and C. I. Bayly, [Journal of Computational Chemistry](#) **23**, 1623 (2002).
- [201] J. Wang, W. Wang, P. A. Kollman, and D. A. Case, [Journal of Molecular Graphics and Modelling](#) **25**, 247 (2006).
- [202] A. W. Sousa da Silva and W. F. Vranken, [BMC Research Notes](#) **5**, 367 (2012).
- [203] L. Martínez, R. Andrade, E. G. Birgin, and J. M. Martínez, [Journal of Computational Chemistry](#) **30**, 2157 (2009).
- [204] A. Paszke, S. Gross, F. Massa, A. Lerer, J. Bradbury, G. Chanan, T. Killeen, Z. Lin, N. Gimelshein, L. Antiga, A. Desmaison, A. Köpf, E. Yang, Z. DeVito, M. Raison, A. Tejani, S. Chilamkurthy, B. Steiner, L. Fang, J. Bai, and S. Chintala, “PyTorch: An Imperative Style, High-Performance Deep Learning Library,” (2019), [arxiv:1912.01703 \[cs, stat\]](#) .
- [205] A. F. Agarap, “Deep Learning using Rectified Linear Units (ReLU),” (2019), [arxiv:1803.08375 \[cs, stat\]](#) .
- [206] D. P. Kingma and J. Ba, “Adam: A Method for Stochastic Optimization,” (2017), [arxiv:1412.6980 \[cs\]](#) .
- [207] D. W. Davidson, [Canadian Journal of Chemistry](#) **35**, 458 (1957).
- [208] E. U. Franck and R. Deul, [Faraday Discussions of the Chemical Society](#) **66**, 191 (1978).
- [209] I. Doroshenko, V. Pogorelov, and V. Sablinskas, [Dataset Papers in Science](#) **2013**, e329406 (2012).
- [210] M. Jorge, J. R. B. Gomes, and M. C. Barrera, [Journal of Molecular Liquids](#) **356**, 119033 (2022).
- [211] E. V. Ivash and D. M. Dennison, [The Journal of Chemical Physics](#) **21**, 1804 (1953).
- [212] I. Y. Shilov, [Molecular Physics](#) **113**, 570 (2015).
- [213] E. B. Freyer, J. C. Hubbard, and D. H. Andrews, [Journal of the American Chemical Society](#) **51**, 759 (1929).
- [214] I.-F. W. Kuo, C. J. Mundy, M. J. McGrath, J. I. Siepmann, J. VandeVondele, M. Sprik, J. Hutter, B. Chen, M. L. Klein, F. Mohamed, M. Krack, and M. Parrinello, [The Journal of Physical Chemistry B](#) **108**, 12990 (2004).
- [215] M. J. Gillan, D. Alfè, and A. Michaelides, [The Journal of Chemical Physics](#) **144**, 130901 (2016).
- [216] S. Koda, T. Mori, and S. Kojima, [Journal of Molecular Structure From Molecules to Molecular Materials, Biological Molecular Systems and Nanostructures](#), **1126**, 127 (2016).
- [217] E. Xiao and C. A. Marianetti, [Physical Review B](#) **107**, 094303 (2023).